UNIVERSITÀ DEGLI STUDI DI NAPOLI
“FEDERICO II”

Scuola Politecnica e delle Scienze di Base

Area Didattica di Scienze Matematiche Fisiche e Naturali

Dipartimento di Fisica “Ettore Pancini”

Laurea Magistrale in Fisica

Femtosecond laser surface texturing of a metallic target

Relatori:
Prof.Salvatore Amoruso
Dott.Jijil JJ Nivas

Candidato:
Martina D’Andrea
Matr. $N94000632$

Anno Accademico 2020/2021

Contents

Introduction

Since the advent of the laser, the processing of materials by using intense laser pulses developed into a scientific evergreen due to its potential in industrial and scientific applications. More recently, the advent of sources providing ultrashort pulses $(\sim 100\ fs)$ has further strengthened the realm of laser material processing. Among the various approaches, direct laser irradiation with ultrashort pulses promotes the development of surface structures with altered and tunable properties that find space in a wide range of fields : biomedicine, tribology, electronics, etc. Different types of surface structures can be generated on solid targets, in particular the Laser Induced Periodic Structures (LIPSS) are an universal phenomenon that has been observed in most of materials (metals, dielectrics, semiconductors) and in various environments (air, water). LIPSS features are linked to the laser beam parameters (e.g. wavelength, pulse fluence, repetition rate, etc.). According to their periodicity, they are divided in two different classes: low spatial frequency LIPSS (LSFL), commonly indicated as *ripples*, and high spatial frequency LIPSS (HSFL).

This thesis work deals with a study on femtosecond fs laser surface structuring of a copper target in air. Copper is a material widely used in electric devices thanks to its thermal and electrical properties. In this frame, the choice to modify the surface structure of a cooper sample relies on the demand to mitigate the generation of secondary electrons in the particles accelerators. In the high energy colliders, photoemission and secondary emission phenomena cause multiplication processes within the beam chambers, whose walls are typically made of copper. These effects lead to the formation of an electron cloud causing the instability of particles beams. Previous works evidenced the potential of surface ripples to reduce this type of phenomenon. However, further investigations are required to improve and optimize the copper surface texturing.

In this context, there is a need to laser texture large areas of the target material in an appropriate time. Most of the previous works on laser surface texturing have been carried out by exploiting Ti:Sa laser sources that typically provide train of pulses at $1\ kHz$. More recently, solid state laser sources at larger repetition rates have become available and are being applied to large area processing. In fact, even an increase of a factor five or ten of the repetition rate can reduce the processing time by a corresponding amount, maintaining fixed the other parameters. However, this requires the use of fast scanning systems for the rastering of the laser beam over the target surface. Here we pursue an alternative approach to form periodic surface structures over a millimeter size area in less time, by using a cylindrical lens for the laser beam focusing. From this point of view, this work is devoted to the morphological characterization of the induced surface structures on copper by means of laser beams with an elliptical profile at different laser wavelengths, in order to clarify the possible merits and drawbacks of such an approach.

This thesis is composed of five chapters.

Chapter (1) introduces femtosecond laser ablation phenomenon and describes the mechanisms of LIPSS formation.

The second Chapter deals with the experimental setup for femtosecond laser ablation and for the morphological analysis of the surface structures.

In Chapter (3) the influence of repetition rates on copper and the adaptability of the Gaussian beam model on the spots produced by the cylindrical lens have been tested.

The fourth Chapter is devoted to ripples appearing on the surface structures and to the analysis of nanoparticles distribution dynamics over the target.

Finally, Chapter (5) describes the morphological features of an area after the laser treatment and explores the influence of the Gaussian intensity distribution impressed on the material surface.

Chapter 1

Laser Induced Periodic Structures

During the last five decades, with the availability of ultra-fast laser sources, Laser Induced Periodic Surface Structures (LIPSS) have gained plenty of attention from the scientific community due to their versatility, reliability and production speed.

In this Chapter we discuss about mechanisms underlying LIPSS formation and their employment in various scientific fields. In particular in Sect.(1.1) we deal with the femtosecond laser ablation process and the Gaussian beam model, which allows to have an experimental method to evaluate the so-called *energy threshold* as well as the beam spot size on the target surface; in Sect.(1.2) we talk about the birth of LIPSS topic and its developments; in Sect.(1.3) we face different proposed theories for LIPSS formation and in Sect.(1.4) we offer a panoramic view on both many key factors that permit their control and on several fields of application.

1.1 Femtosecond laser ablation: the TTM and Gaussian beam models

Over the past ten years, the employment of femtosecond laser systems has enhanced the development of nano- and micro- structuring techniques and ensured a fast way to create materials with altered but controllable properties. These processes are all based on the well-known physical phenomenon that goes by the name of *laser ablation*, of which we gave a scheme in Fig.(1.1).

The phenomenon of femtosecond laser ablation occurs on solid targets upon the irradiation by ultra-short laser pulses ($\tau_p \sim ps \div fs$) and basically consists in the removal of a part of material from its surface.
From a theoretical point of view, the *Two Temperature Model* (TTM) should be introduced to explain mechanisms underlying this process. This theory assumes the interaction between two subsystems: the electrons and the lattice.

When a train of ultra-short laser pulses hits the material surface (e.g., a metal) the electrons, within the optical penetration depth, instantaneously absorb the energy of the pulses due to their short interaction time whereas the lattice remains cold.

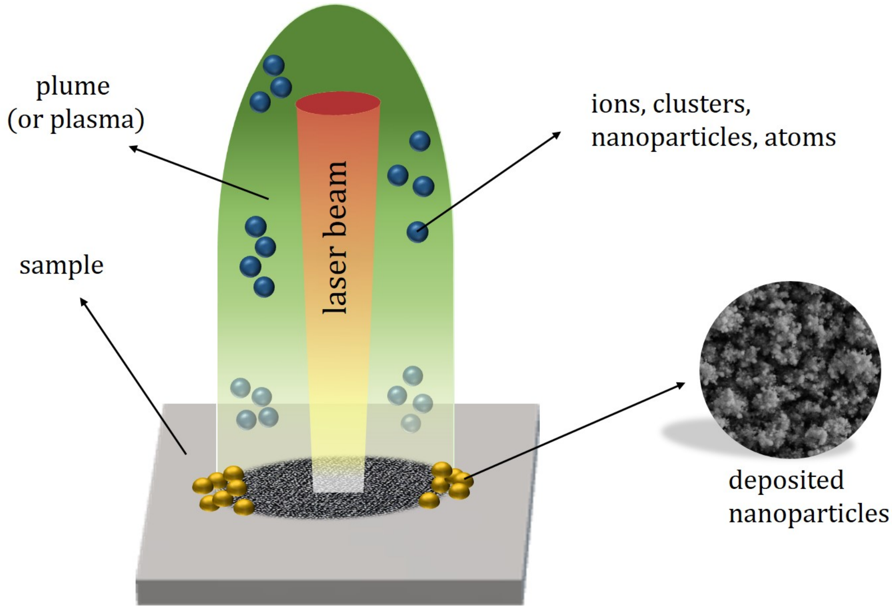

Figure 1.1: Laser ablation process: the laser beam impacts onto the sample and causes the expulsion of material from its surface in form of nanoparticles, ions and neutral atoms held in a plume. Afterwards, due to the external pressure and temperature, some nanoparticles deposit surrounding the ablated region and decorating it.

As a result, the whole system stands in a nonequilibrium stage due to the different temperatures between the cold lattice and the hot electronic system, both in a local thermal equilibrium among themselves [31].
Hence, to restore equilibrium, the electrons progressively transfer energy to the lattice system, through the so-called *electron-phonon coupling*. The duration of this phenomenon depends on the electron-phonon relaxation time τ_{e-ph}, which is correlated to the specific material and usually ranges from $0.1\ ps$ to $10\ ps$ [7], [67].
The TTM exploits the following equations (1.1) and (1.2) to describe the temporal evolution of the temperatures of the lattice, T_L, and electrons, T_e, thus allowing to study the heat transferred between the two systems and their thermal properties [28], [61]:

$$C_L \frac{\partial T_L}{\partial t} = \vec{\nabla} \cdot (\kappa_L \vec{\nabla} T_L) + g_{e-ph}(T_e - T_L) \tag{1.1}$$

$$C_e \frac{\partial T_e}{\partial t} = \vec{\nabla} \cdot (\kappa_e \vec{\nabla} T_e) + g_{e-ph}(T_e - T_L) + S(\vec{r}, t) \tag{1.2}$$

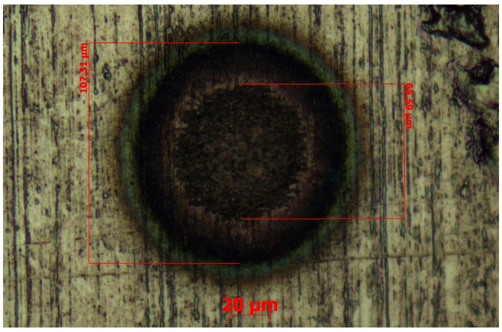

(a) OM image of a crater produced on copper in air with a spherical lens ($\lambda = 1030\ nm$, $RR = 15\ kHz$, $E = 55\ \mu J$, $N = 200$).

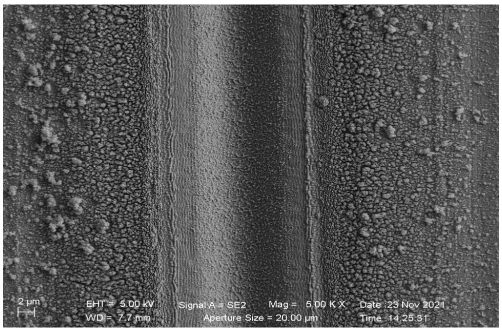

(b) SEM image of a crater produced on copper in air with a cylindrical lens ($\lambda = 515\ nm$, $RR = 5\ kHz$, $E = 170\ \mu J$, $N = 200$).

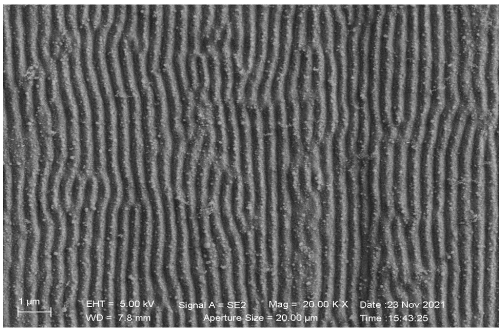

(c) SEM image of a large area processed with a scanning velocity of $v_s = 5\ mm/s$ ($\lambda = 515\ nm$, $RR = 5\ kHz$, $E = 176\ \mu J$, $N = 200$).

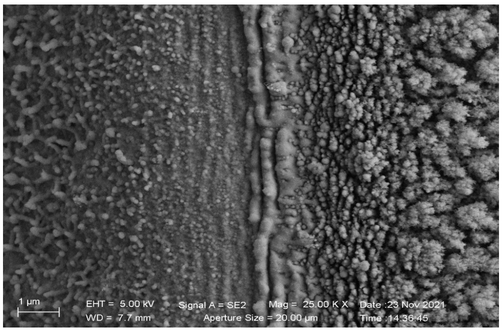

(d) Zoomed SEM image of a crater produced on copper in air with a cylindrical lens ($\lambda = 515\ nm$, $RR = 5\ kHz$, $E = 197\ \mu J$, $N = 200$).

Figure 1.2: Different structures generated on copper through both spot processing [(a), (b), (d)] and scanning line processing [(c)] in the frame of this thesis work.

where κ_e and κ_L are the electron and lattice heat conductivities; C_e and C_L stands for the electron and lattice capacities; g_{e-ph} is the electron-phonon coupling strength and S corresponds to the laser pulse energy [28], [61]. According to the duration of the pulses, the equations (1.1) and (1.2) have two limits:

- If $\tau_p \geq \tau_{e-ph}$ (i.e $\tau_p \sim ps$) the electrons begin to thermalize during the irradiation of the target and reach a quasi-stationary condition, while the temperature of the lattice increases linearly with the time until the electronic system cools down. In this case ablation occurs through the competition among melting, vaporization and solidification [28];

- If $\tau_p \leq \tau_{e-ph}$ (i.e $\tau_p \sim fs$) the electron-phonon interaction occurs after the laser irradiation and lasts until the equilibrium among the lattice and the electrons is reached. In this case, depending on the attained temperature of lattice T_L, phenomena of amorphization, melting and ablation may happen [28], [67].

When T_L is sufficiently low, the heat absorbed by the target disperses in a thin layer below its surface. In this case the cooling rate is so high ($\sim 10^9 K/s$) that it does not allow the material re-crystallization and causes the surface to appear in an amorphous state [68].
If T_L is higher than the previous case and reaches the melting temperature T_m then the surface results in liquid phase that lasts from $10\ ps$ to $100\ ps$. Different theories are proposed to explain the transport in the melted stage; some authors propose a model based on Navier-Stokes equations or on the Marangoni effect for convection motion [7], [12]; others suggest that the fluid behaves as an incompressible Newtonian fluid [61]. The molten stage usually stands in non-equilibrium conditions before the resolidification process. In this scenario, if the temperature of lattice reaches high values, the melted material gets involved in phenomena of vaporization, evaporation, boiling and thus ablation [16], [68].

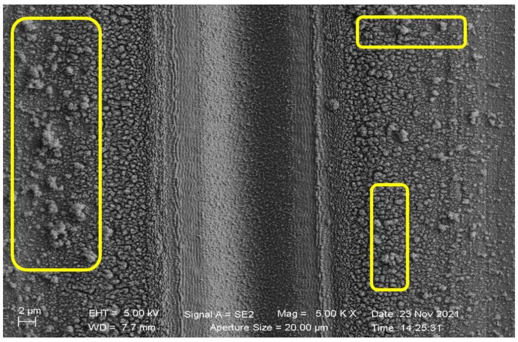

(a) SEM image of a crater produced on copper through a cylindrical lens; the circled areas highlight the deposited nanoparticles.

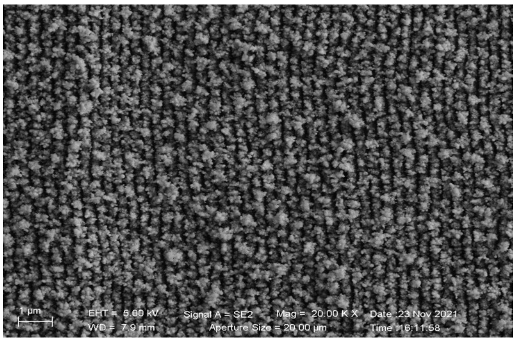

(b) SEM image of a large area entirely covered by nanoparticles.

Figure 1.3: Different structures generated on a copper sample through both spot processing (a) and scanning line processing (b) in the frame of this thesis work.

Therefore, the phenomenon of ablation manifests with several mechanisms and apart from the aforementioned ones, it can occur through effects of spallation, fragmentation and phase explosion [1] [67]. Ablation verifies from a time scale of $10\ ps$ up to $100\ ns$, following which the sample surface cools down and rapidly solidifies, giving rise to surface structures, examples of which are displayed in Fig (1.2).

[1]At high temperatures of the lattice, close to $0.90\ T_{cr}$, where T_{cr} is the critical temperature of the material, the melted surface undergoes a phase transition to a superheated liquid. Afterwards, bubbles form and lead to the formation of vapor and liquid droplets which are ejected from the material [60].

The material removed from the surface stands up in a *plume* (or plasma), composed by nanoparticles, ions, atoms, clusters and droplets. The plume survives above the target from several ns up to $100\ \mu s$ depending on the environment in which it expands [1]. Subsequently, due to the external ambient pressure the nanoparticles deposit back onto the surface, decorating it.

The generation of nanoparticles is suitable for several film deposition applications that go under the name of *Pulsed Laser Deposition* (PLD). Developments in this field require the control of three important parameters: (i) the cooling speed of the plume; (ii) ambient pressure; (iii) temperature, which are responsible of the properties and dispersion of nanoparticles surrounding the ablated region [55]. Figure (1.3) illustrates deposition of nanoparticles debris on the surface of the target after laser irradiation.

The morphology of surface structures strictly depends on the laser parameters; in particular the laser fluence has an impressive impact on its features.

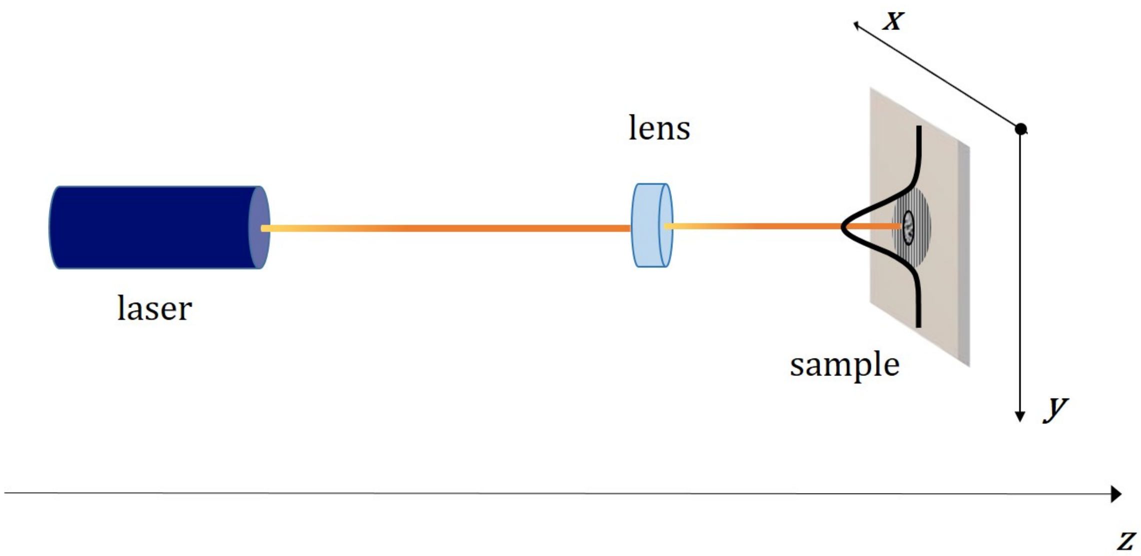

Figure 1.4: Representation of the Gaussian profile along the sample surface.

In the following, the determination of the characteristic fluence threshold for a specific process (e.g. ablation, structures formation, surface modification, etc.) is illustrated in the case of a Gaussian beam [25]. Such an approach has been shown to be valid also for beams with more complex spatial shapes, as for example vector vortex beams carrying orbital angular momentum [39]. This model also allows determining the laser spot size on the target surface, another important experimental parameter.

Let us assume to have a material surface in the x and y plane, hit by a train of femtosecond laser pulses propagating along the z direction. It is commonly assumed that for a laser beam focused through a lens, the spatial profile on the sample surface is Gaussian [Fig.(1.4)].

Hence, indicating with r the distance between a point of the surface and the point corresponding to the maximum value of the fluence ϕ (energy for unit of area), the formula in Eq.(1.3) shows the Gaussian profile of $\phi(r)$:

$$\phi(r) = \phi_0 e^{-\frac{2r^2}{w_0^2}} \qquad \text{and} \qquad \phi_0 = \frac{2E}{\pi w_0^2} \tag{1.3}$$

where ϕ_0 is the peak fluence, w_0 is the Gaussian spot size corresponding to the radius for which $\phi(r)$ decays by a factor $1/e^2$ and E stands for the pulse energy.

As above mentioned, different surface features arise from the radiation-matter interaction depending on the value of the laser fluence. This correlation is true for both spot and line scanning processing [see Paragraph (1.3.3)], [12].

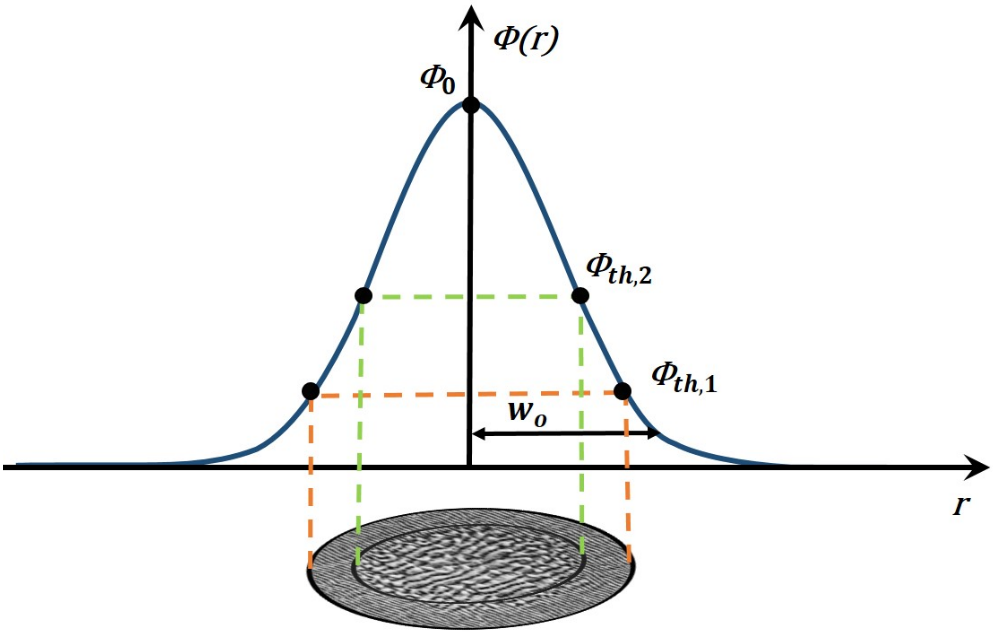

Figure 1.5: Schematic representation of the fluence of a Gaussian laser beam; in particular two different fluences were marked for the two different regions visible on a crater produced by a laser beam on the surface of a silicon sample; the image of crater belongs to Ref.[1].

Therefore for each distinct region as long as w_0 is the same [see Fig.(1.4)], it can be defined the fluence threshold ϕ_{th} as in Eq.(1.4), characteristic for each material.

$$\phi_{th} = \phi(r_{th}) = \phi_0 e^{-\frac{2r_{th}^2}{w_0^2}} \tag{1.4}$$

where r_{th} is the radius of the specific region presenting the process of interest with fluence threshold ϕ_{th}. Replacing ϕ_0 and ϕ_{th} with the expression in Eq.(1.3), the formula in Eq.(1.4) becomes:

$$\phi_{th} = \frac{2E_{th}}{\pi w_0^2} = \frac{2E}{\pi w_0^2} e^{-\frac{2r_{th}^2}{w_0^2}} = \phi(r_{th}) \tag{1.5}$$

from which one can obtain an expression for r_{th} [Eq.(1.6)].

$$r_{th}^2 = \frac{w_0^2}{2} ln\left(\frac{E}{E_{th}}\right) \tag{1.6}$$

Equation (1.6) represents the starting point to experimentally evaluate the Gaussian spot w_0, the energy threshold E_{th} and consequently the fluence threshold ϕ_{th}. The method consists in generating spots on the surface at fixed λ, repetition rate RR and variable pulse energy E and then measuring the crater size as a function E. In the present work such a procedure was exploited to determine ϕ_{th} for copper samples, performing a fit through Eq.(1.6).
Additional discussions and results are provided in Chapter (3).

1.2 History of LIPSS

The generation of periodic surface structures upon linearly polarized radiation is an universal phenomenon which occurs on almost any solid target (metals, semiconductors and dielectrics) in different kinds of environments (air, vacuum, liquids, etc).
Depending on the material, selected laser parameters and working conditions, various type of surface structures can be processed whose feature sizes range from several micrometers to few tens of nanometres [6], [8].

LIPSS were observed for the first time in 1965 by Birnbaum on polished germanium crystal surfaces irradiated with a focused ruby laser beam [5]. Initially this formation was ascribed to some diffraction effects along with material removal phenomena which lead to the surface structuring at the maxima of the intensity pattern. Subsequently, during the eighties of the twentieth, many authors suggested a new theory based on a mechanism of interference between the excited surface wave scattered at the rough surface and the incident laser beam.
At that time, the interest and the research in this field were not so intense as it lefts few doubts and questions. However, in the early ages of the new millennium, the discover of a "non-classical" type of LIPSS with period significantly smaller than the laser wavelength (the ones named *HSFL*) gave a new resonance to LIPSS topic, strongly supported by the commercial availability of ultra-short laser pulses ($\tau_p \sim fs \div ps$) [7], [8].

Sipe and co-workers coined in 1982 the term "LIPSS"; in particular, with both theoretical and experimental approaches, they introduced for the first time the so-called

efficacy factor η.
The efficacy factor is a scalar function that represents the propensity of the material to absorb the inhomogeneous energy at the surface roughness and allows to identify the LIPSS period and orientation as a function of the laser parameters (wavelength λ, angle of incidence θ, polarization direction) and surface parameters (dielectric permittivity ϵ, shape factor s and filling factor F linked to the surface roughness). Sipe's theory also introduces a set of 14 equations for the evaluation of the LIPSS periods. Although this theory is the most accepted one, it is unable to predict some types of structures because it does not include the treatment of the feedback mechanisms, of which we will talk about in Paragraph (1.3.3) [8], [12].

Apart from many theories developed in the last years to investigate LIPSS formation and actually object of debate, it is important to point out the development and the employment of laser sources at high repetition rate (*HRR*).
Modern solid-state lasers can provide repetition rates ranging from kHz up to MHz. The implementation of laser source with high pulse energy and high repetition rate allows to realize nanostructures in the fastest way that we are currently able to guarantee and that can meet industrial requirements [30].
Nowadays, through the employment of scanning systems, the laser approach is capable to manufacture large areas of several hundreds of cm^2 in few minutes.

Nevertheless, it is necessary to pay attention with laser sources at high repetition rates, since some undesirable effects may ensue. One of them is the *plume shielding effect*, occurring when the temporal distance between two consecutive pulses is smaller than the time during which the plume stays above the target surface.
In this case, the laser pulse interacts with the nanoparticles, ions and neutral atoms held in the plume, leading to some unwanted morphological modifications on the target surface [1].

Anyhow, fs laser induced surface structuring became one of the most enviable and competitive techniques available in the industrial sector. Moreover, it results a valid alternative to the already known nanostructuring methods (chemical vapour deposition (*CVD*), electron beam lithography (*EBL*), nano-imprinting, wet and dry etching, photolithography etc.) which are often expensive, time-consuming and require also the employment of different kinds of elements (e.g. optical masks, vacuum systems) and conditions (e.g. clean rooms) [12], [18].

In particular, this work carried out at Dipartimento di Fisica "Ettore Pancini", fits in this framework since the obtained nanostructures were realized through laser pulses in the range of kHz.

1.3 Theory of LIPSS

As mentioned in Sect.(1.2), LIPSS are generated when a laser beam linearly polarized strikes a solid surface. They usually emerge as surface relief characterized by periodic lines which show a correlation with the laser beam polarization and wavelength. According to their spatial period LIPSS are commonly divided in two different classes:

- *Low-spatial frequency LIPSS* (LSFL): with $\lambda/2 \leq \Lambda_{LSFL} \leq \lambda$, where λ is the wavelength of the laser beam and Λ_{LSFL} is the spatial period of the structure. Furthermore, these kind of LIPSS are also referred to as *ripples*. In turn, LSFL are divided into two groups:

    a) *LSFL-I*: these structures are typical for metals and semiconductors and are characterized by $\Lambda_{LSFL} \sim \lambda$ and orientated perpendicular to the laser beam polarization ;

    b) *LSFL-II*: these structures are typical for materials with large band gap and are characterized by $\Lambda_{LSFL} \sim \lambda/n$, with n being the refractive index of the material, and are usually orientated parallel to the laser beam polarization [7], [8];

- *High-spatial frequency LIPSS* (HSFL): with $\Lambda_{HSFL} < \lambda/2$ where λ is the wavelength of the laser beam and Λ_{HSFL} is the spatial period of the structure. In turn, LSFL are divided into two groups depending on the depth-to-period aspect ratio A:

    a) *HSFL-I*: with $A > 1$, typically observed for semiconductors and dielectrics;

    b) *HSFL-II*: with $A < 1$, typically observed for metals [6], [8].

Fig. (1.6) displays a scheme which summarizes the classification of LIPSS and Fig. (1.7) illustrates some examples of the above-mentioned structures.

Anyhow, besides the LIPSS illustrated above and displayed in Fig.(1.7), other surface structures with supra-wavelength period, that have not yet been included in the previous classification, have been observed. These structures are generally indicated as *grooves* and have been much less investigated than ripples. They are preferentially aligned along a direction parallel to the laser polarization, and hence orthogonal to ripples, and they typically form at larger fluence values and for higher number of laser pulses with respect to ripples [8], [20].

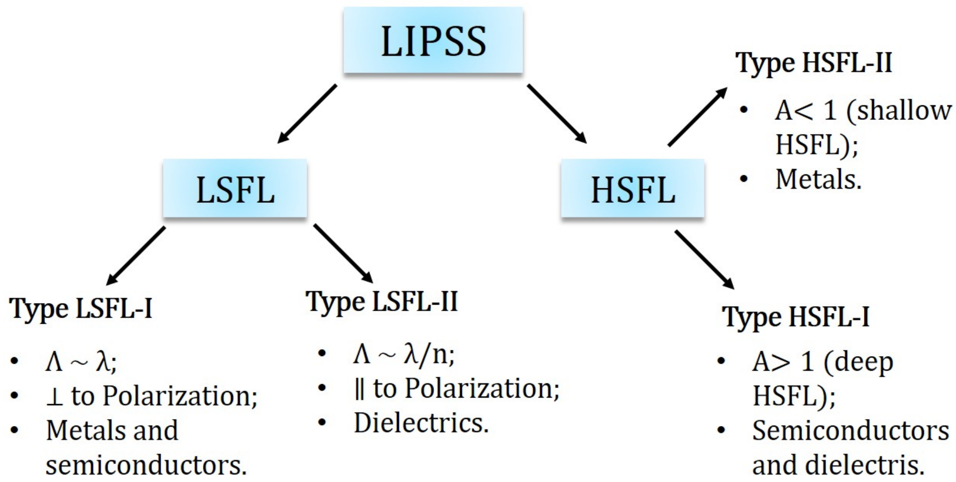

Figure 1.6: Classification scheme for LIPSS, [8].

Grooves formation has been reported in semiconductors (Si, InP, etc.) [11], [19] dielectrics (e.g., SiO_2) [62] and in some metals and alloys (e.g., Ni, Ti, steel, etc.) [61], [63]. The formation mechanisms and the dependence of their characteristic features on the various experimental parameters have yet to be fully clarified [38]. However such a task is out of the scope of this thesis work since it was carried out in an irradiation regime for which grooves formation does not take place.

As regards the theories on the formation of LIPSS, the current scientific community is divided between those who sustain electromagnetic theories and those who support matter reorganization theories. The main difference between these two thoughts must be searched in the temporal regime within which LIPSS are formed.

- Concerning electromagnetic theories, the generation of LIPSS is directly linked to the deposition of optical energy into the solid, during the laser irradiation;
- Concerning matter reorganization theories, LIPSS form after laser irradiation (from hundred of *ps* to tens of ms) and this may involve hydrodynamic effects along with material instabilities, erosion effects and creation of defects.

In particular, for solids irradiated with ultra short lases pulses (*ps* or fs) both scenarios can occur in two separate temporal regimes. This question can be explored using two experimental approaches: the first one employs double fs pulses to investigate optical absorption by the material, the latter one uses time-resolved spectroscopy (e.g. pump-probe) to study the ultrafast dynamics of the LIPSS [7], [8].

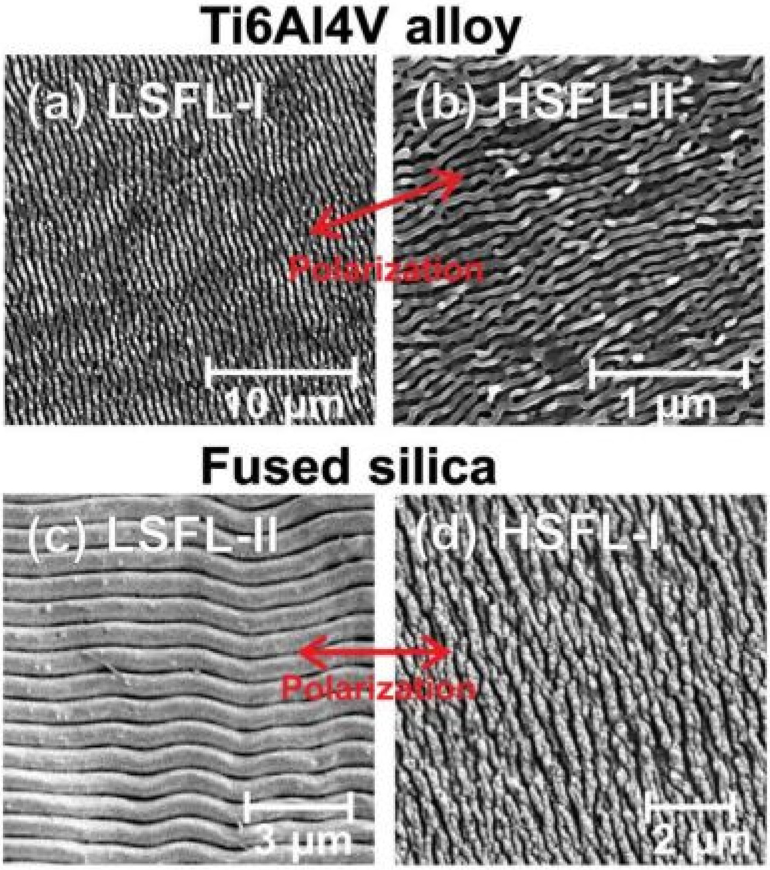

Figure 1.7: SEM images showing different types of LIPSS. The upper panels display LIPSS for a sample of Ti6Al4V titanium alloy: *LSFL-I* (on the left), *HSFL-II* (on the right); the bottom panels illustrate structures for fused silica:*LSFL-II* (on the left), *HSFL-I* (on the right). The red arrow indicates the direction of polarization [7].

1.3.1 Electromagnetic theories

When we talk about electromagnetic theories for LIPSS formation, we usually refer to low spatial frequency LIPSS, the ones we named *LFSL*.

We have already made the difference between *LSFL-I* and *LSFL-II*, however it was a distinction which accounted structural characteristics; now we want to underline also that the mechanisms of *LSFL-I* and *LSFL-II* formation are not the same. It is generally accepted that *LSFL-I* arise from an interference between the incident laser beam and a s*urface electromagnetic wave* (*SEW*) generated on the rough surface [see Fig. (1.8)].

Initially, we can image that the incident laser beam linearly polarized generates a defect on the material, which acts as a scattering center. Consequently, a wave propagating along the surface through scattering effects, is produced. This wave, known as

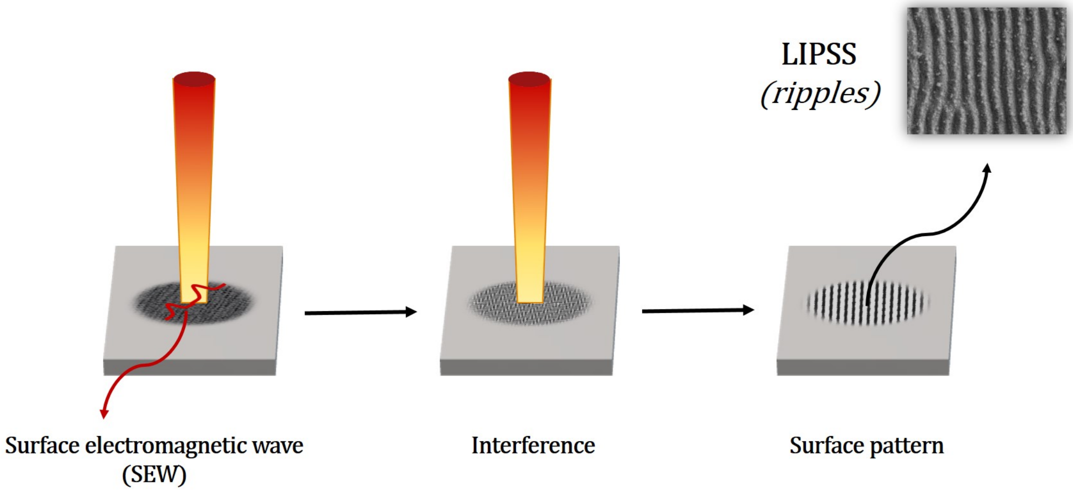

Figure 1.8: Mechanism of interference between SEW and the incident laser beam, which leads to LIPSS.

SEW, interacts in turn with the incident laser beam and creates an interference pattern which modulates the spatial energy distribution deposited onto the sample [7], [8].

Sometimes, the mechanism explained above may involve the excitation of *Surface Plasmon Polaritons* (SPPs), which are waves that propagate across the interface between two media, under specific conditions on their dielectric permittivities [Eq (1.7)], [18].

$$Re\{\epsilon_{air}\}Re\{\epsilon_{sample}\} + Im\{\epsilon_{air}\}Im\{\epsilon_{sample}\} < 0 \tag{1.7}$$

For metals, it can be shown that upon irradiation in air (in the range from visible to near IR), the SPPs are excited if the dielectric permittivity ϵ_m (m stands for metal) reaches the condition $Re\{\epsilon_m\} < -1$.

In literature, referring to *the SPP standard model of LIPSS*, the spatial period Λ_{LSFL} of *LSFL-I* is linked to the spatial period of the modulated electromagnetic field Λ_{SPP}, through the relation $\Lambda_{LSFL-I} = \Lambda_{SPP}$.
For a plane air-metal interface, under normal incident radiation, Λ_{LSFL-I} can be calculated as follow:

$$\Lambda_{LSFL-I} = \Lambda_{SPP} = \lambda Re\left\{\sqrt{\frac{\epsilon_m + 1}{\epsilon_m}}\right\} \tag{1.8}$$

where λ is the radiation wavelength. The relation in Eq.(1.8) must be used carefully: it is valid for experiments employing few number of pulses and for not too deep LIPSS relief [7], [12].

The hypothesis of the excitation of *SPP* may be useful also as a starting point to explain the regularity of LIPSS for different metals. Let us assume to have a metal surface, in the x and y plane, exposed to femtosecond laser pulses in air environment. As mentioned, if the condition in Eq.(1.7) is satisfied, SPPs excitation can occur. Hence, SPPs waves propagate along the surface of the material with a wave number given by:

$$k_x = \pm \frac{\omega}{c} \sqrt{\frac{\epsilon_{air}\epsilon_{sample}}{\epsilon_{air} + \epsilon_{sample}}} \tag{1.9}$$

where ω is the angular frequency of the waves. Since SPPs spread crossing the metal surface, some energy could be loss due to the absorption. From this point of view, a parameter which takes into account these absorption phenomena is introduced: the propagation length (or mean free path) L_{SPP}.
L_{SPP} is defined as the distance beyond which SPPs intensity decays by a factor equal to $1/e$, and it is calculated as follow:

$$L_{SPP} = \frac{1}{2Im\{k_x\}} \tag{1.10}$$

As a first approximation, it can be shown that for metals the mean free path L_{SPP} is linked to the regularity of periodic structures.
In particular the following classes of materials can be identified:

a) Metals with L_{SPP} ranging from $(1 \div 20)$ μm which manifest high regular periodic structures (the ones signed as *HR-LIPSS*);

b) Metals with $L_{SPP} \gtrsim 50$ μm for which periodic structures appear in a not so regular way.

It is interesting to underline that materials with a high optical dumping belong to the first group [a)]; examples are: Mo, Ti, steel.
Materials such as Au, Al and Cu belong to the second group [b)].
Note that the cited metals are related to experiments performed through a femtosecond laser source with a wavelength $\lambda = 1030$ nm. Indeed, it was experimentally demonstrated that with the decrease of the laser wavelength several metals tend to exhibit *HR-LIPSS* such as Au and Cu [18].

Sipe's theory predicts the mechanism underlying *LFSL-II* formation for transparent materials. The theory involves the so-called *Radiation Remnants*, a non-radiative electromagnetic wave, which propagates close to the rough surface. As a result, this wave extracts energy from the incident radiation and transfers it to the material surface at the associated spatial frequencies [8].

It should be highlighted that *LSFL* can also originate in a non-ablative regime. In this case, the optical energy transferred to the irradiated material is not enough to induce material removal from the surface; as a result periodic structures can arise from the solidification of the molten region.

This process may involve many effects such as the action of thermocapillary forces and the occurrence of thermal oxidation, which lead to a spatial redistribution of the material during the melting stage [8], [12].

As regards *HSFL* several theories have been proposed, since the discussion on the subject is still controversial. In 2011 Buivdas at al. proposed a theory for transparent materials according to which *HSFL-I* originate from the nanoparticles held in the plume above the material after the fs laser irradiation, [7].
Apart from hydrodynamical and self organization effects, others mechanisms were proposed such as: the interaction, and thus the subsequent interference, between the incident electromagnetic radiation and the coherent near field scattered at the rough surface and the involvement of second harmonic generation [7], [8].

1.3.2 Matter reorganization theories

Matter reorganization theories rely on the fact that, after femtosecond laser irradiation, the material displays a molten phase after which it cools down and solidifies. During this process transport effects occur and lead to a redistribution of the material that reshapes in a periodic structure pattern. Hydrodynamic effects, material instabilities and microscopic accumulations concur to the above mentioned events for which many theories are proposed; here, we briefly discuss about two of them: *hydrodynamic theories* and *self organization theories*.

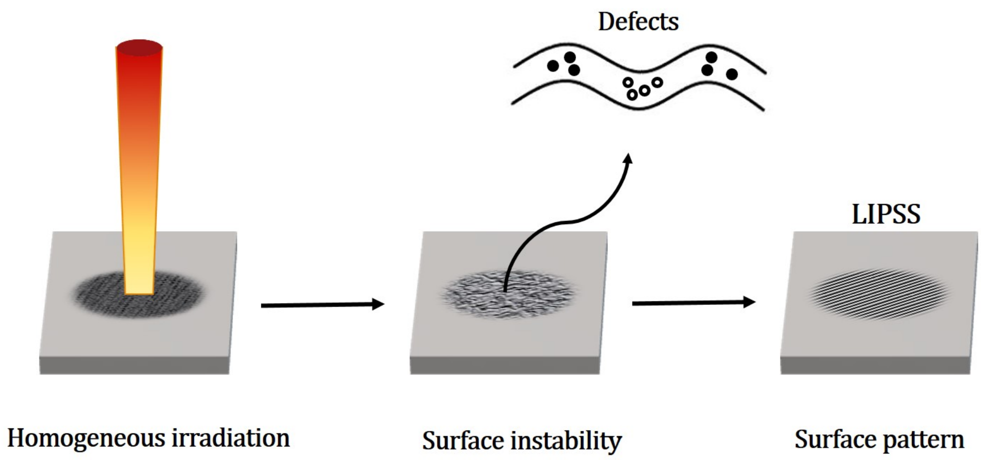

Figure 1.9: Scheme for LIPSS formation through self organization phenomenon.

- Hydrodynamic theories involve the action of surface tension gradients that stretches the melted layer during the transition phase to the solid state. According to the latter, the dynamics of this molten coat is usually dealt with Navier-Stokes equations which describes the motion of a continuous fluid with mass density ρ, dynamic viscosity μ at pressure P. In this scenario, possible attendances by thermoelastically generated surface acoustic waves (*SAWs*) and capillary waves must not be omitted. In particular, the first ones manifest when the absorbed energy deposits into a thin layer of the material and with the contribution of the heat flow, excites *SAWs* at appropriate spatial frequencies; the latter appear thanks to capillary forces during the convective motion of the fluid (*Marangoni effect*) [7];

- Self organization theories are based on the formation of defects (vacancies, voids, displacements) after intense fs laser exposure. These defects are trapped into a layer of thickness *h* of the host material causing its instability, which manifests in a thermal nonequilibrium. As a result, a mechanism for restoring thermal equilibrium is required. This fact leads to the temporal evolution of the elastic thin layer h which results in a self assembled quasi-periodic structure [6]. In Fig.(1.9) an example of the process is illustrated.

1.3.3 Feedback phenomena

Let us assume a material surface exposed to a train of N fs laser pulses at a fixed repetition rate *RR* and of which we vary the number N; there are two possible irradiation conditions :

- *The static configuration*: the train of N laser pulses hits the same point of the target surface;

- *The dynamic configuration*: where a large area is processed through the scanning of the laser pulses across the surface;

In both scenario, depending on N, feedback phenomena occur influencing the LIPSS formation and their morphological features.

Feedback processes are divided into two groups: the *intrapulse effects* and the *interpulse effects*. The former occur when the surface receives a single laser pulse and they may include many effects such as: changing in optical properties, excitation of SEW, generation of defect states (e.g. excitons) and inhomogeneous absorption. The latter manifest during multi-pulses laser irradiation and may involve: topographical and morphological changes, self-organization phenomena and chemical changes.

Moreover, it should be noted that a single laser pulse without any doubt changes surface morphology, but for gaining regular periodic structures it is necessary acting with several number of pulses [12], [18].

1.4 Control of LIPSS and applications

The manufacturing of nano and micro structures by fs laser pulses, is one of the most versatile techniques which allows to process a large variety of materials suitable for a wide range of applications, such as: photonics, biology, medicine, tribology, electronics, and so on.
The great capability to be such a flexible technology justifies both the active research in this field and the increased demand from industry. Moreover, this versatility is reinforced by the quick and easy manipulation of the parameters which make possible the realization of LIPSS [6], [12], [67].

The key factors we are talking about are:

- **Laser wavelength** λ: as we have seen in Sect.(1.3) LIPSS period is strictly related with the laser wavelength. It is usually observed that Λ_{LSFL} scales linearly with λ. It should be noted that there is a lower spatial limit for the periods depending on the processes; it is widely accepted it is caused by the optical relaxation during the transfer of energy from the electronic system to the lattice [8], [12].

- **Number of pulses** N: surface modifications can occur by a single laser pulse, however to obtain regular periodic structures an increase of the number of pulses is required, thus leading to feedback phenomena [see Paragraph. (1.3.3)]. It has been experimentally seen that for metals and semiconductors an increase of N leads to a decrease of Λ_{LSFL}; for dielectrics the opposite phenomenon takes place. For *HSFL* it seems that there is not a strong correlation with N [10], [12];

- **Polarization**: as we discussed in Sect.(1.3), the orientation of LIPSS is linked to the polarization of the laser beam. This correlation was experimentally demonstrated through the irradiation of a solid sample through optical vortex beams characterized by different polarization states (radial, azimuthal, and spiral-like) [8], [12], [39].

- **Peak fluence**: local fluence is crucial for LIPSS generation. A material could show characteristic LIPSS for a selected value of fluence which does not occur at others. Therefore, for each material there are certain values of fluence at which different types of structures appear (e.g. *ripples*, *spikes*, *grooves*), [12].

- **Angle of incidence** θ: the angle formed between the incident laser beam and the irradiated material also affects the morphological changes of the surface. In particular, *LSFL* strongly depend on θ; while $HSFL$ show a weaker correlation [12];

- **Local environment and room temperature**: the medium which surrounds the material surfaces also affects the period of LIPSS. In particular it has been shown

that in air and in vacuum there are not substantial changes in LIPSS period, while in liquids (e.g. water) a reduction of about $100\ nm$ is observed.
Moreover, the temperature T of the room influence LIPSS formation, since the linear absorption coefficient α of the material is sensitive to T [10], [12].

Hereafter we illustrate many effects obtained through fs laser structuring and suitable for several technological applications.

Antibacterical surfaces - LIPSS can be suitable for medical applications: they can be used to reduce the bacterial attachment on material surfaces.
For instance, on LIPSS-covered titanium alloy it was demonstrated a decrease of *Staphylococcus aureus* bacteria adhesion, allowing in this way to obtain safer prothesis since titanium is one of the most used material for their realization.

Other experiments report the influence of LIPSS in the growth of biological cells; e.g. it was investigated the proliferation of different cells cultures on polystyrene film for which it was shown that cells align along the direction of LIPSS [8], [12].

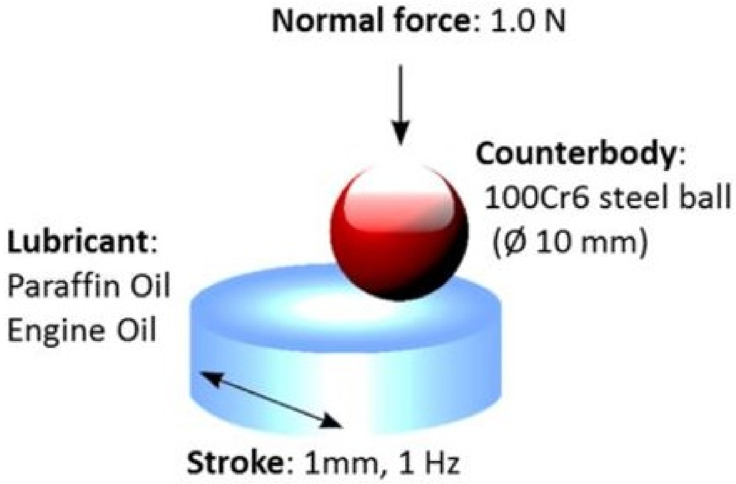

Figure 1.10: Example of a tribological test: a ball of 100Cr6 steel slides in a commercial engine oil against a sample of titanium-alloy, [8].

Modification of mechanical properties: friction and wear - LIPSS find application also in the field of tribology.
The first experiment was carried out in 1999 with a tribological test on the nanostructured NiP and it was found out that LIPSS concur to the reduction of friction and wear with respect to the unstructured one [8], [12].
Futhermore, many tests performed on several metals confirm this trend. For example,

in the one shown in Fig.(1.10) a ball of 100Cr6 steel slides in a commercial engine oil against a sample of titanium-alloy first nanostructured and then unstructured to check the difference of the friction coefficient [8], [12].

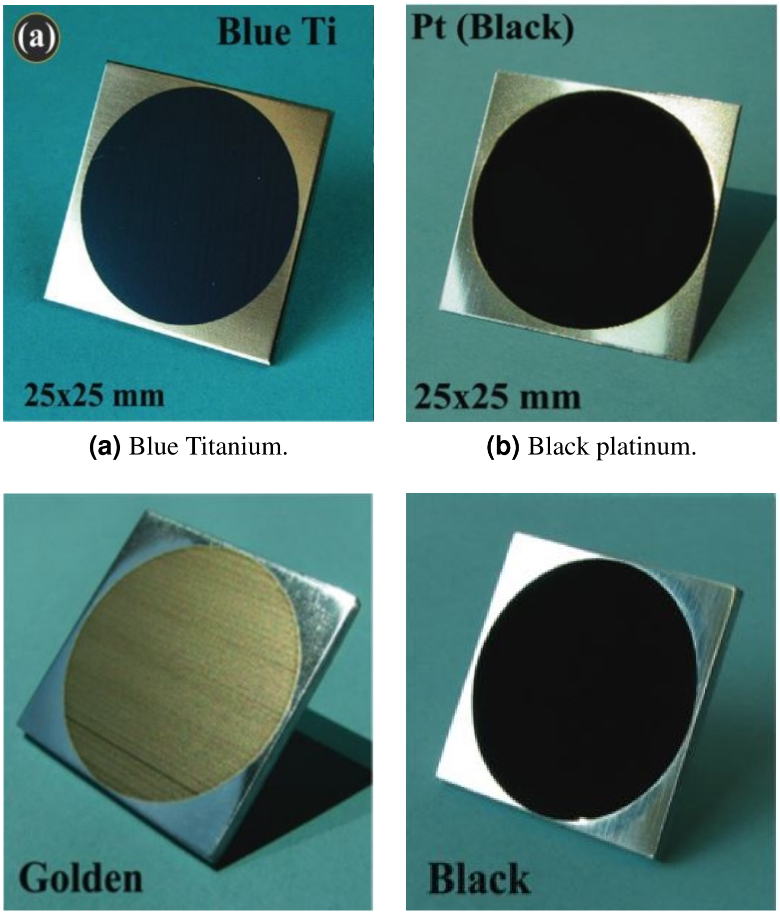

(a) Blue Titanium. **(b)** Black platinum.

(c) Golden aluminium. **(d)** Black aluminium.

Figure 1.11: Nanostructured metals displaying different colors with respect to the ones we are used to see [67].

Modification of optical properties: the structural color - Material surfaces exhibit different types of colors not only for the presence of pigments, but also for scattering and diffraction events which occur due to the interaction with the light of the environment. Thus, surfaces act as diffraction gratings, light scattering structures and thin-film reflectors.

From this point of view it is understandable to expect that surface modifications lead to a change in the structural color of the sample. Hence, the generation of LIPSS becomes a method to change optical properties of materials and gain some with different

colors from what we are used to see.
This effect was observed for the first time on metals irradiated with fs laser pulses and with the generation of LIPSS it was possible to obtain: blue titanium, black platinum, golden and black aluminium [Fig.(1.11)] [67].
The control of color by LIPSS would be useful in many application such as cryptography, optical data storage, decoration [8], [12].

Other applications - In the previous paragraphs we have discussed some applications of LIPSS in different fields; however, others ones are reported in literature. LIPSS also can be used to: enhance Raman signal in *SERS* technique; improve both X-ray emission from surface and thermal emission from tungsten lamps; turn hydrophobic surfaces into hydrophilic ones and vice versa; investigate superconducting and magnetic properties of metals [6], [12], [67].

Chapter 2

Experimental Setup

This chapter presents the experimental setup employed in this thesis work. The Sect.(2.1) describes the typical setup used in direct fs laser surface structuring, with the focus on the cylindrical and spherical lenses used to focus the beam. The discussion continues with the description of the scanning electron microscope (SEM) [Sect.(2.3)] and the optical microscope (OM) [Sect.(2.4)] used to characterise the morphological features of the generated structures.

2.1 Experimental setup for femtosecond laser surface structuring

The experimental setup employed in this work consists in two fundamental parts:

a) The laser system and accessories for surface processing;

b) The optical microscope (OM) and the scanning electron microscope (SEM) for the morphological analysis of the nanostructured samples.

Fig.(2.1) displays a sketch of a typical experimental set up for laser surface processing.

The laser system produces fs pulses that are focused onto the surface of the target material through a lens. The sample is located perpendicular to the laser beam and mounted on a computer-controlled translation stage that allows to move it along x and y directions. The z direction is fixed and adjusted in correspondence with the lens focus or another appropriate position and it can be manually or computer controlled. This type of equipment enables to work both in the static and dynamic configurations. The energy of the laser pulse is controlled by a system composed of a half wave plate and an attenuator, whereas an electromechanical shutter fixes the number of pulses for the generation of spots (static configuration) or blocks the laser beam in raster scanning for the texturing of large areas (dynamic configuration).

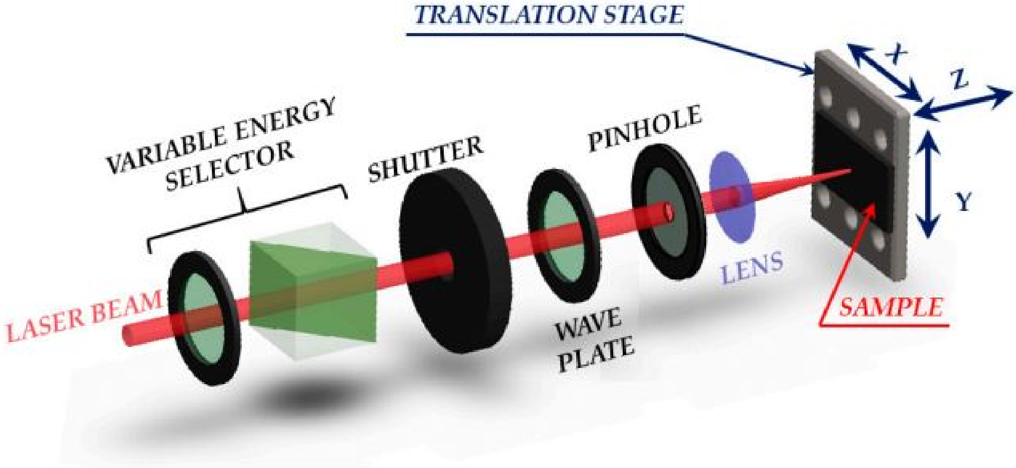

Figure 2.1: Scheme of the typical experimental setup for fs laser surface structuring [38].

A wave plate and a pinhole are respectively used to control the laser polarization and reduce any possible laser distortions and aberrations, besides selecting the most intense part of the beam; a powermeter is also used for monitoring the energy of the beam [38], [67].

In this thesis work the laser source is a chirped pulse amplification Yb:KGW system providing pulses with a duration of $\tau \sim 180\ fs$ at a central wavelength of $1030\ nm$. The system is equipped with a harmonic generator unit that allows producing beams at other wavelengths. The experiments were carried out by using both the fundamental output at $1030\ nm$ and its second harmonic at $515\ nm$. The laser system is provided with a pulse selector capable to define a train of laser pulses with any value of the repetition rate RR up to that of the Regenerative Amplifier (RA). The regenerative amplifier is used for the amplification of ultrashort light pulses and consists of an optical resonator within that there is a gain medium. The operating principle can be explained as follow: first the gain medium is pumped and depending on the pump, the amplifier can work at determined repetition rates; moreover, the higher is the repetition rate, the lower will be the energy per pulse. Subsequently, the incoming pulse is trapped in the resonator and undergoes many round trips until it extracts all the energy stored in the gain medium. In this way the pulse is amplified and after that it leaves the cavity [48].

In our system the pulses reach a maximum energy of $\sim 1.5\ mJ$. In the experiments involving the study at various RR, some issues must be taken into account if the RR selection is done by the RA switching. For example, apart from that the energy per pulse is reduced with the increase of repetition rate, the features of the laser beam itself could be modified. To overcome such an issue a *pulse picker*, integrated within our system, is used. The pulse picker works as an optical divider, i.e it permits to select certain pulses from a pulse train. A pulse picker comprises: (i) a Pockels cell which manipulates the polarization state, (ii) a polarizer that enables the pulses either to pass or to be blocked. Such a method assures to have a stable laser source with the same energy per pulse during the experiment (apart from any statistic fluctuations), however it limits the energy to a maximum value; e.g. if the maximum power delivered from the laser source is $2\ W$ at $RR = 200\ kHz$, then the maximum pulse energy is $E = 10\ \mu J$ [1], [42].

The experiments were carried out irradiating copper targets in air. The Cu target consists of a polycrystalline copper OFE (Oxygen-Free electronic grade) metal sheet of $1\ mm$ thick that is cut into a size of $2\ cm \times 2\ cm$. The target underwent a standard procedure for UHV cleaning, including a wet-chemical detergent based degreasing process followed by rising in deionized water. Due to its excellent thermal and electrical properties, good machinability and high corrosion resistance, copper is one of the metals widely used in industrial applications, e.g. it can be suitable for making wiring systems, high conductivity cables, transmission lines etc. In particular, copper has wetting properties which can be improved with fs laser treatments involving LIPSS formation. It has been shown that the generation of periodic structures on copper allows to gain high hydrophobic surfaces exploitable to: enhance heat exchangers, improve water-resistant electronics, modify and control oxidation of the materials, etc. [2].

However, beyond all these considerations, the present work on copper samples fits into a broader and new panorama related to the reduction of secondary electrons emission in high-energy colliders. When two beams of particles collide at high speed and energy, photoemission and secondary emission phenomena occur leading to some unwanted effects in the high-energy particle accelerators. One of these effects is the formation of electron clouds by secondary electron emission from the walls of the system, typically made of Cu, which affects the stability of the beam itself causing it to degrade and damage.

From this point of view, the structural modification of the beam chamber is one of the approach that can be followed in order to cope with to such an issue. In particular, laser surface texturing has been considered in some works [14], [15], [64], [65]. In this respect, surface structuring with fs laser pulses is still scarcely investigated [40]. However, femtosecond laser treatment on the chamber surface might be one of the techniques deserving attention that might enable reaching such an achievement. Ref.[40] reports an interesting study performed on two types of copper targets (OFC and POFC, differing each other in the treatment of their surface) structured with a fs laser source. What the authors have shown is that the generation of LIPSS on copper surfaces leads to a reduction of the *secondary electron yield* (SEY) δ, i.e the parameter through which one can control the quantity of the emitted electrons: $\delta = I_{SE}/I_{PE}$, where I_{SE} is the current of secondary electrons emitted and I_{PE} is the current of incident primary electrons.

An important result regarding SEY is its dependence on the morphology of the surface; in fact, it has been experimentally demonstrated that ripples arising from a linearly polarized fs laser irradiation are more efficient for SEY mitigation than those generated by a circularly polarized beam (recall that polarization is one of the parameters that influences the appearance of LIPSS Sect.(1.4)). The reduction of SEY gained in the research in Ref.[40] is not high enough to completely avoid the electron clouds formation in particle colliders since it requires a value of $\delta \leq 1$, while the one obtained is almost $\delta = 0.91$. However, the mentioned work lays the foundations for new studies in this field, in particular the present work thesis fits into this context.

In the current experiments, the surface structures were generated by both the static and dynamic irradiation of a copper sample. In the former case, the laser light was focused in air through both plano-convex spherical and cylindrical lenses with focal lengths of 200 mm and 150 mm respectively. By using the spherical lens, the Cu sample was irradiated at $\lambda = 1030\ nm$ with a sequence of $N = 200$ pulses and by varying: the repetition rate in the range $(3 \div 30)\ kHz$ and the pulse energy in the range $(30 \div 60)\ \mu J$.
By using the cylindrical lens, several spots of elliptical shape were produced with a train of $N = 200$ pulses at the repetition rate of $5\ kHz$. The sample was irradiated with the laser source at the central wavelength of $\lambda = 1030\ nm$ and at its second harmonic of $\lambda = 515\ nm$. In both cases we varied the energy of pulses: for the IR light the energy variation window is $(356 \div 506)\ \mu J$ whereas for the green light it is $(94 \div 197)\ \mu J$.

In the case of the dynamic configuration, the laser beam was focused onto the copper surface by a plano-convex cylindrical lens. The laser surface structuring was carried out across a millimeter size area by moving the translation stage, where the target is located, at velocity v_s. We selected four scanning velocities in the range $v_s = (0.1 \div 2.0)\ mm/s$. The areas were processed by writing a continuous pattern of parallel lines along the horizontal direction, separated by a shift along the vertical direction of which we varied the step. The laser was operated at a repetition rate of $RR = 5\ kHz$ and $\lambda = 1030\ nm$. The energy per pulse was fixed and it was about $180\ \mu J$.

The laser surfaces processing, as well as, the investigation of the morphology of the nanostructured samples by means of the optical microscope (OM) were carried out at "Dipartimento di Fisica Ettore Pancini". The morphology of the generated structures has been also analysed by means of the scanning electron microscope (SEM) at Laboratorio MUSA" of CNR-SPIN Institute (located in Salerno, Dr.Antonio Vecchione).

The measurements of the structural features of the processed samples were performed with the open source program ImageJ [37], while the bidimensional Fast Fourier Transform (2D-FFT) maps of the SEM images were elaborated with Gwyddion software [36].

2.2 Spherical and cylindrical lenses: an overview

In the previous section, it has been underlined that the laser beam was focused on the material surface through a plano-convex spherical lens ($f \sim 200\ mm$) and a plano-convex cylindrical lens ($f \sim 150\ mm$). This paragraph gives a brief overview of the advantages between these two approaches. A spherical lens is an optical element with almost a curved surface that causes the beam to converge or to diverge. In particular, a plano convex lens is a converging (or positive) lens which features a spherical surface on one side and a flat surface on the other. It is commonly used in the optical systems and in our interest, it has been employed to focus the laser beam at single point placing the flat surface opposite to the sample (the focal plane) and the spherical surface in front of the beam (the infinite conjugate plane) to reduce aberration effects.

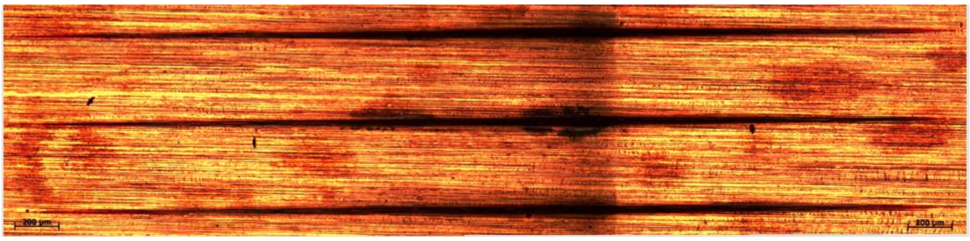

Figure 2.2: Lines generated on a copper sample by focusing a fs laser beam ($\lambda = 515\ nm$) with the cylindrical lens.

A spherical lens is usually defined by a single radius of curvature that guarantees a certain symmetry, i.e by rotating it, the shape and the orientation of focused point should not change. However, as every curved surface, it is affected by spherical aberration that causes the light to focus in different points on the optical axis. From this point of view, a cylindrical lens may suitable to solve such an issue since it is curved only in one direction. A cylindrical lens is obtained by cutting a glass cylinder with a plane parallel to the axis of rotation. Therefore, it has two different radii along x and y directions which lead it to produce a magnified image only in one axis. Moreover, this shape makes it not fully symmetrical i.e the mode through which the light is transmitted depends on the orientation of the lens.

In the present work, we used a plano convex cylindrical lens to focus the laser beam along a line on the sample surfaces [Fig.(2.2)]. The choice to exploit a cylindrical lens lies in the fact that it enables to texture larger and bigger areas in less time rather than spherical lenses.

2.3 The scanning electron microscope SEM

Due to its high resolution, the scanning electron microscope (SEM) is one of the most used instrument for the investigation of sub-micrometer morphological features [Fig.(2.3)]. The operating principle is based on the interaction between the target and the electron beam scanned over its surface.

Moreover, the scanning electron microscope can be suitable also for the chemical analysis of the samples, implementing it with the X-ray energy dispersive spectrometer (EDS), [24].

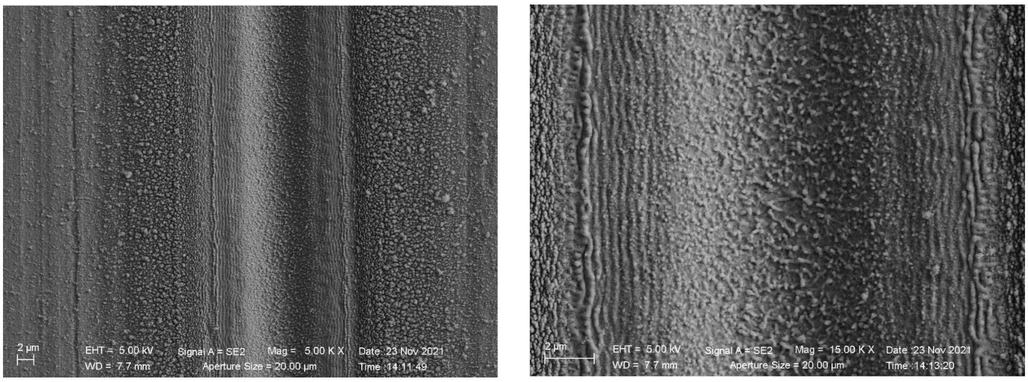

(a) Central part of the elliptical crater generated through a cylindrical lens: it is possible to recognize the ablated region and the deposited nanoparticles clearly.

(b) Enlarged image of the figure on the left; here it is easy to distinguish the peripheral area where ripples are formed and the excavated central region that features peculiar texture.

Figure 2.3: SEM images of a structured surface of copper generated by an irradiation sequence of $N = 200$ pulses, at pulse energy $E = 140\ \mu J$, $RR = 5\ kHz$ and $\lambda = 515\ nm$, in the frame of this work.

The microscope consists in two fundamental parts:

a) The electronic console through which one can control and adjust the intensity, the focus and the magnification of the images on the display screen;

b) The electron column where the electron beam is produced and sent to the target placed on a motor stage in a vacuum chamber.

Figure (2.4) shows a sketch of the electron column with its components, that are briefly described [24], [29].

- **The electron gun**: at the top of the column, it provides the electron source either for the thermionic effect or via field emission effect. Three parts compose the gun: (i) the hot filament which ejects electrons; (ii) the Wehnelt cylinder that controls the number of the emitted electrons; (iii) the anode responsible of accelerating electrons. To reduce any possible effect of interaction between the beam and the external environment, the electron gun is inserted in a vacuum chamber different from the one where the sample stands.
  The electron beam usually reaches voltage from $1\ kV$ up to $40\ kV$.

- **Electron lenses**: are distinguished in two types (i) the condenser lenses closest to the gun; (ii) the objective lens nearest to the sample. The former reduce the diameter of the electron beam down to $\sim 10\ \mu m$, the latter focuses it as a probe on the target with a spot of nanometric dimensions. In addition, a platinum disk is inserted near the objective lens in order to limit aberration effects and improve the depth-of-field of the images.

- **The scanning system**: provides the scanning of the electron beam along the surface of the specimen. It consists of a deflection system integrated with the objective lens and monitored by two pairs of electromagnetic coils (*scanning coils*).

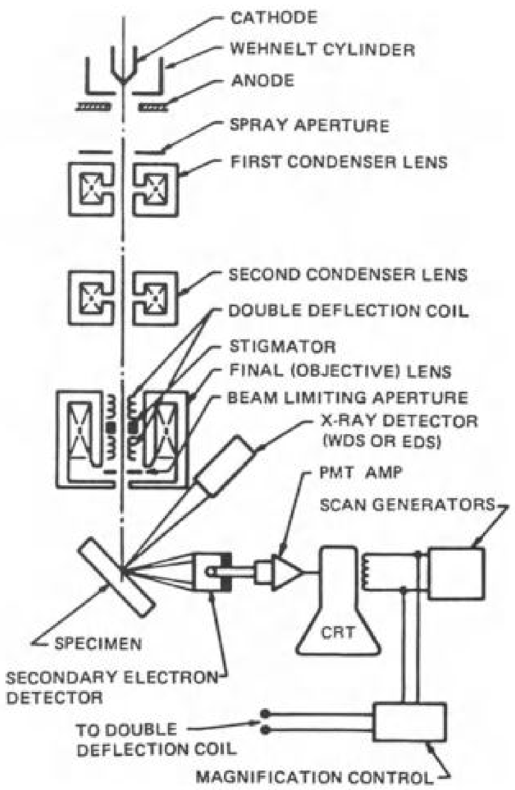

Figure 2.4: Scheme of the electron column and its components, [29].

After the scanning process, the electrons emitted from the sample are collected by a detector, amplified and used to reconstruct the image at the screen. In particular, the image is formed as result of a one-to-one correlation between the points on the screen of a cathode ray tube (CRT) and the scanned points on the target.

As above mentioned, SEM requires a vacuum system which allows to: preserve the source from the environment, secure the path of the electrons on long distances and isolate the target in order to avoid interactions among the air particles and the electrons released during the process.
Hence, rotary and a turbo-molecular pump in series are commonly used to ensure a clean environment. The rotary pump allows to gain vacuums of $\sim\ 10^{-2}\ mbar$ (*rough vacuum*) starting from the atmospheric pressure; the latter produces vacuums of the order of $10^{-3} \div 10^{-6}\ mbar$ (*high vacuum*).
Moreover the vacuum chambers are controlled by a locking system: when the chamber of the sample is opened, the one of the source is closed avoiding the tungsten filaments to burn owing to the difference between pressures.

In the following some details about the electron source, the detection system and the imagine acquisition are provided.

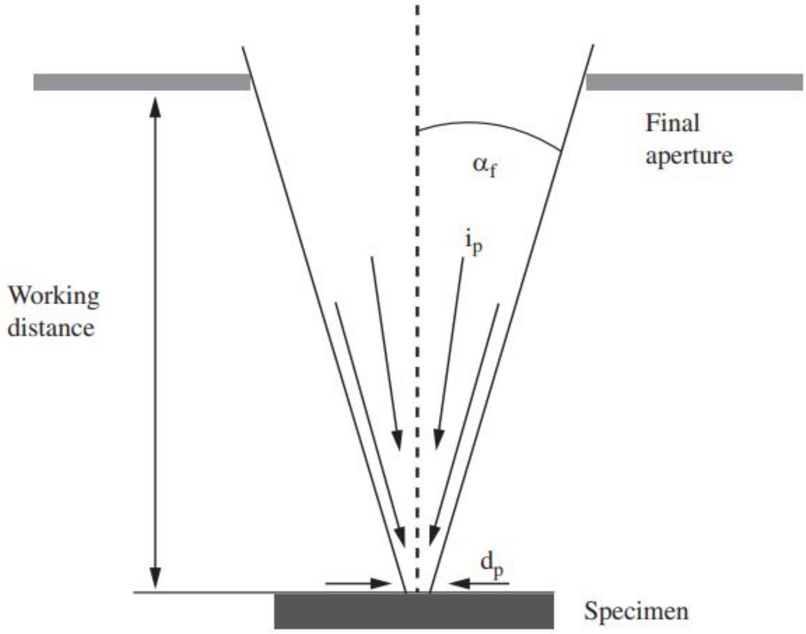

Figure 2.5: Scheme of the longitudinal section of the electron beam with its main features: the working distance, the angle of aperture α_f, the diameter d_p and the current i_p [24].

2.3.1 The electron source and the electron beam parameters

In Section (2.3), it has been emphasized that one of the main component of the microscope is the gun which generates the electron beam. According to the physical phenomena involved, there are two basic types of guns:

a) *The thermionic emission gun*, which uses a tungsten or a LaB_6 filament as source and exploits the thermionic effect. Indeed, the filament is heated at high temperatures by the passage of electric currents (*Joule effect*).
As a result the electrons in the conduction band overcome the potential barrier and leave the surface. After that, imposing a voltage between the filament and anode, the electrons are accelerated towards the electrical lens system.
Although LaB_6 requires vacuum higher than tungsten, modern microscopes prefer to use it as cathode since its working function is smaller than the tungsten one, enabling to produce electrons with weaker currents [24].

b) *The field emission gun* operates with the application of an intense electromagnetic field to a metal tip (with a diameter of $\sim 100\ nm$) typically composed of a tungsten crystal. In this case, electrons exceed the energy barrier due to the tunnelling effect. The beam intensity produced through this method is about 10^4 orders of magnitude higher than the previous one.

The field emission gun can work in two opposite modalities: at high temperatures (*thermal gun*) and at low temperatures (*cold gun*). The first case generates a beam of large stability and few noise; the second case engenders a beam with low energies (useful for preserving the sample), but very sensitive to air ions.
Furthermore, even the tip is affected by the local environment (i.e residual ions generated from the emission) which can cause it some oxidation; for this reason the maintenance of the tip is necessary.

The generated electron beam features a current (i.e *probe current* i_p) ranging from picoamperes (pA) to microamperes (μA) and has a diameter d_p whose size determines the resolution of the images [see Paragraph (2.3.3)]. In particular, the diameter depends on two important parameters *the beam convergence angle* α_f and *the brilliance* β [Eq.(2.1)].
The beam convergence angle represents the angle of objective aperture and it is strictly correlated to the working distance, i.e the distance between the sample and the objective lens [Fig(2.5)].

$$d_p = \sqrt{\left(\frac{4i_p}{\beta\pi^2\alpha_f^2}\right)} \tag{2.1}$$

The brilliance (or brightness) is a coefficient that enables to evaluate the current at different points of the SEM column; in fact it is defined as the current for the unitary solid angle ($Acm^{-2}rad^{-1}$) [24], [29].

2.3.2 Interaction with the sample and detection system

The electrons rising from the material surface, and employed for SEM analysis, are of two kinds: the backscattered electrons (BSEs) and the secondary electrons (SEs).

- The backscattered electrons are produced from the elastic scattering among the incident beam and the atoms of the specimen. This entails that the energies are close to that of the electrons of the beam (preserving the $60 \div 80\%$) and that BSEs are deflected on large angles;

- The secondary electrons emerge with the inelastic scattering between the beam an the target. In this case, an incident electron transfers part of its kinetic energy to an electron of the atom of the sample, causing the latter to eject from its orbital and thus become a secondary electron. This process involves a considerable loss of energy and generates electrons with energies in the range of $(3 \div 5)\ eV$ and scattered at small angles.

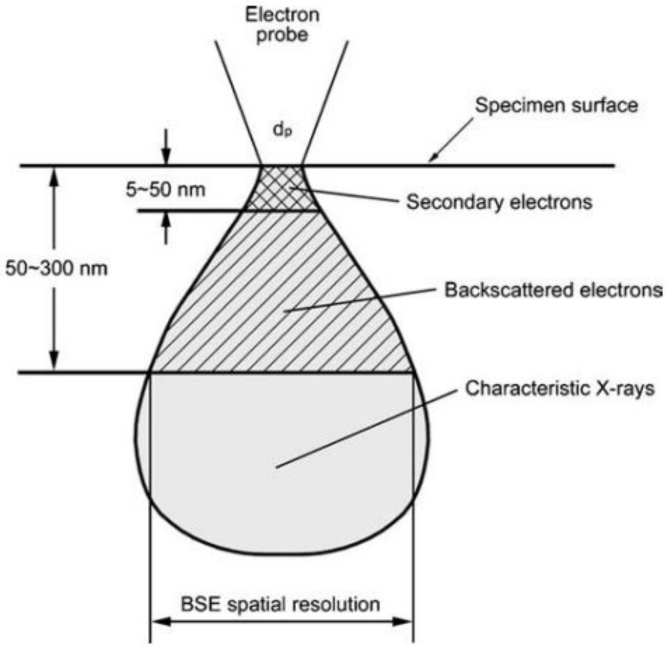

Figure 2.6: Interaction zone between the specimen and the electrons of the beam, [24].

The interaction zone is usually schematized as a drop-shaped region, in which one can distinguish three main parts: (i) the first related to the secondary emission of the electrons, (ii) the second associated to the backscattered electrons, (iii) the last linked to the production of characteristic X-rays, involved in the chemical analysis of the sample. As indicated in Fig.(2.6), the secondary electrons that can actually be detected are the ones that reach depths of $(5 \div 50)\ nm$ below the surface of the sample; on the contrary due to their higher energies the backscattered electrons, useful for the detection, extend on lengths larger then the previous ones, ranging from $50\ nm$ to $300\ nm$, [24].

The detection system is typically constituted by a *Everhart-Thornley detector* [Fig.(2.7)] that allows the observation both of the BSEs, which usually travel directly toward it, and of SEs that are instead deflected towards the detector.

The detector [see Fig.(2.7)] is equipped with a Faraday cage (FC) charged negatively or positively; in particular, if it has a positive charge it mainly collects secondary electrons, but if it has a negative charge it rejects these ones with energy lower than $\sim 50\ eV$. The detected electron signal goes to a scintillator which transforms it into photon signal that travels across a light guide and reaches the photomultiplier tube where the signal gain increases up to $\sim 10^6$.
The output of the photomultiplier is amplified and displayed onto the screen, [29].

The images revealed at the screen may exhibit different features depending on the type of detected electrons. Indeed, there are two kinds of contrasts:

1) **The topographic contrast** - It is usually obtained with the detection of SEs, even

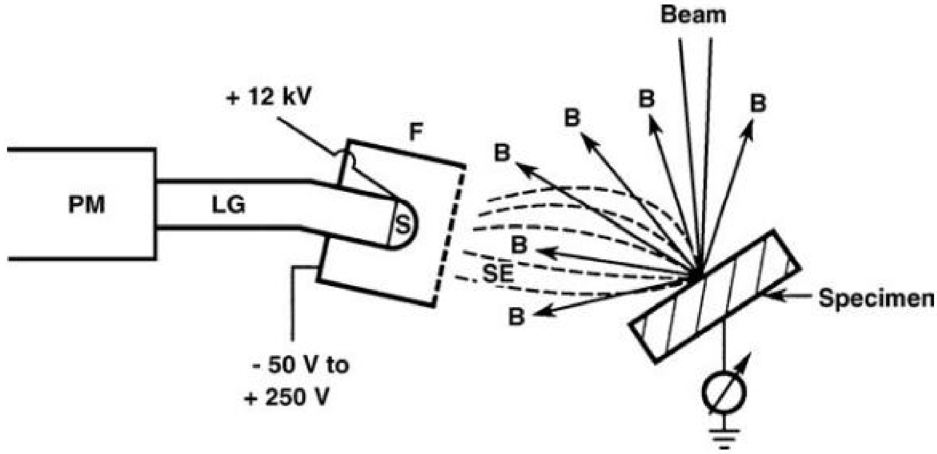

Figure 2.7: Scheme of a Everhart-Thornley detector: the arrows indicate the trajectory of the backscattered electrons (BE), dashed lines trace the path of secondary electrons (SE), F stands for Faraday cage, S is the scintillator, LG denotes the light guide and PM is the photomultiplier [24].

if also BSEs can contribute to these images. As the word itself suggests, topographic images relate with the morphology of the surfaces and depend on two phenomena: the trajectory effect and the electrons number effect. The first refers with the orientation of the surface target with respect to the detector; in particular, if the electrons emitted from a certain zone do not face the detector the image features dark regions. The latter is linked to the ejection of electrons at some angles, i.e if the probe hits a flat surface then fewer electrons escape from the material, but if the probe strikes a surface with a pronounced curvature or a raised area, then more electrons are emitted. In this way, according to the two regions, the images feature safer areas and brighter zones [24].

2) **The compositional contrast** - It is typically linked to the detection of BSEs and refers to the chemical composition of the sample. It should be noted that the chemical analysis provided through this method is only qualitative and not quantitative, i.e the SEM is not capable to recognize a specific chemical element even if it gives and idea of the different material composition, colouring the resulting images with distinct shades of gray.

   The dependence of the atomic species on the backscattered electrons lies in the fact that the capability of emission is correlated to the atomic number of the specie; thus the greater the atomic number, the more electrons will be emitted. This corresponds to brighter areas in the images. [24].

2.3.3 Quality of the images: the control of resolution and depth of field

To obtain the desired image, one should be able to control two important parameters: the resolution and the depth of field, i.e the distance beyond which the focus of the image is lost.

The resolution of the images is affected by the several factors, one of them is the probe size; in particular, to achieve high resolution it is necessary to reduce the beam diameter d_p. Recalling Eq.(2.1), it can be noted that an increase of β (brightness) as well as of the aperture angle α_f, will minimize the probe diameter d_p. The brightness can be controlled by varying the acceleration voltage of the electron gun V_0, since $\beta \propto V_0$, while the aperture angle can be adjusted through the working distance. However, it is prominent to be careful when one modifies α_f since a large aperture angle could introduce some spherical aberration, therefore the optimization of this parameter is required.

Another important feature to gain high resolution is the regulation of the probe current that must necessarily be larger than the background noise of the electrons due to the quantum fluctuations of the beam and the amplification of the detection system. The resolution is also limited by the pixel size of the screen; indeed, one can estimate it by the pixel size and SEM magnification M (ranging from $20\times$ to $100.000\times$) ratio [24].

The depth of field D_f is mainly affected by the angle of aperture α_f and the working distance [Fig. (2.8)]. The relationship between these parameters is given by Eq.(2.2).

$$D_f = \frac{2R}{tan(\alpha_f)} \tag{2.2}$$

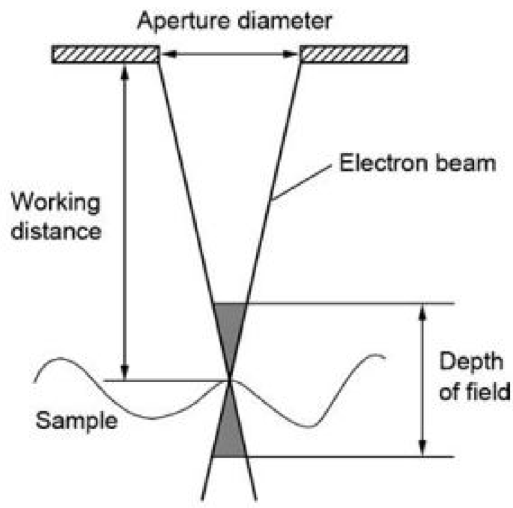

Figure 2.8: Representation of the depth of field D_f, the working distance D_w and the aperture size [29].

where R is the resolution. Assuming that α_f is small enough that $tan(\alpha_f) \sim \alpha_f$, in turn the angle of aperture can be written as a function of the aperture radius r_{fap} and the working distance D_w, thus D_f can be expressed as follow:

$$D_f = \frac{2RD_w}{r_{fap}} \tag{2.3}$$

Equation (2.3) proves that an increase of the working distance and a decrease of the aperture size results in an enhancement of the depth of field. However, once again care must be taken since a small aperture size reduces the probe current and so the signal to noise ratio, whereas a long working distance diminishes α_f worsening the resolution. Therefore, the best configuration for getting high quality images should be the selection intermediate aperture size and working distance.

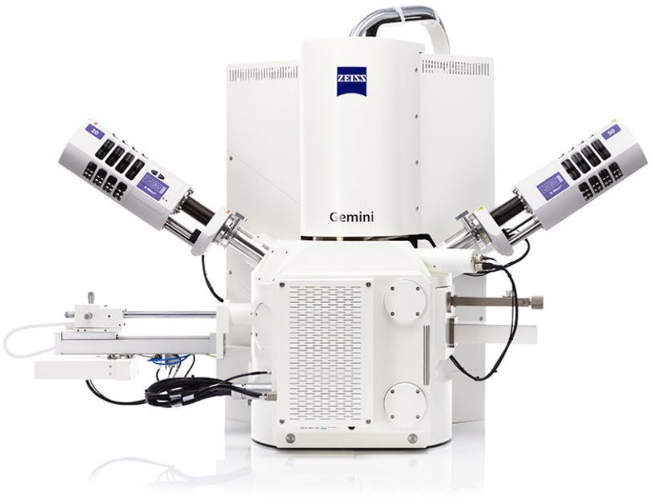

Figure 2.9: Representation of an FE SEM from Zeiss Σigma, [21].

The microscope used in this work for the analysis of the samples is a FE SEM (i.e Field Emission SEM) from Zeiss Σigma model [Fig.(2.9)].
The system is equipped with two detectors: one for the collection of BSE placed perpendicular to the sample and one for the detection of SEs positioned at 45 degrees with respect to the normal to the sample. The former is an Everhart -Thornley detector, the latter is an In-Lens (IL) detector. The In-Lens detector is located inside the electron column of the microscope and it is usually used to register SEM images at high contrast.
The samples have been inserted in a vacuum chamber provided with a specimen holder which supports up to nine targets [Fig.(2.10) (b)]; however, it is important to note that before inserting a sample into the SEM chamber a specific preparation is required.

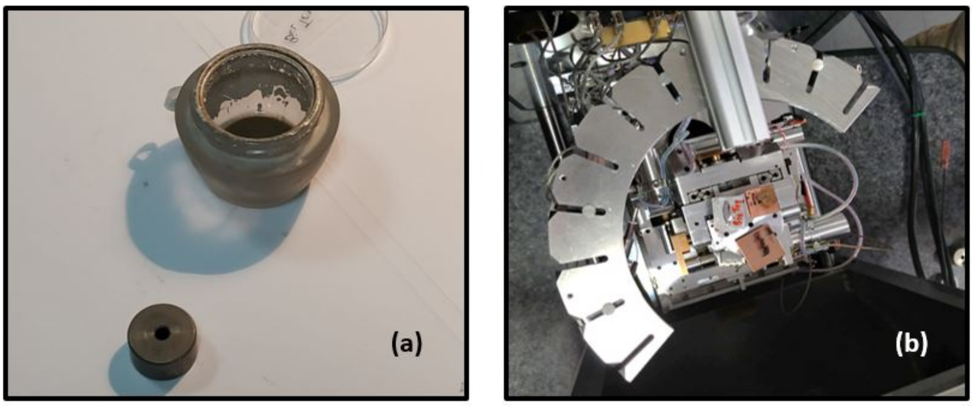

Figure 2.10: Preparation of the samples before inserting them in the SEM chamber: panel (a) shows the silver glue used for the connection to the ground, panel (b) displays the specimen holder, with the two copper samples.

Indeed, during the operation of the SEM, the specimen may become negatively charged and provoke deviations of electrons that would ruin the image. In order to prevent this effect, the sample is connected to ground by a conductive connection which directs the excess current towards an electrical ground through the specimen stage, [29].

In our case we used a silver glue which was attached on the surface facing towards the sample holder [Fig.(2.10) (a)]. Once the sample was prepared and the chamber closed, a vacuum of $\sim 10^{-6} mbar$ (*high vacuum*) was generated through a series of rotative and turbo pumps.
The electron beam operated with an acceleration voltage $EHT = 5\ kV$, an aperture size of $\sim 20\ \mu m$ and a working distance $D_w \sim 7.8\ mm$.

2.4 The optical microscope

In this section we briefly introduce the optical microscope (OM) which it has been employed for the analysis of the nanostructured samples [Fig.(2.11)].

The main components of the microscope are reported below.

- **The illumination system**: the light for the observation of the samples is provided by an electrical lamp.
  Depending on the light spectrum and the color temperature, the lamps employed in the microscope can be (i) a low voltage tungsten filament bulb that guarantees a continuous spectrum with wavelengths ranging from $300\ nm$ to $1500\ nm$ and a low color temperature (blue), (ii) tungsten-halogen bulb which also ensures a continuous spectrum, but compared to the previous one it provides a brighter light source and a higher color temperature (red-yellow), (iii) gas discharge tubes which can be filled both with mercury (with discontinuous spectrum) and xenon (with continuum spectrum) that allows to obtain high colors temperature.
  Moreover, the tungsten-halogen and gas discharge lamps are prone to heating, therefore a system of cooling is required [24].

- **Objective lens and the eyepiece**: the objective lens is probably one the most important element of a microscope, it provides the first image of the sample and strongly influences both the resolution of the pictures and the magnification of the system. The eyepiece collects the light path during the examination of the microstructures and forms the virtual image on the eye retina.
  The total magnification M of the microscope is given by $M = M_{ob} \times M_{ey}$, where M_{ob} and M_{ey} are the magnifications of the objective lens and of the eyepiece respectively. In particular the eyepiece has commonly a magnification of $10x$, while the one of the objective lens depends on the *numerical aperture* (NA) which is a parameter determined both by the refraction index of the media between the lens and the sample, and the half-angle of the cone of light α entering the objective.

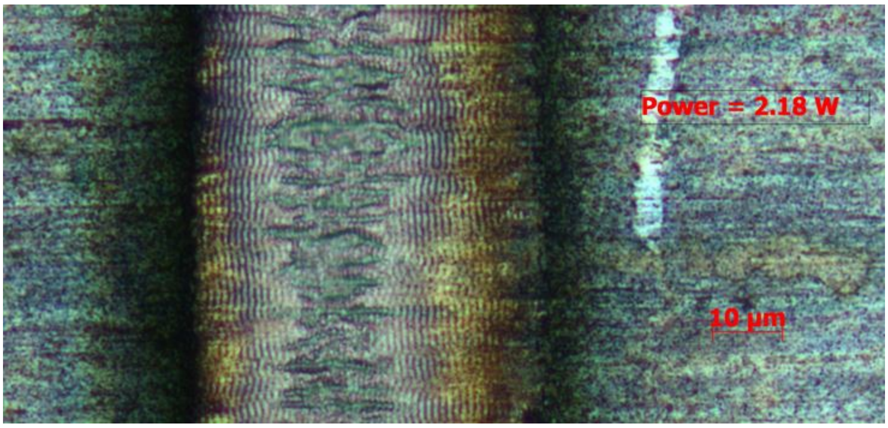

(a) Central part of an elliptical crater generated in air with a fs laser source at $\lambda = 1030\,nm$, $N = 200$, $RR = 5\,kHz$.

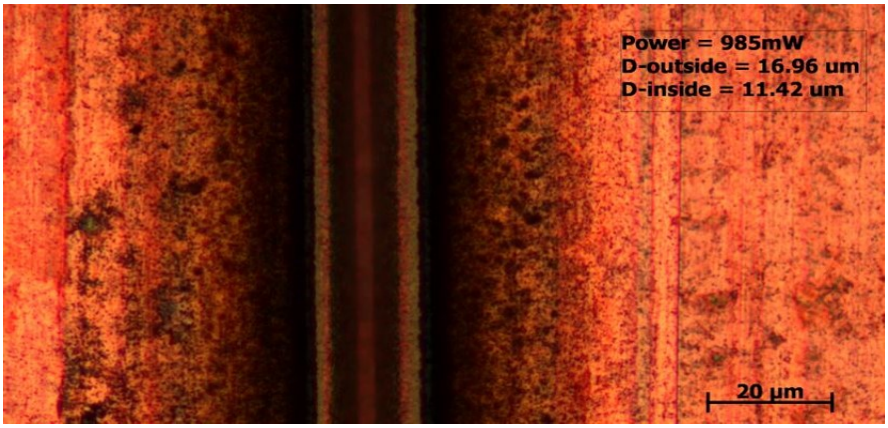

(b) Central part of an elliptical crater generated in air with a fs laser source at $\lambda = 515\,nm$, $N = 200$, $RR = 5\,kHz$.

Figure 2.11: OM images of different copper samples nanostructured after the irradiation with a sequence of fs laser pulses, focused by the cylindrical lens.

Typically the greater the *NA* the higher the M, thus it is common to immerse the lens in a medium that allows to obtain a larger *NA* (e.g. oil).

The types of lens used for the objective are chosen for their ability to correct both chromatic and spherical aberrations, i.e a microscope objective can consist of: (i) achromatic lens, which reduces the chromatic aberration for two wavelengths (red and blue), (ii) semi-achromatic lens that improves the brightness and the resolution of the image, beyond diminishing chromatic and spherical aberration, (iii) apochromatics lens which almost deletes completely chromatic aberration and refines the quality of the images under each point of view [24], [32].

- **The stage**: it is the flat surface where one places the specimen for being examined.

The stage can be shifted along x and y direction to check the points of the sample to analyse and moved up and down in front of the objective to gain the best focus.

A light microscope usually operates in two modalities, i.e collecting either the reflected light (*reflected light microscope*) or the transmitted light (*transmitted light microscope*) from the sample. The first configuration is common for metals, the second for transparent materials.

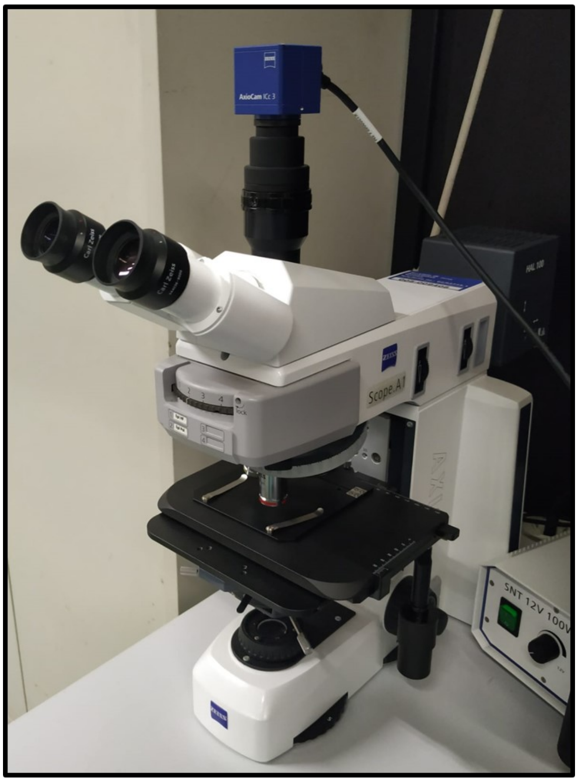

Figure 2.12: Zeiss Axio Scope A1 employed in this framework.

Modern light microscopes have an illumination system comprised of a *collector lens* and a *condenser lens*, this equipment is know as *Kohler system*.
In this system, the light originating from the lamp is gathered by the collector lens towards the condenser lens that in turn collimates the light onto a small area of the sample. The condenser lens allows to attain an uniform illumination onto the sample, moreover its focusing can be adjusted by means of special knobs provided by the instrument. The Kohler system is also capable to generate two *conjugate focal planes*: (i) the conjugate aperture plane which enables to align the optical system, (ii) the conjugate field plane responsible of the image forming. The first is also arranged with an aperture diaphragm through which one can control α to gain the best resolution and depth of field, while the latter has a field diaphragm with which one can limit the area of view and block the scattered light from the sample, that may affect the objective lens [24], [32].

In this thesis work the Zeiss Axio Scope A1 was used for the investigation of the morphological features of the samples [Fig.(2.12)]

The tool operates with the transmitted-light and a reflected-light techniques such as:(i) the brightfield, commonly used in microscopes and based on the collection of light through the objective after the illumination of the sample by an intense ray of light; (ii) the darkfield, used to observe the unstained samples, introduces a condenser below the stage causing the light to diffract at different angles and an opaque object (the "stop") that blocks the central light; hence only the oblique rays hit the sample that

appears brightly in a dark background; (iii) the polarization employed for birefringent materials which uses a polarizer above the sample in order to enhance the direction of light that illuminates the sample and thus gaining the best quality of the image; (iv) the fluorescence which mainly works with biological specimens that emit light (naturally or due a treatment) at a certain visible wavelength. In our case the system worked in brightfield condition.
Moreover, the microscope is provided by five objective lenses with a magnification of $10\times \div 50\times$ and has various illumination source including a 100 watt halogen bulb. The advantage of this tool is given by the possibility of observing the details of the resulting image on a screen due to a high-resolution camera, therefore Zeiss Axio Scope A1 interfaces with the Zeiss Axio Vision imaging software which allows to process, analyse and store the images [53].

Chapter 3

The Gaussian beam model: characterization of circular and elliptical spots

This Chapter provides the estimation of fluence threshold for copper ablation by using the Gaussian beam model introduced in Sect.(1.1). The analysis is performed on the OM and SEM images that exemplify both the circular and elliptical craters obtained by the direct laser structuring carried out in this thesis work.

3.1 Measurements and results for circular craters

In Sect.(1.1) we introduced the Gaussian beam model, pointing out that the generation of several surface structures occurs at certain fluence threshold ϕ_{th}. In order to evaluate this parameter for the nanostructured surface of copper we recall the Eq.(1.6):

$$r_{th}^2 = \frac{w_0^2}{2} ln\left(\frac{E}{E_{th}}\right) \tag{3.1}$$

Eq.(3.1) represents the starting point to: (i) study the dependence of the radius of the ablated regions on the pulse energy E; (ii) estimate the Gaussian spot w_0 and (iii) derive the fluence threshold ϕ_{th}. Based on this relation, a linear fit between r_{th}^2 and $ln(E)$ can be carried out as follow:

$$r_{th}^2 = b\, ln(E) + a \tag{3.2}$$

where the slope b and the intercept a determine the spot w_0 and the energy threshold E_{th}, according to Eq.(3.3).

$$w_0 = \sqrt{2b} \quad \text{and} \quad E_{th} = e^{-\frac{a}{b}} \tag{3.3}$$

Once w_0 and E_{th} are known the fluence threshold can be find by using Eq.(1.5) here reported:

$$\phi_{th} = \frac{2E_{th}}{\pi w_0^2} \tag{3.4}$$

$$\sigma_{\phi_{th}} = \sqrt{\left(\frac{\partial \phi_{th}}{\partial a}\right)^2 \Delta a^2 + \left(\frac{\partial \phi_{th}}{\partial b}\right)^2 \Delta b^2 + 2\left(\frac{\partial \phi_{th}}{\partial a}\right)\left(\frac{\partial \phi_{th}}{\partial b}\right) cov(a,b)} \tag{3.5}$$

where $\sigma_{\phi_{th}}$ is the statistical error of ϕ_{th}. This procedure is suitable for craters with a circular shape, i.e those obtained by focusing the laser beam with the spherical lens. As regards the elliptical spots, generated with the cylindrical lens, the method proposed in Sect.(3.2) was used.
The experimental conditions used to process the copper surface by focusing the laser beam with the spherical lens are summarized in Table (3.1).

Table 3.1: Experimental conditions for the fs laser structuring of a copper target, in the case of the spherical lens.

Number of pulses	Wavelenght (nm)	Rep. Rate (kHz)	Pulse energy (μJ)
200	1030	$(3 \div 30)$	$(30 \div 60)$

Figures (3.1) and (3.4) show OM images of the craters generated under the specified conditions.
From a qualitative point of view, the size of the laser spot on the sample enlarges with the increasing of the pulse energy [Fig.(3.1)], meanwhile the variation of repetition rates seems to not influence the relief structures [Fig.(3.4)].
In the OM images it is possible to recognize two different regions: (i) a inner circular crater and (ii) a circular ring that surrounds it.
The inner crater is characterized by a peculiar texture and, considering the Gaussian spatial intensity profile along the sample surface, it is found in correspondence with high values of fluence.

The outer annulus features ripples whose depth is linked to the pulse energy, indeed the panel [a] of Fig.(3.1) reports a crater elaborated at $E = 60\ \mu J$ and it displays sharp colors, i.e deeper ripples, whereas the panel [d] of Fig.(3.1) illustrates a circular structure generated at $E = 30\ \mu J$ with mild colors, corresponding to shallow ripples.
Moreover, the OM micrographs indicate ripples assembled in the zone corresponding to the Gaussian tail, i.e where the fluence is low.
Apart from the two distinct regions, every crater is surrounded by an annulus of faded colors. This zone represents the portion of area where nanoparticles deposit. The expansion of nanoparticles debris along the sample surface is analysed and discussed in Sect.(4.2).

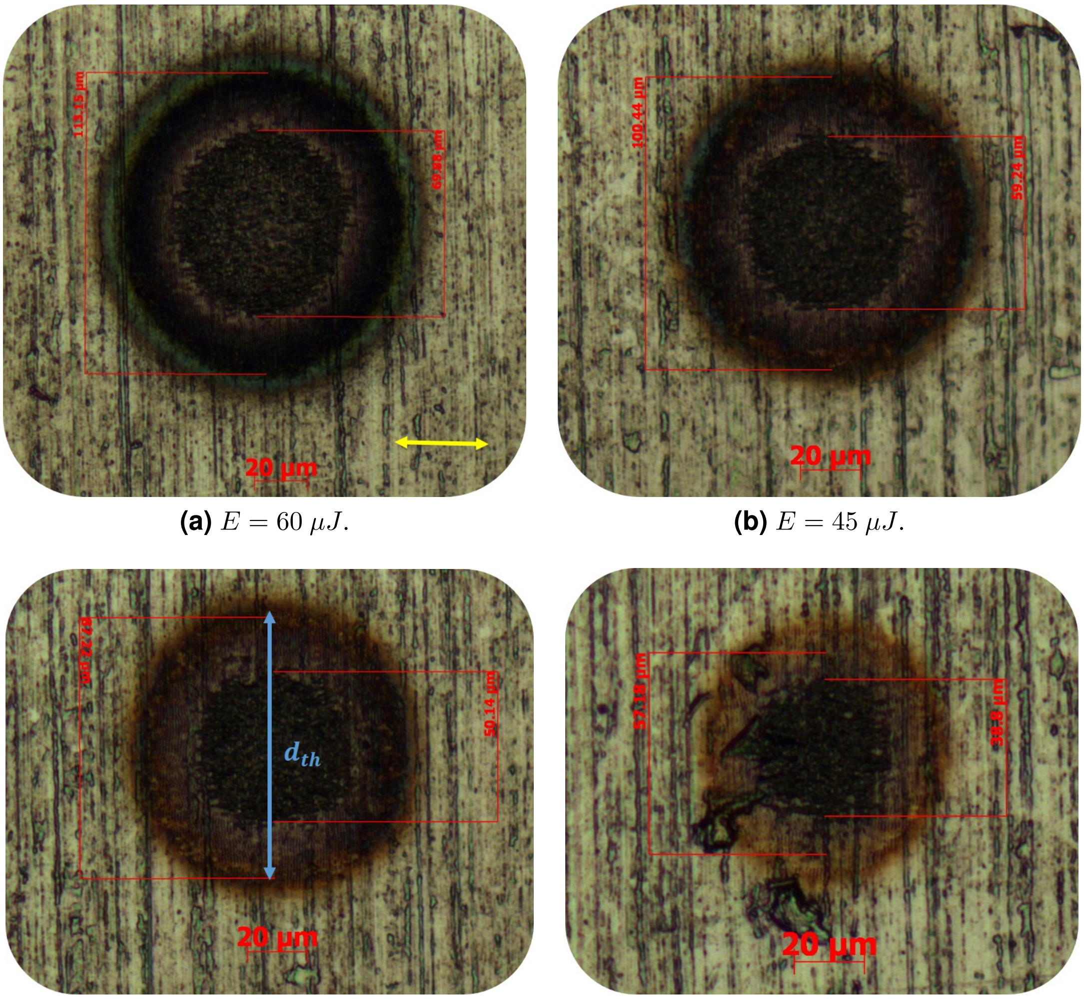

(a) $E = 60\,\mu J$. **(b)** $E = 45\,\mu J$.

(c) $E = 40\,\mu J$. **(d)** $E = 30\,\mu J$.

Figure 3.1: OM images of craters generated on a copper sample by focusing a train of pulses with the spherical lens ($f \sim 200\,mm$) at $\lambda = 1030\,nm$, $RR = 30\,kHz$, $N = 200$ and at variable energy E. The yellow arrow in the left panel on the top shows the direction of the laser beam polarization, while the blue arrow in the left panel on the bottom shows the measurement procedure.

The diameter d_{th} of the outer crater was measured as function of energy at fixed repetition rate. The measure was elaborated by using Image J software. A sketch of the experimental procedure is shown in the panel [c] of Fig.(3.1).
The square radius r_{th}^2 of the ablated region is derived from d_{th} and according to Eq.(3.1) its trend as function of $ln(E)$ is traced [Fig. (3.2)].
The plot in Fig.(3.2) proves the linear dependence of r_{th}^2 on $ln(E)$ as expected from the theory.

The linear fit in Eq.(3.2) and the mathematical relationships in Eq.(3.3) give the following estimates at $RR = 20\ kHz$: $E_{th} = (21\ \pm\ 1)\ \mu J$ and $w_0 = (78\ \pm\ 2)\ \mu m$. The corresponding fluence threshold for ablation is $\phi_{th} = (0.22\ \pm\ 0.04)\ J/cm^2$.

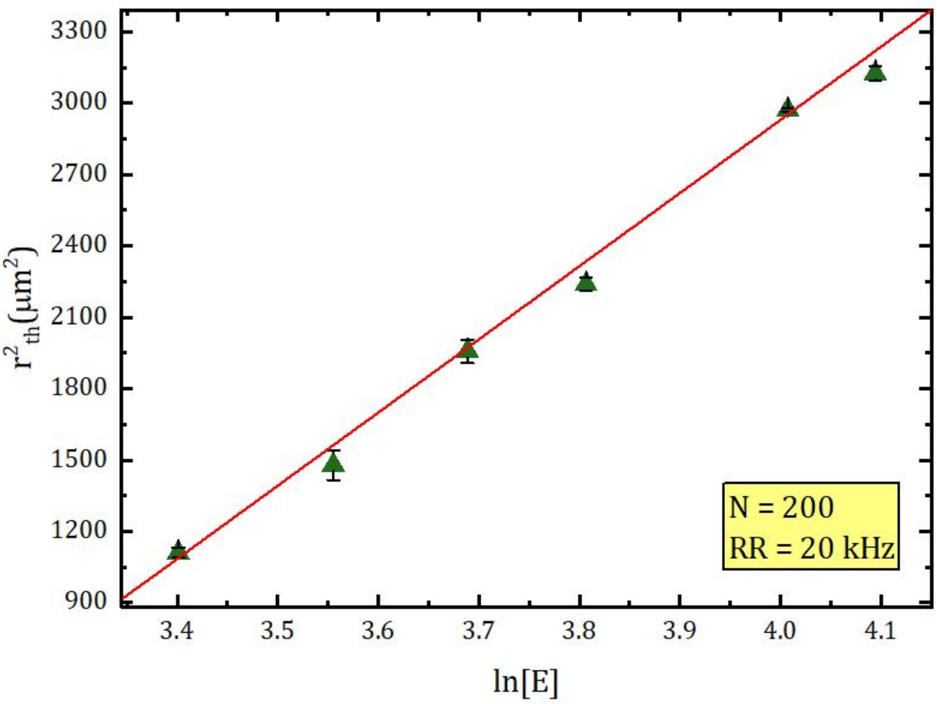

Figure 3.2: Variation of the square radius of the outer crater r^2_{th} as function of the natural logarithm of the pulse energy E at $RR = 20\ kHz$ and $N = 200$. The red line represents the result of the linear fit.

As the data at $RR = 20\ kHz$ are well described by the linear dependence of Eq.(3.1), so are the data at the other repetition rates ranging from 3 kHz up to 30 kHz. For the sake of simplicity, Fig.(3.3) reports the dependence of r^2_{th} on $ln(E)$ for each repetition rate, including the one at 20 kHz. The data in Fig.(3.3) show that the experimental points overlap each other and tend to align along a common line.
This result suggests to run a weighted average of r^2_{th} at fixed energy and study its linear dependence as function of $ln(E)$. The Table (3.2) displays the results achieved from this analysis which are compared with those obtained at $RR = 20\ kHz$ and recalled in Table (3.3).
The data listed below are in good agreement each other, this demonstrates that the relief structures are not influenced by varying RR, as we will discuss in the following.

We turn now to the discussion about the estimated values of ϕ_{th}. As aforementioned in Chap.(1), the fluence threshold depends on the material, i.e on both its thermal and optical characteristics, and on the specific experimental conditions.

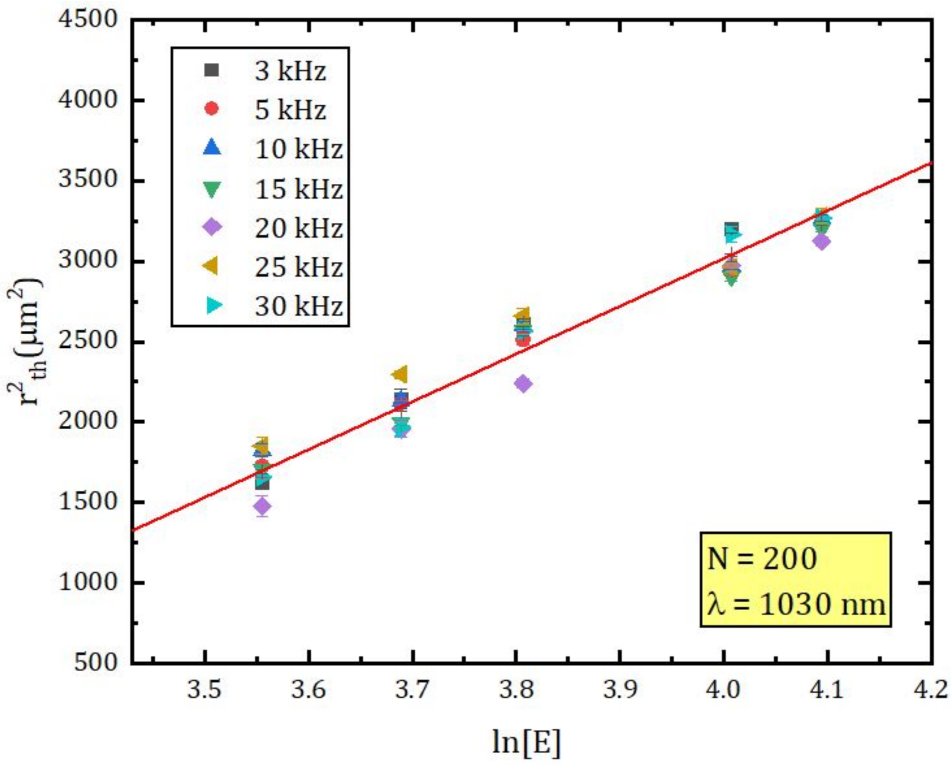

Figure 3.3: Variation of square radius of the outer crater r^2_{th} as function of the natural logarithm of the pulse energy E at each RR in the range of $(3 \div 30)\ kHz$. The line shows the linear trend obtained by the fitting procedure.

Table 3.2: Values of E_{th}, w_0 and ϕ_{th} resulting from the linear fit of the weighted average of r^2_{th} vs. $ln(E)$.

$E_{th}(\mu J)$	$w_0(\mu m)$	$\phi_{th}(J/cm^2)$
20 ± 1	77 ± 2	0.21 ± 0.04

Table 3.3: Values of E_{th}, w_0 and ϕ_{th} recalled from the analysis at $RR = 20\ kHz$.

$E_{th}(\mu J)$	$w_0(\mu m)$	$\phi_{th}(J/cm^2)$
21 ± 1	78 ± 2	0.22 ± 0.04

In the present case the value $\phi_{th} = (0.21 \pm 0.04)\ J/cm^2$ is in good agreement with those reported in the literature [2]. In particular, Ref.[59] reports a study at various fluence regimes performed with a fs laser source which provides a central wavelength of $800\ nm$ and operates at $RR = 20\ Hz$. The research shows that the copper fluence threshold is $\sim 0.2\ J/cm^2$ at low fluences. This value is consistent with ours, and although our experimental conditions are different from those listed above, we can stand that by irradiating the copper surface with an IR radiation and in the low fluence regime, the value of the threshold fluence for ablation is about $0.2\ J/cm^2$.

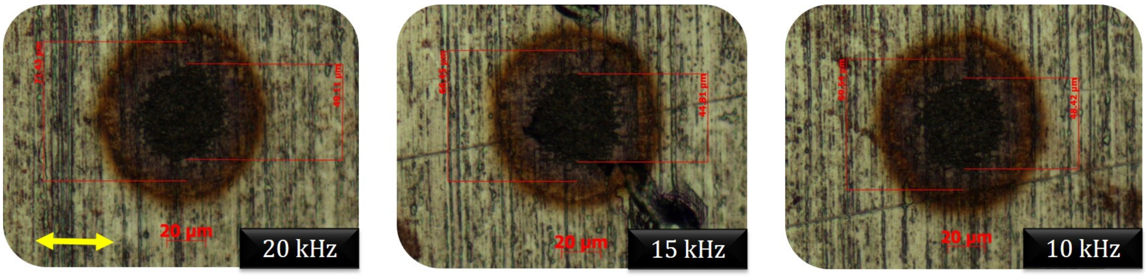

(a) Circular spots produced at $E = 30\ \mu J$.

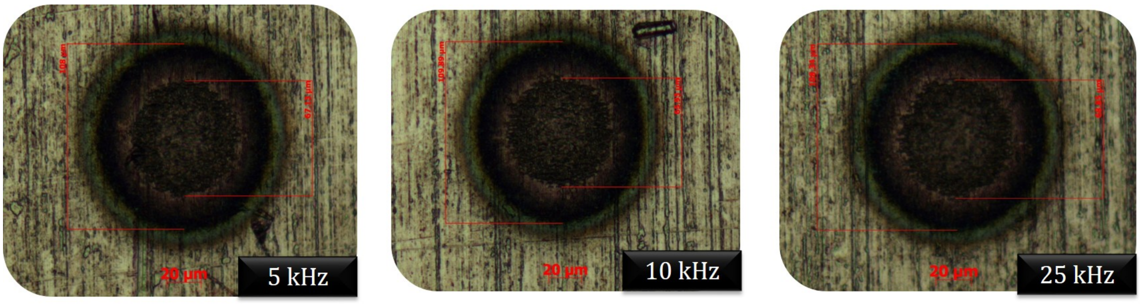

(b) Circular spots produced at $E = 55\ \mu J$.

Figure 3.4: OM images of craters generated on a copper sample by focusing a train of pulses with the spherical lens ($f \sim 200\ mm$) at $\lambda = 1030\ nm$, $N = 200$ and at variable repetition rate RR. The yellow arrow in the left panel on the top shows the direction of the laser beam polarization.

We now turn our attention to the investigation at various repetition rates. The quantitative analysis we carried out, as well as the plot illustrated in Fig.(3.3), lead to the conclusion that the various repetition rates do not induce substantial changes to the relief structures. From this point of view it can be stated that, in our experimental conditions the copper surface does not get involved in any effect of *heat accumulation* and *plume shielding*. The mentioned phenomena are common for experiments carried out at high repetition rate, i.e from kHz up to several MHz.

Heat accumulation occurs because of the short temporal separation between two consecutive laser pulses. As discussed in Sect.(1.1), when a train of pulses hit the material surface part of the energy is absorbed by the target and diffuses beneath its surface. However, if the rate of the delivered pulses is too high, some of the energy remains trapped onto the surface, causing it to reach high temperatures. Such an effect causes the surrounding regions of the irradiated area to be heated, melted and damaged. These effects produce irreversible changes of the surface [1].

The plume shielding effect takes place when the plume, resulting from the removal of the material during the ablation process, stands above the target on a timescale comparable with the pulse separation. Under this condition, the interaction between the cloud of electrons, atoms, nanoparticles and the incoming pulse occurs. As a consequence, the effective energy released to the sample is reduced, leading the crater to change its features [1].

In this framework these effects do not appear under the specified experimental conditions. To explain the reason for which the nanostructered surface of copper does not change with the increase of the RR, we mostly rely Ref.[49]. This paper contains interesting results on the dynamics of the removed material from the surface of several metals, including Cu. In this research the fs laser source ($\tau_p \sim 300\ fs$) operates at: $\lambda = 1030\ nm$, with repetition rates variation ranging from $31\ kHz$ up to $500\ kHz$ and in a fluence variation window of $(0.6 \div 18)\ J/cm^2$. The samples are irradiated in raster scan method. Although these experimental conditions are different from those we used, the gained results can be suitable for our case, since they were obtained in the same spectral range (IR) and they can reasonably be applied at lower fluences and repetition rates.

As regards copper, one of the most important achievements is that the ablation rate (i.e the volume of removed material per pulse) is proved to be dependent on laser fluence, but independent on repetition rate. In particular, at the fluence of $0.6\ J/cm^2$ the ablation rate is shown to be the lowest of all, and i.e little material is removed from the surface of the target. It can reasonably be assumed that at fluences $\phi \lesssim 0.6\ J/cm^2$ the portion of the ejected material is even smaller. The present work fits in this scenario since our laser system operated in the fluence variation window of $(0.3 \div 0.6)\ J/cm^2$ and at RR less than those used in Ref.[49].

Accordingly, the material released by the irradiated copper surface results in a cloud consisting of a small amount of clusters, ion and nanoparticles. A plasma plume composed in such a way is not dense enough to provoke the plume shielding effect, that is hence assumed avoided in our experimental conditions. This argument is sustained by the fact that the reflectance of copper in the IR spectral range reaches high values, almost close to one ($R \sim 0.97$ [46]). Therefore, without considering that pulse by pulse the optical properties of the material could change, at the wavelength of $\lambda = 1030\ nm$ copper reflects most of the radiation and absorbs the little remaining part, leading to a low ablation rate at low fluences (i.e it takes a lot of energy to excite copper in the IR spectral region).

As an example, effects of plume shielding are observed on silicon, irradiated with a fs laser source at $\lambda = 1030\ nm$ for $RR \geqslant 10\ kHz$ [1]. According to our explanation, this result should be reasonable since the reflectance of silicon in the IR spectral region is $R \sim 0.33$ [47] , i.e it is required little energy to excite silicon in IR spectral region.

Heat accumulation is more difficult to clarify, since there are few theoretical models aimed at explaining this effect for a given material. However, an indication of why this phenomenon does not occur on copper, in our experimental conditions, can be given by the material properties itself. For example, the heat penetration depth of copper is found to be greater with respect to Ti and stainless steel, for which high repetition rates have an impressive effect [49]. Moreover, due to its high thermal conductivity, the cooling rate of copper results faster than the one of Ti [49]. These considerations could carry to the conclusion that for copper the thermal energy is not getting strongly confined, but it is spread quickly. From this point of view, the thermal energy does not diffuse around the regions of the irradiated surface, thus limiting heat accumulation effects.

3.2 Measurements and results for elliptical craters

In the present section we extend the Gaussian beam model to the case of craters of elliptical shape obtained by focusing the laser beam with a plano-convex cylindrical lens.
As already discussed, the profile of the laser beam along the sample surface is Gaussian. Since an ellipse has different sizes along the x and y directions, we assume that the spatial intensity profile of the beam on the target will result in a two dimensional fluence distribution having different Gaussian widths $w_{0,x}$ and $w_{0.y}$ [(Eq.(3.6)]:

$$\phi(x,y) = \phi_0 e^{-\frac{2x^2}{w_{0,x}^2}} e^{-\frac{2y^2}{w_{0,y}^2}} \qquad \text{where} \qquad \phi_0 = \frac{2E}{\pi w_{0,x} w_{0,y}} = \frac{2E}{S} \tag{3.6}$$

In this frame, we separate the problem along the two directions x and y, in order to obtain two equations equivalent to the expression in Eq.(1.3), used for the circular spots. The two relations are shown in Eq.(3.7).

$$\phi(x) = \phi_{0,x}\, e^{-\frac{2x^2}{w_{0,x}^2}} \qquad \text{and} \qquad \phi(y) = \phi_{0,y}\, e^{-\frac{2y^2}{w_{0,y}^2}} \tag{3.7}$$

We carry on the discussion for the Gaussian along the x axis, taking into account that the same treatment can be applied for the Gaussian along y.
By indicating with x_{th} the minor axis of the elliptical spot, the Eq.(3.7) on the right became:

$$\phi(r_x) = \phi_{0,x}\, e^{-\frac{2r_x^2}{w_{0,x}^2}} = \frac{2E}{\pi w_{0,x}^2}\, e^{-\frac{2r_x^2}{w_{0,x}^2}} = \phi_{th,x} = \frac{2E_{th,x}}{\pi w_{0,x}^2} \tag{3.8}$$

where for the sake of simplicity we put $r_x = r_{x_{th}} = \dfrac{x_{th}}{2}$.

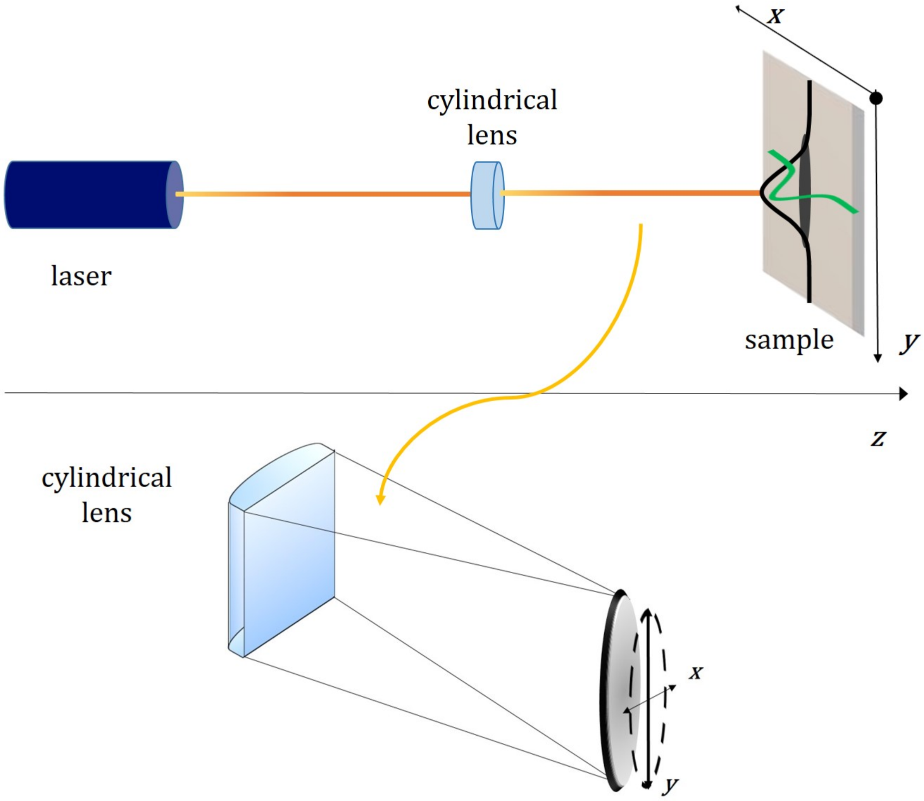

Figure 3.5: Representation of the Gaussian profile along the sample surface when the beam is focused with the cylindrical lens.

From the Eq.(3.8), the formula in Eq.(3.9) is derived and as well as done for the circular craters, it can be exploited for the linear fit below reported.

$$r_x^2 = \frac{w_{0,x}^2}{2} ln\left(\frac{E}{E_{th,x}}\right) \longrightarrow r_x^2 = b\ ln(E) + a \tag{3.9}$$

The fitting parameters a and b are linked to E_{th} and w_0 in the same way reported in Eq.(3.3). Once the analysis is carried out both for x and y, the obtained values of $E_{th,i}$ and $w_{0,i}$, where i stands for x and y, are used to determine the total energy threshold E_{th}:

$$E_{th} = \frac{E_{th,x} + E_{th,y}}{2} \quad \text{with error} \quad \sigma_{E_{th}} = \frac{\sqrt{\sigma_{E_{th,x}}^2 + \sigma_{E_{th,y}}^2}}{2} \tag{3.10}$$

the total spot S:

$$S = \pi w_{0,x} w_{0,y} \quad \text{with error} \quad \sigma_S = \sqrt{\left(\frac{\partial S}{\partial w_{0,x}}\right)^2 \sigma^2_{w_{0,x}} + \left(\frac{\partial S}{\partial w_{0,y}}\right)^2 \sigma^2_{w_{0,y}}} \tag{3.11}$$

and thus the fluence threshold ϕ_{th}:

$$\phi_{th} = \frac{2E}{S} \quad \text{with error} \quad \sigma_{\phi_{th}} = \sqrt{\left(\frac{\partial \phi_{th}}{\partial E_{th}}\right)^2 \sigma^2_{E_{th}} + \left(\frac{\partial \phi_{th}}{\partial S}\right)^2 \sigma^2_S} \tag{3.12}$$

As anticipated in Chap.(2), the elliptical craters were produced by irradiating the surface of copper samples with a fs laser source which provides the fundamental output at $1030\ nm$ and its second harmonic at $515\ nm$. For the sake of simplicity we summarizes the experimental conditions in Table (3.4) .

Table 3.4: Experimental conditions for the copper surface nanostructured at $\lambda = 1030\ nm$ and $\lambda = 515\ nm$.

Wavelength(nm)	Number of pulses	Repetition Rate(kHz)	Pulse energy(μJ)
1030	200	5	$(356 \div 506)$
515	200	5	$(94 \div 197)$

It should be noted in the case where the laser beam is focused with a cylindrical lens, the energy of the pulses is one order of magnitude higher than the case where the beam is focused with the spherical lens. This fact can be explained as follow: when a beam is focused in a line on a target, the laser fluence along it is lower than when the same beam is focused at a point with a spherical lens. As a result in order to remove enough material to ensure ablation, the energy per pulse is required to be greater when the beam is focused through the cylindrical lens [70].

We turn now to the analysis of the surface structures generated on Cu at $\lambda = 1030\ nm$. The Figure (3.6) displays the variation of the crater sizes along y direction as function of the energy E. In particular the panel on the right illustrates craters obtained at low energy values, whereas the left panel shows structures elaborated at higher energy values. The size of the elliptical spot increases as function of the energy as well as its depth.
Figure (3.7) reports two OM images exemplifying the central area of the sample elaborated at the pulse energy of $E = 506\ \mu J$ and $E = 392\ \mu J$ where it can be clearly seen that the crater width is greater in the case of the highest energy.
Moreover, Figs.(3.6) and (3.7) evidence inner and outer structures. This means that,

as observed for the circular craters, there are two fluence regimes at which different structures are formed, in particular the outer zone features ripples that form in correspondence of the Gaussian beam wings and whose characterization has been carried out in Sect.(4.1).

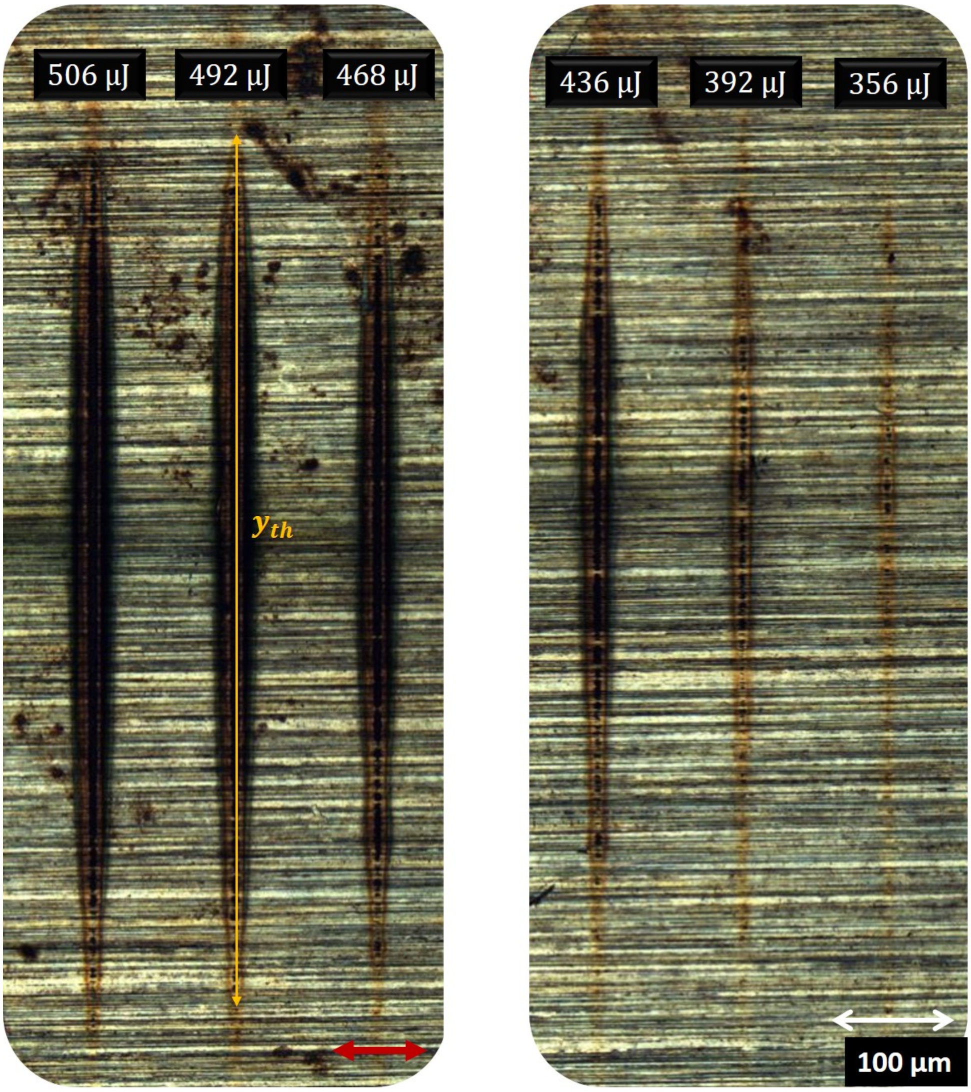

Figure 3.6: OM images of craters generated on Cu at $1030\ nm$. The red arrow in the left panel represents the laser beam polarization, while the long yellow arrow indicates how the major axis of the elliptical craters was measured. Each panel displays the pulse energy at which the relief structure was engendered.

We measured the major y_{th} and the minor x_{th} axes of the elliptical craters by using Image J software. A sketch of the experimental procedure is indicated in the left panel

of Fig.(3.6) and in the panel [b] of Fig.(3.7).
From the measured data, the radii r_x and r_y are derived. Figure (3.8) displays the trend of r_x^2 and r_y^2 as function of $ln(E)$ according to Eq.(3.9). The illustrated plots confirm the linear dependence of r_x^2 and r_y^2 on $ln(E)$. From the linear fit in Eq.(3.8) the values of $E_{th,i}$ and $w_{0,i}$ (with $i = x,\ y$) are obtained and shown in Tab.(3.5). From the data listed below, exploiting the Equations [(3.10)-(3.12)] we estimate the total energy threshold E_{th}, spot S and fluence ϕ_{th}.

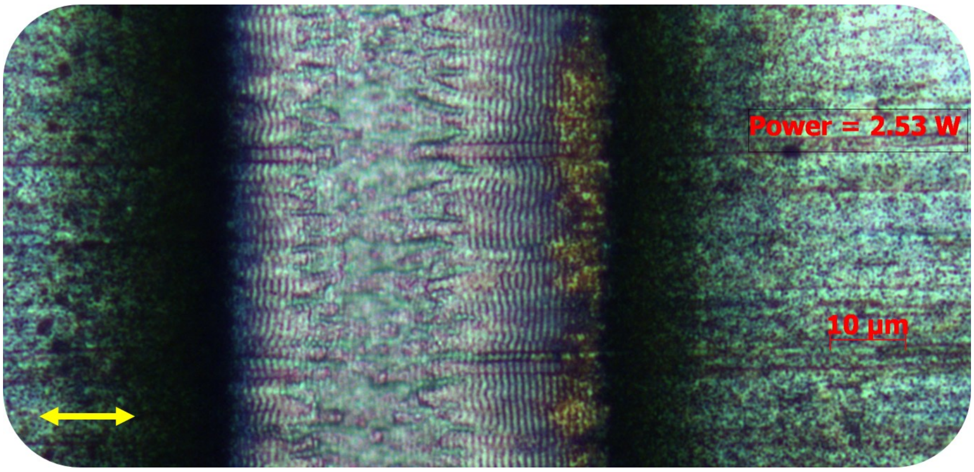

(a) Elliptical spot produced at $E = 506\ \mu J$.

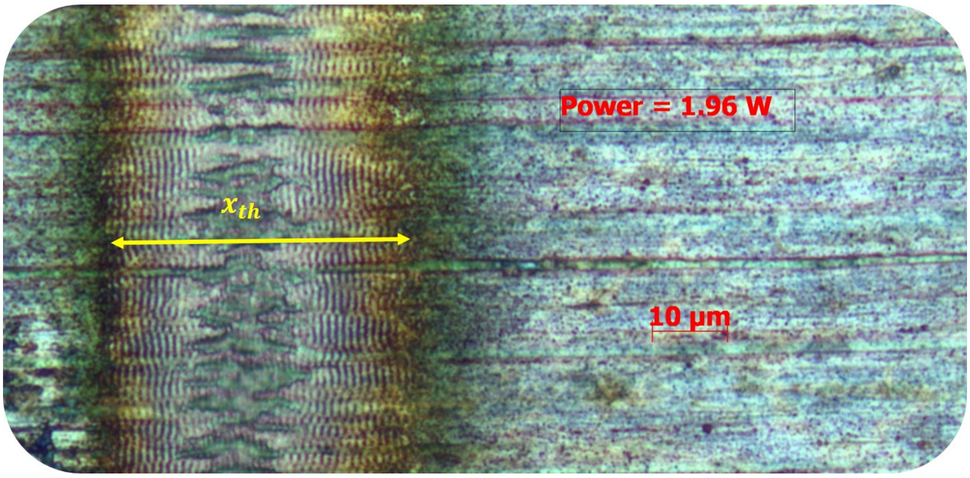

(b) Elliptical spot produced at energy $E = 392\ \mu J$.

Figure 3.7: OM images of the central part of craters generated on Cu at $\lambda = 1030\ nm$ with the cylindrical lens ($f\ \sim 150\ mm$). The yellow arrow in the upper panel shows the direction of the laser beam polarization, while the yellow arrow on the bottom indicates how the minor axis of the elliptical crater has been measured.

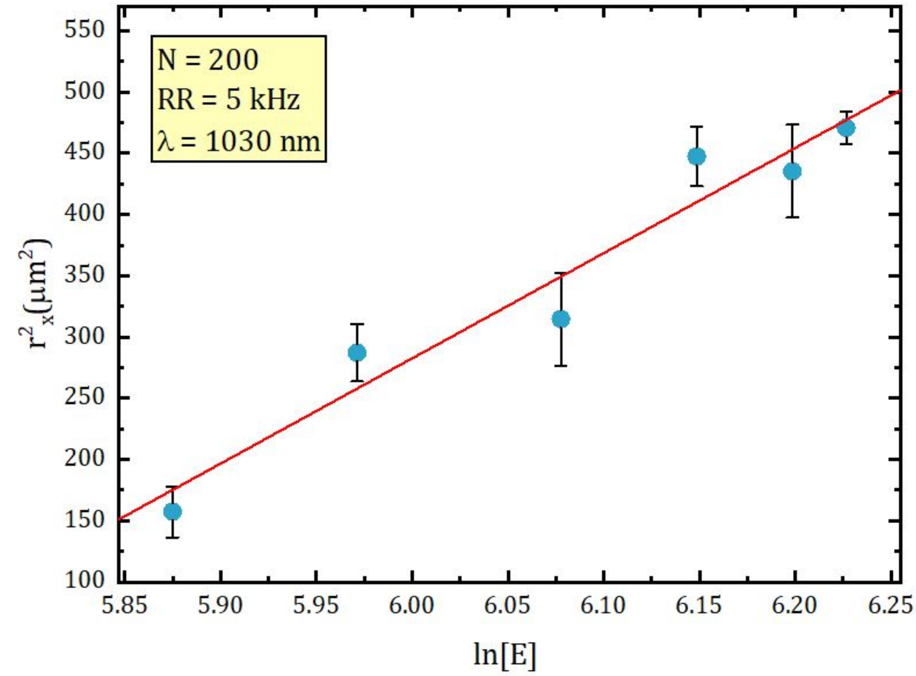

(a) r_x^2 vs $ln(E)$.

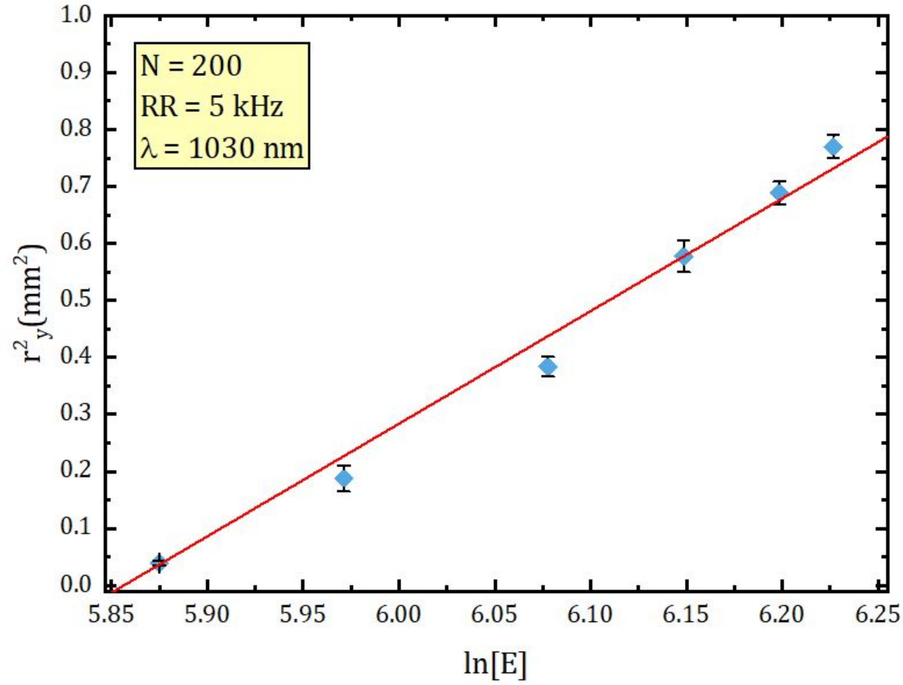

(b) r_y^2 vs. $ln(E)$.

Figure 3.8: Variation of the minor and major squared radii r_x^2 and r_y^2 of the outer crater as a function of the natural logarithm of E in the range $(356 \div 506)$ μJ.

Table 3.5: Values of $E_{th,i}$ and $w_{0,i}$ resulting from the linear fits r_i^2 vs. $ln(E)$, with $i = x,\ y$. The values refer to the analysis carried out on the copper surface structured at $\lambda = 1030\ nm$.

Direction	Threshold energy E_{th}	Gaussian spot w_0
x	$(291\ \pm\ 15)\ \mu J$	$(42\ \pm\ 3)\ \mu m$
y	$(355\ \pm\ 5)\ \mu J$	$(2.1\ \pm\ 0.1)\ mm$

Table (3.6) displays these results which are compared with those obtained from the analysis on the circular spots and recalled in Tab.(3.7). The values of the fluence thresholds are in good agreement each other. Such an achievement confirms what we know from the theory, i.e the threshold fluence depends on both optical and thermal characteristics of the material [2] and on the specific experimental conditions: the laser wavelength λ, the fluence regime and the number of pulses N [13]. Since both the experimental conditions and the target were the same, it is reasonably to aspect the same ϕ_{th}. The only difference between the two arrangements was the employment of different lenses that cause the E_{th} to be different. In fact, as already explained, in the case of the cylindrical lens the energy of pulses necessary to remove sufficient material must be higher with respect to the case of the spherical lens.

Table 3.6: Values of E_{th}, S and ϕ_{th} resulting from the analysis of the elliptical spots on Cu surface elaborated at $\lambda = 1030\ nm$.

$E_{th}(\mu J)$	$S(mm^2)$	$\phi_{th}(J/cm^2)$
$323\ \pm\ 8$	$0.27\ \pm\ 0.02$	$0.24\ \pm\ 0.02$

Table 3.7: Values of E_{th}, S and ϕ_{th} resulting from the analysis of circular spots generated on Cu surface produced at $\lambda = 1030\ nm$.

$E_{th}(\mu J)$	$S(mm^2)$	$\phi_{th}(J/cm^2)$
$20\ \pm\ 1$	$0.018\ \pm\ 0.001$	$0.21\ \pm\ 0.04$

Note that the value of S in Tab.(3.7) is calculated from w_0 displayed in Tab.(3.6), by using $S = \pi w_0^2$.
Moreover, the consistence between the results prove that the conventional procedure for threshold measurements, which assumes a Gaussian laser beam focused with a spherical lens, is also suitable for a Gaussian laser beam focused with a cylindrical lens.

The same measurement procedure and analysis, above developed, has been carried out on the OM and SEM images relative to the Cu surface structured at $\lambda = 515\ nm$. The panels of Fig.(3.9) show the formation of lines longer and tighter with respect to those illustrated in Fig.(3.6).
Figure (3.10) reports the central area of the irradiated samples, in particular the panel on the left displays a crater generated at $E = 170\ \mu J$ and the panel on the right illustrates

a crater produced at $E = 125\ \mu J$. In both cases the images evidence an outer and an inner zone which are not visible in Fig.(3.9) due to the low spatial resolution of the OM image. The dark region surrounding the crater represents the deposition of nanoparticles whose dispersion will be further investigated in Sect.(4.2).

Figure 3.9: OM images of craters generated on copper at $\lambda = 515\ nm$ with the cylindrical lens. The white arrow in the central panel represents the laser beam polarization. Moreover each panel displays the pulse energy at which the elliptical craters were produced.

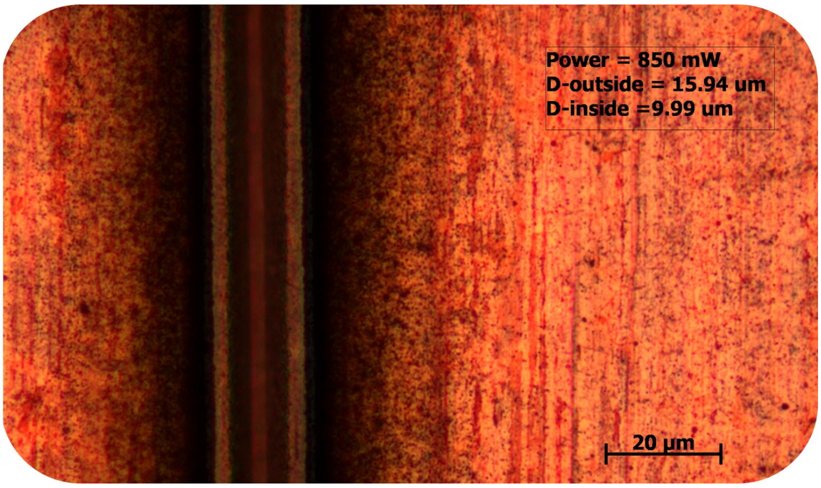

(a) Elliptical spot generated at the pulse energy of $E = 170\ \mu J$.

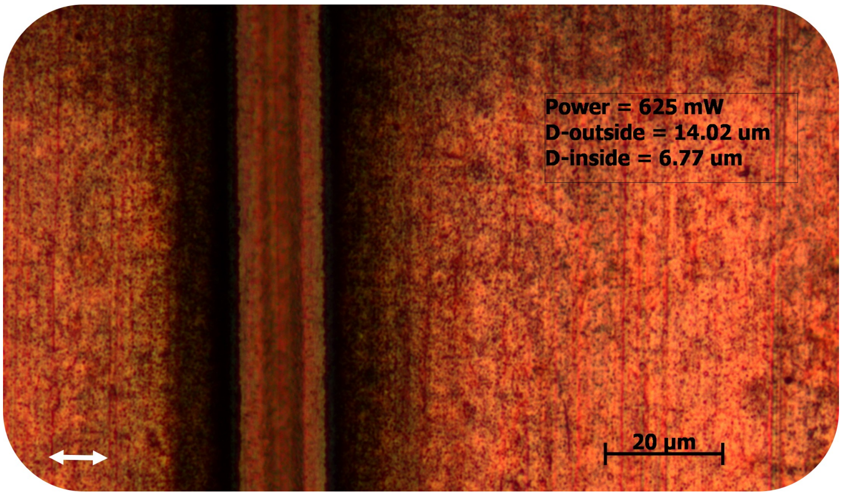

(b) Elliptical spot generated at the pulse energy of $E = 125\ \mu J$.

Figure 3.10: OM images of the central part of craters produced on the Cu target by focusing the laser beam with the cylindrical lens ($f \sim 150\ mm$) at $\lambda = 515\ nm$. The white arrow in the lower panel indicates the direction of the laser beam polarization.

From the OM images above described, the major and minor axes of the elliptical craters were measured and used to derive the dependence of r_x^2 and r_y^2 on $ln(E)$ reported in Fig.(3.11). The plot proves that the crater size increases lineary as function of $ln(E)$. The radius along r_y is found to be $2.1\ mm$ at the higher energy and $1.6\ mm$ at the lower energy. The minor radius r_x varies from $8\ \mu m$ up to $6.3\ \mu m$. Table (3.8) reports the values obtained from the linear fit of Eq.(3.8).

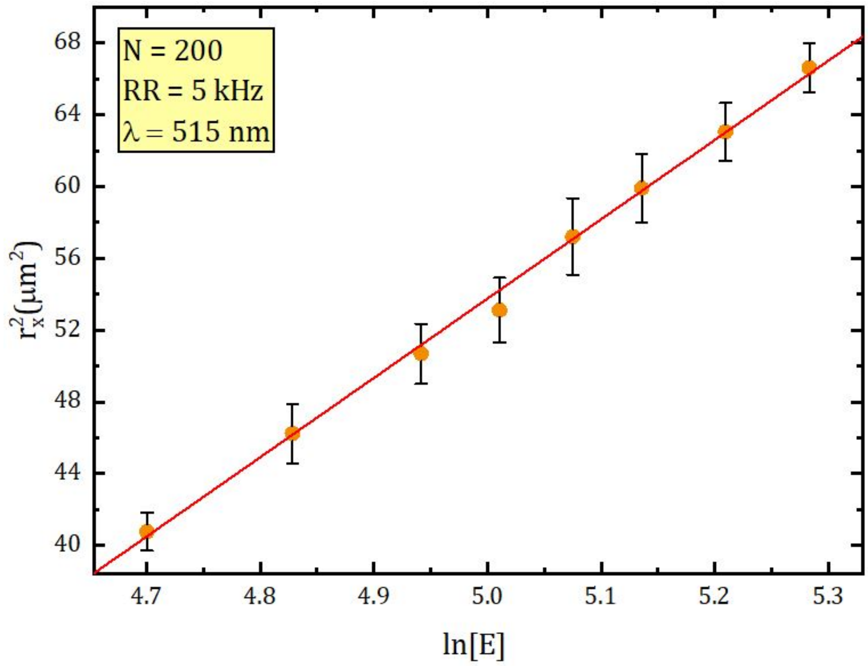

(a) r_x^2 vs. $ln(E)$.

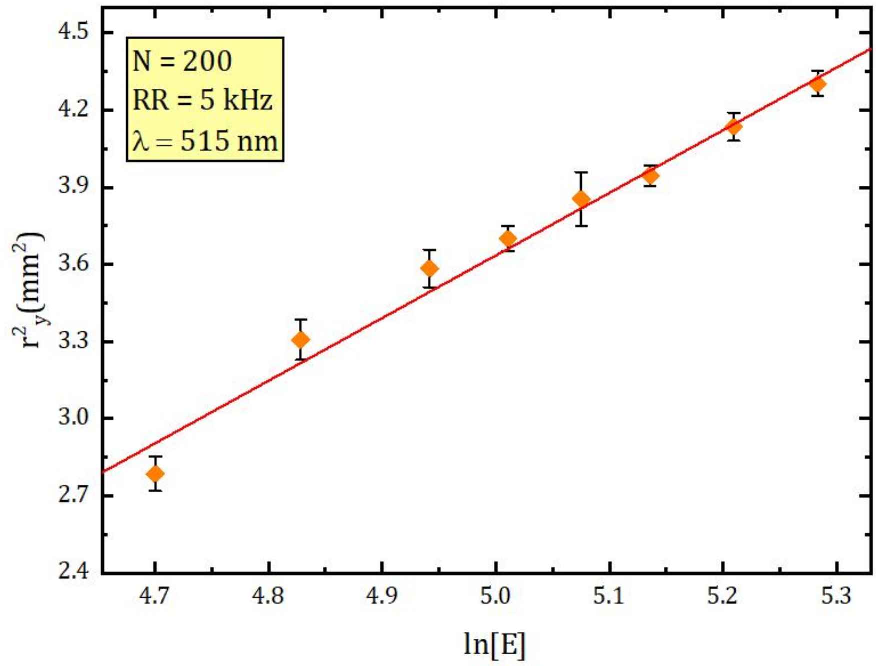

(b) r_y^2 vs. $ln(E)$.

Figure 3.11: Variation of the minor and major squared radii r_x^2 and r_y^2 as function of the natural logarithm of E in the range $(110 \div 197)$ μJ. These trends are related to measurements performed on OM images.

Table 3.8: Values of $E_{th,i}$ and $w_{0,i}$ resulting from the linear fits r_i^2 vs. $ln(E)$, where $i = x, y$. The values refers to the analysis carried out on the OM images that illustrate the copper surface structured at $\lambda = 515\ nm$.

Direction	Threshold energy E_{th}	Gaussian spot w_0
x	$(45\ \pm\ 2)\ \mu J$	$(9.4\ \pm\ 0.1)\ \mu m$
y	$(34\ \pm\ 4)\ \mu J$	$(2.2\ \pm\ 0.1)\ mm$

The SEM image in Fig.(3.12) illustrates a complete visualization of the elliptical spots produced on Cu at $\lambda = 515\ nm$. Although the image is acquired at high resolution, it is not capable to display the inner and the outer zone. Such a distinction can be clearly observed in the panels of Fig.(3.13). Both of SEM micrographs evidence ripples in the external region of the irradiated surface and a peculiar textures in the internal zone.

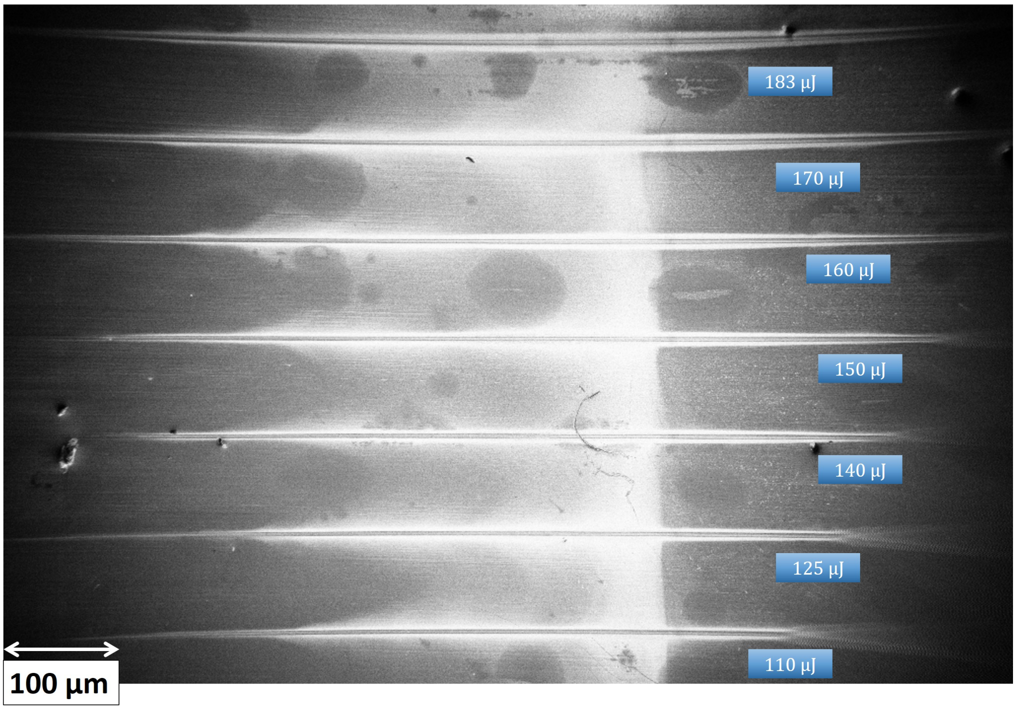

Figure 3.12: SEM image of the elliptical spots on Cu at $\lambda = 515\ nm$ obtained with an In-Lens (IL) detector. We signed up the energy at which each line was produced.

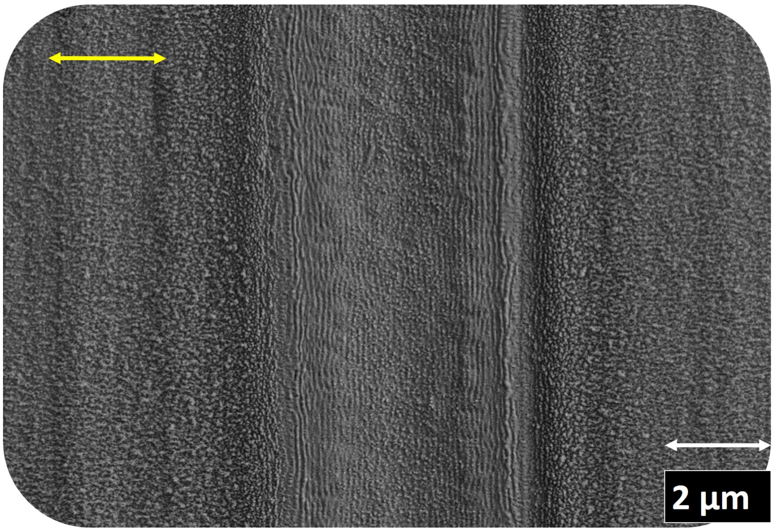

(a) Elliptical spot produced at an energy $E = 94\ \mu J$.

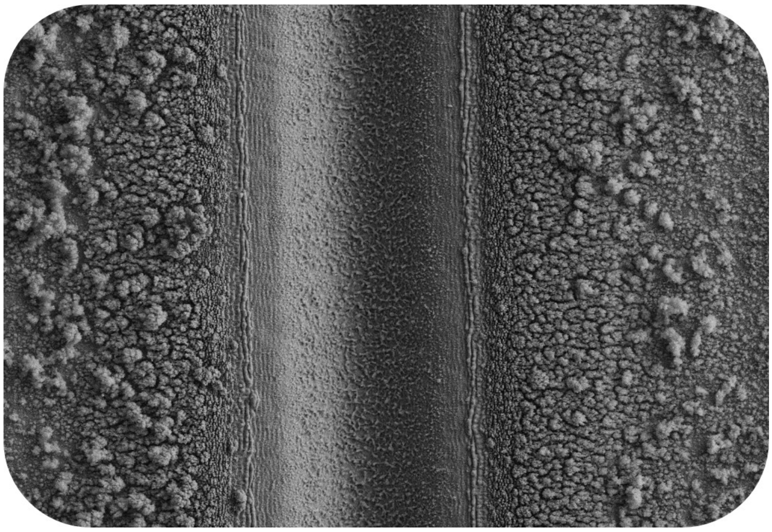

(b) Elliptical spot produced at an energy $E = 197\ \mu J$.

Figure 3.13: SEM images of the central part of craters generated on the Cu target at $\lambda = 515\ nm$ with the cylindrical lens $(f\ \sim 150\ mm)$. The yellow arrow in the top panel displays the direction of the lase beam polarization.

The upper panel reports a crater generated at $E = 94\ \mu J$, whereas the panel on the bottom illustrates the relief structure elaborated at $E = 197\ \mu J$. As it can be observed, the removal of material is more consistent in the case of high energy since the crater is shown to be deeper and surrounded by a greater amount of nanoparticles. The variation of r_x^2 and r_y^2 as function of $ln(E)$ is illustrated in Fig.(3.14) and the results of the linear fit are provided in Tab.(3.9).

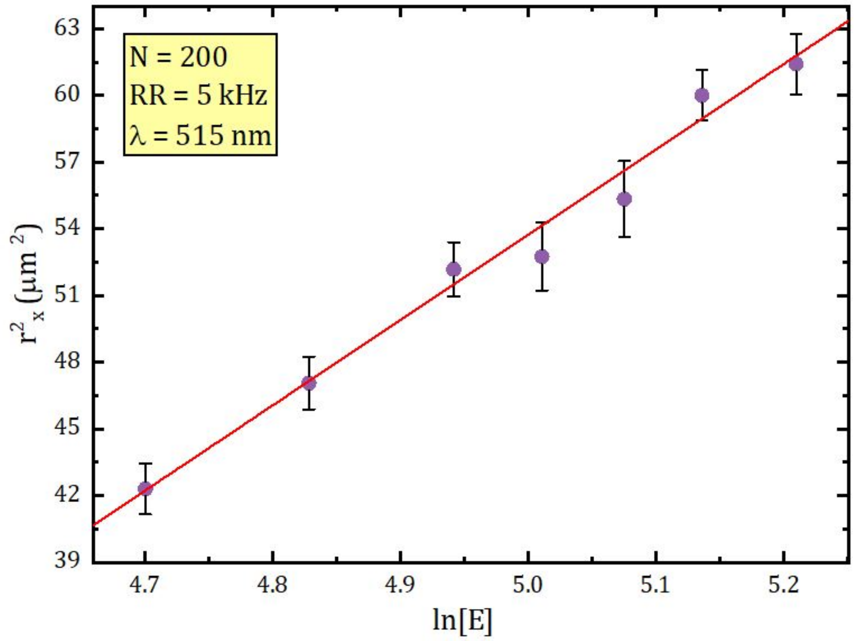

(a) r_x^2 vs. $ln(E)$.

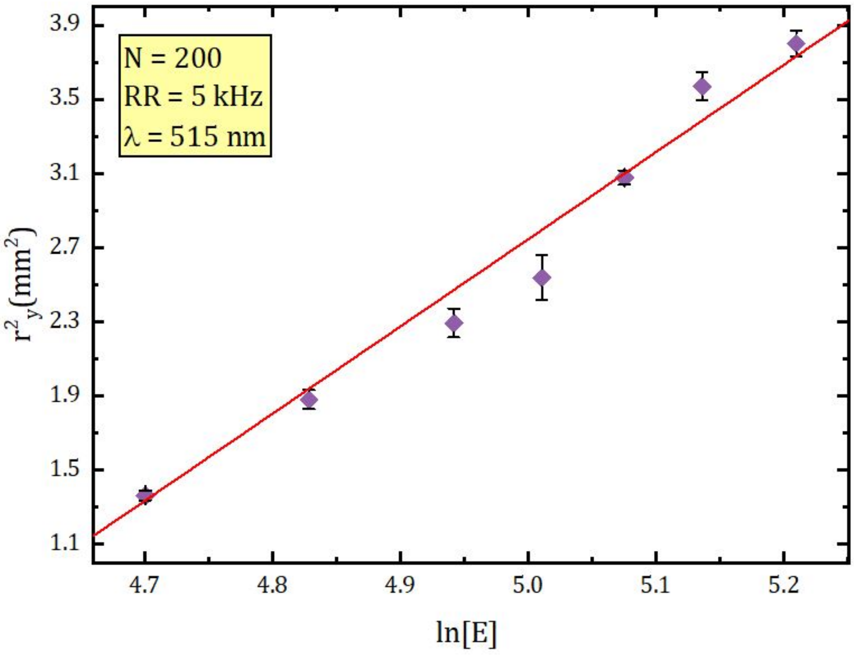

(b) r_y^2 vs. $ln(E)$.

Figure 3.14: Variation of minor and major squared radii r_x^2 and r_y^2 of the crater as function of the natural logarithm of E in the range $(110 \div 183)\ \mu J$. These trends refer to measurements carried out on SEM images exemplifying the copper surface texture generated by irradiation sequences at $\lambda = 515\ nm$.

Table 3.9: Values of $E_{th,i}$ and $w_{0,i}$ resulting from the linear fits r_i^2 vs. $ln(E)$, where $i = x, y$. The values refers to the analysis carried out on the SEM images that displays the copper surface structured at $\lambda = 515\ nm$.

Direction	Threshold energy E_{th}	Gaussian spot w_0
x	$(36\ \pm\ 3)\ \mu J$	$(8.7\ \pm\ 0.3)\ \mu m$
y	$(86\ \pm\ 4)\ \mu J$	$(3.1\ \pm\ 0.1)\ mm$

From the data listed above and in Tab.(3.8) the total fluence and energy thresholds for copper ablation, as well as the spot S, are derived. The results are summarized in Tab.(3.10) where, in order to have a complete visualization of the achievements, we recall the values resulting from the analysis of the OM images at $\lambda = 1030\ nm$.

Table 3.10: Values of E_{th}, S and ϕ_{th} resulting from the analysis of the OM and SEM images exemplifying the elliptical spots elaborated on the copper target.

Wavelenght(nm)	Image	$E_{th}(\mu J)$	$S(mm^2)$	$\phi_{th}(J/cm^2)$
1030	OM	$323\ \pm\ 8$	$0.27\ \pm\ 0.02$	$0.24\ \pm\ 0.02$
515	OM	$61\ \pm\ 3$	$0.07\ \pm\ 0.02$	$0.12\ \pm\ 0.04$
515	SEM	$70\ \pm\ 2$	$0.08\ \pm\ 0.02$	$0.14\ \pm\ 0.04$

The fluence and energy thresholds estimated from the analysis of OM a SEM images representing the copper surface structured at $\lambda = 515\ nm$, are in pretty good agreement with each other, within the errors.
Registered values of ϕ_{th} are not matched to the scientific literature since the green wavelength regime has been rarely discussed. A value reported in literature is $0.54\ J/cm^2$, but it is related to an experiment performed with a single laser shot [26]. However, such a difference suggests, or rather confirms, that feedback mechanisms involved at high number of pulses influence the fluence threshold for ablation. Indeed, from an experimental point of view the multiple pulse ablation threshold $\phi_{th}(N)$, where N is the number of incident pulses, follows the formula [23]:

$$\phi_{th}(N) = \phi_{th}(1)N^{\xi-1} \tag{3.13}$$

where $\phi_{th}(1)$ is the fluence threshold at single shot and ξ is the *incubation coefficient* that depends on the specific material. In literature the estimated value of ξ for copper is around (0.76 ± 0.02) [13], [23].
In our case, the coefficient ξ can be calculated by using Eq.(3.13). The same type of analysis can be run not only at $\lambda = 515\ nm$, but also at $\lambda = 1030\ nm$ for which the single shot ablation threshold was determined to be $(1.06 \pm 0.12)J/cm^2$ [13]. Table

(3.11) summarizes the values of ξ attained from this analysis and the fluence thresholds used to calculate it. Note that $\phi_{th} = 0.13\ J/cm^2$ is obtained from the average between the data at $\lambda = 515\ nm$ listed in Tab.(3.10).

Table 3.11: Incubation coefficient ξ obtained in the cases where the copper surface is structured with a IR and VIS radiation.

Wavelenght(nm)	$\phi_{th}(1)(J/cm^2)$	$\phi_{th}(N)(J/cm^2)$	ξ
1030	1.06 ± 0.12 [13]	0.24 ± 0.02	0.72 ± 0.03
515	0.54 [26]	0.13 ± 0.04	0.73 ± 0.06

The estimated incubation coefficients are consistent, within the errors, both with each other and with the values reported in the literature. This analysis suggests that the fluence threshold for copper ablation, found in this thesis work, with a radiation at $515\ nm$, is consistent with what is already known about copper. Another aspect worthy of attention concerns the difference between the recorded values of ϕ_{th} at the two wavelengths. In particular, the fluence threshold is lower if the surface is irradiated with laser pulses at the visible wavelength. This may be due to the optical properties of copper. Indeed, at $\lambda = 515\ nm$ the reflectance coefficient of copper is $R \sim 0.59$ [45], whereas at $\lambda = 1030\ nm$ it is ~ 0.97 [46]. This means that in the visible range, the copper is prone to absorb much radiation with respect to IR. As a consequence, the energy per unit area required to damage the surface is smaller in the case where copper is nanostructured with a laser beam having a green wavelength. These results are in agreement with the literature. In fact, although there are few works on copper in the visible regime, some recent investigations were conducted on copper with fs laser sources at the wavelengths of $1030\ nm$ and $515\ nm$ [26], [69]. In particular, the authors suggest that in the case of the IR the two-photon absorption effect is involved , since the single-photon energy is not high enough to force the electrons optical transition.

Chapter 4

Morphology of craters and deposition of nanoparticles

The present chapter is devoted to the morphological characterization of the surface structures elaborated on copper. The description of the morphological features of the elliptical craters is provided in Sect.(4.1) with a particular attention on ripples. Sect.(4.2) focuses on the deposition of nanoparticles over the copper substrate.

4.1 Analysis of the ripples spatial period

In this section, we analyse in more detail the surface structures developed on copper by focusing the laser beam with the cylindrical lens. For the sake of simplicity, Tab.(4.1) recalls the experimental conditions used to process the copper surface.

Table 4.1: Experimental conditions employed in this thesis work to develop surface structures by using a cylindrical lens with a focal length of 150 mm.

λ (nm)	N	RR (kHz)	Pulse energy (μJ)	Peak Fluence (J/cm^2)
515	200	5	$(94 \div 197)$	$(0.24 \div 0.49)$
1030	200	5	$(356 \div 506)$	$(0.26 \div 0.37)$

The values of the peak fluence were calculated by using $\phi_0 = 2E/S$ where S is the total spot reported in Tab.(3.10) of Sect.(3.2).
As discussed in Sect.(3.2), the OM images display elliptical craters with inner and outer structures whose morphological features are not clearly visible, owing to the low spatial resolution of the pictures. Such an issue is overcame by using the scanning electron microscope that acquires clearer images at higher resolution. From this point of view,

the regions displayed in the OM micrographs can be associated to the morphological features appearing in the SEM images.

We start to consider the elliptical craters generated at the green wavelength. Fig.(4.1) reports OM and SEM images of a crater elaborated at a pulse energy of $E = 170\ \mu J$. The assorted colors of the OM micrograph indicate transitions from a surface structure to another. Indeed, panel [b] in Fig.(4.1) displays ripples appearing in the peripheral area of the irradiated spot and vanishing in the middle part, where a peculiar texture emerges.

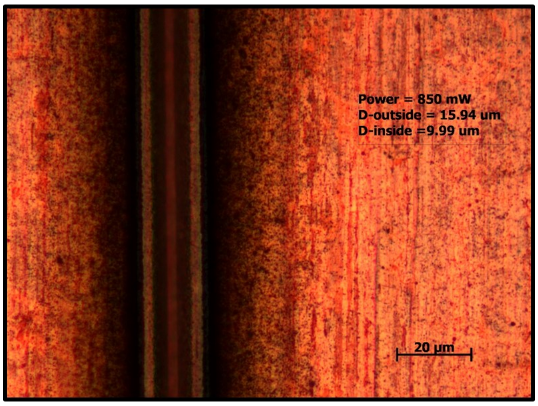

(a) Central part of the elliptical crater.

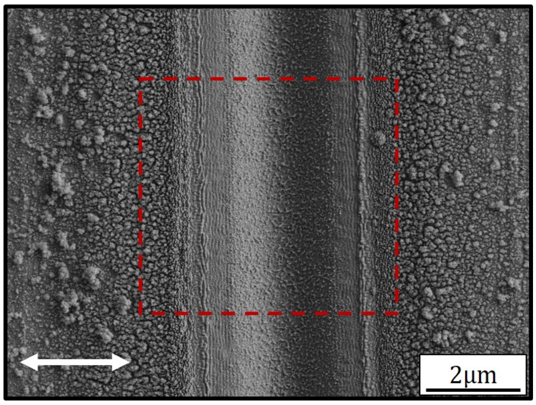

(b) SEM image displaying the structures of panel (a).

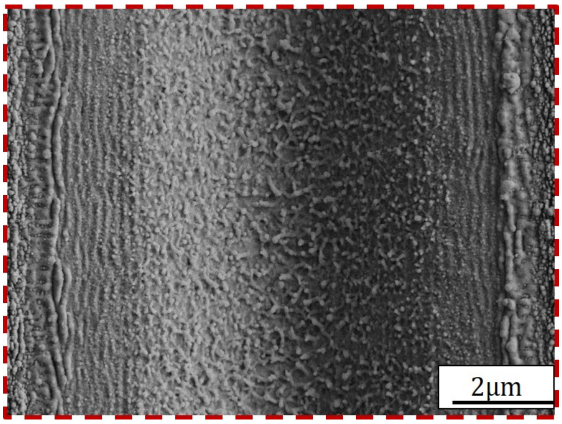

(c) Zoomed view of the dashed box in panel (a), registered at higher magnification.

Figure 4.1: Panels (a) and (b): OM and SEM views of the copper surface elaborated at $E = 170\ \mu J$ (peak fluence of $0.43\ J/cm^2$). The double headed arrow in panel (b) indicates the laser beam polarization. Panel (c): SEM micrograph exemplifying a zoomed view of the crater central area.

Moreover, the various tints of the OM image shown in panel [a], denote an inner region deeper with respect to the outward one. This aspect is confirmed by the SEM image of panel [b].
Panel [c] of Fig.(4.1) shows a magnified view of the zone in the dashed red box of panel [b]. This micrograph evidences ripples oriented perpendicular to the laser beam polarization whose direction is indicated by the double-headed arrow in Fig.(4.1) [a]. The central part of the spot features nanostructures in form of nanoprotusions and nanocavities. These structures have already been observed on copper in Ref.[66]. Using fs laser pulses at $\lambda = 800\ nm$ and $RR = 1\ kHz$, the authors produced nanostructures at various fluence regimes and number of shots. In particular, they have shown that at laser fluences ranging from $0.35\ J/cm^2$ up to $1.52\ J/cm^2$ and number of pulses varying from the single shot to $N = 1000$, the middle part of the irradiated spots exhibit surface textures similar to those we observe in this work.

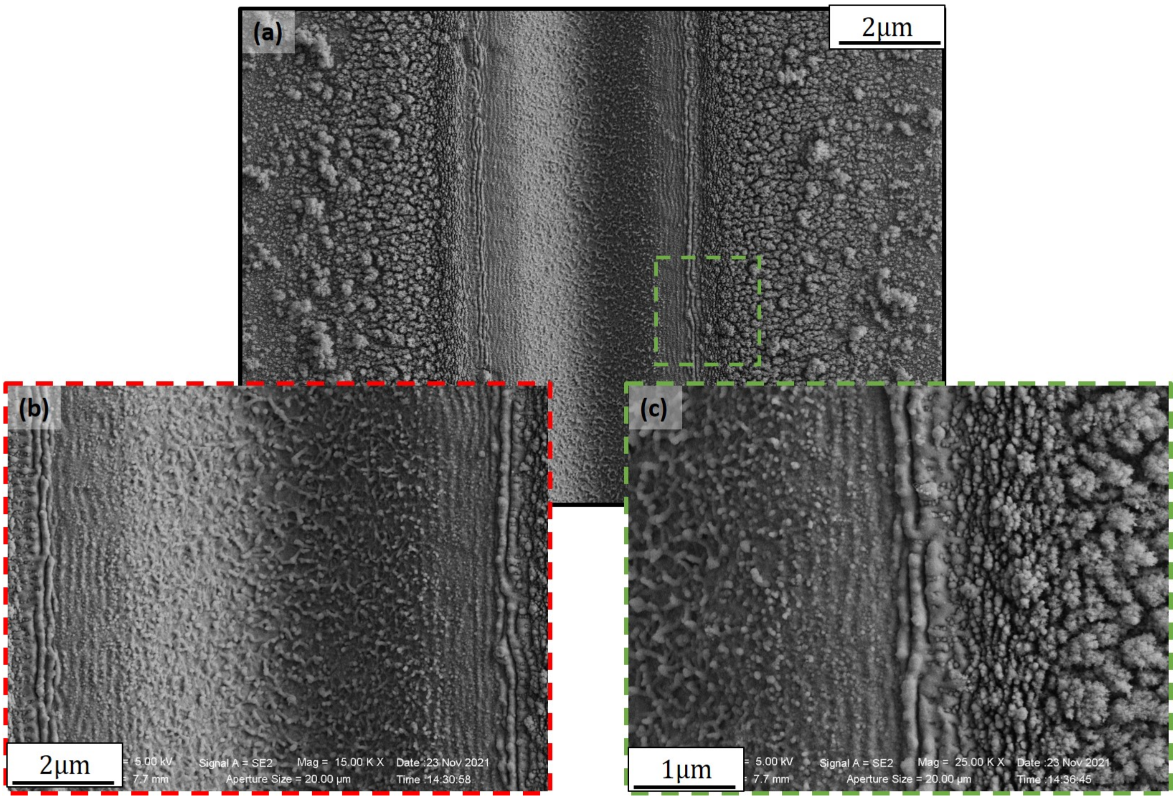

Figure 4.2: SEM images of the Cu surface irradiated by the laser beam focused with the cylindrical lens at the pulse energy of 197 μJ ($\phi_0 = 0.49\ J/cm^2$). Panel (a) reports the central area of the irradiated spot decorated with nanoparticles debris. Panels (b) and (c) show zoomed views of the crater in panel (a) at different magnifications.

A possible explanation behind the formation of these nano-protusions and -cavities relies on an initial non-uniform laser energy deposition. The factors that lead to a non-homogeneous absorption may be various, for example (i) the presence of defects on the sample; (ii) the inhomogeneity of the incident laser beam and (iii) the interference between the incident light and the excited surface electromagnetic wave due to the structural defects [66].

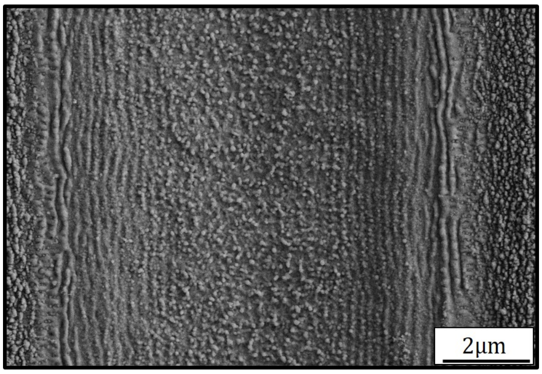

(a) $E = 94\ \mu J$.

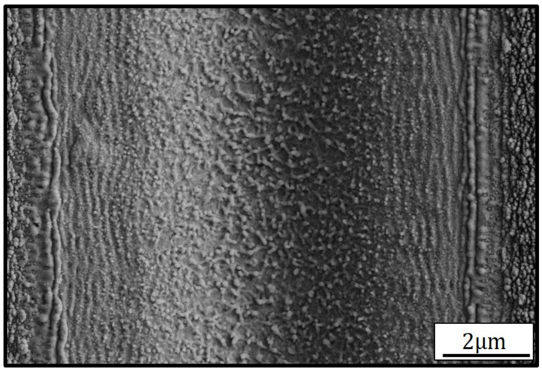

(b) $E = 140\ \mu J$.

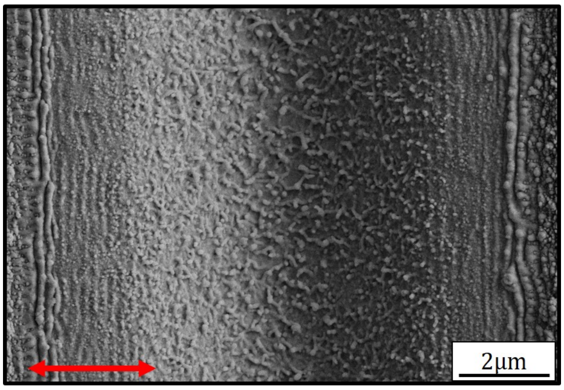

(c) $E = 183\ \mu J$.

Figure 4.3: Evolution of the morphological features on copper as the laser pulse energy increases. Here the corresponding laser fluence values are reported: (a) $\phi_0 = 0.24\ J/cm^2$, (b) $\phi_0 = 0.35\ J/cm^2$, (c) $\phi_0 = 0.46\ J/cm^2$. The red arrow displayed in panel [c] refers to the laser beam polarization.

Figure (4.2) displays an elliptical crater generated at $E = 197\ \mu J$. Even in this case the morphological features of the surface are described by ripples in the outer region and nanoprotusions and cavities in the internal part. In particular, the inset in the dashed green box shows a zoomed view of the morphological features of the surface at boundary of the crater. On the right side of ripples, the surface presents thick columns that form along the descent of the ablated structure. Periodic patterns seem to be impressed in the zone that flanks the outside part of the crater, where there are agglomerates of nanoparticles oriented along regular sequences. By moving away from the ablated region, these organized nanoparticles evolve into nanoparticles randomly distributed over the sample surface as shown in panels [a] of Figs.(4.1) and (4.2). The description of nanoparticles diffusion is discussed in Sect.(4.2).

The morphology of the induced structures is linked to the Gaussian intensity profile impinged on the material surface. In particular, ripples emerge in correspondence of the Gaussian tails where the fluence is low, but higher with respect to ablation threshold. In the present case, for the elliptical spots produced at the green wavelength, the fluence threshold ϕ_{th} is found to be $(0.13 \pm 0.04)\ J/cm^2$. At the peak value of $0.24\ J/cm^2$, and i.e slightly above the threshold, ripples start to appear on the surface of the target, as shown in panel [a] of Fig.(4.3). Here, periodic structures can be clearly seen in the peripheral area of the irradiated spot. Nevertheless, due to the low energy, a regular pattern seems to be impressed also in the internal area . As it can be observed in Fig.(4.3), as the laser fluence increases, the middle part of the crater gets deeper and larger, whereas ripples tend to extend in narrower spaces towards the crater rim. This phenomenon is observed in different works [38], [41]. In particular, the authors in Ref.[38] indicate as responsible of this effect the diverse excitation levels induced on the irradiated surface at different local fluences.

The description provided above for the craters produced at $\lambda = 515\ nm$ is suitable also for those elaborated at $1030\ nm$. In this case the fluence threshold found in Sect.(3.2) is $(0.24\ \pm\ 0.02)\ J/cm^2$.
Although the optical microscope allows to obtain images at a lower spatial resolution with respect to the scanning electron microscope, the OM images acquired in this case illustrate clearly visible ripples. Examples are shown in Fig.(4.4).
Panel [d] in Fig.(4.4) displays an elliptical crater formed at the peak fluence of $0.26\ J/cm^2$. This value is close to the threshold, therefore the surface structure seems little damaged. However, ripples can be distinguished in the peripheral and in central areas of the irradiated spot.
In particular, in the middle part of the ablated region, ripples are interrupted by irregular structures. The same type of morphology can be observed in panel [c] of Fig.(4.4). This micrograph displays an elliptical spot, produced at $0.29\ J/cm^2$, where the formation of textures in the internal part is more consistent. Moreover, as above discussed, the increase of laser fluence leads these complex structures to develop in the centre of the irradiated spot causing ripples to be confined at the borders of the crater.
The resolution of these OM images is not high enough to allow a detailed visualization of the morphological features of the internal part of the craters.
However on the basis of the SEM images above illustrated, these zones may exhibit nanostructures analogous to those we observed at $\lambda = 515\ nm$. Such a hypothesis can be better supported if we recall the induced nanostructures on copper in Ref.[66], ob-

tained by irradiating the target with an IR radiation, in a fluence regime and number of pulses that encounter our experimental conditions.

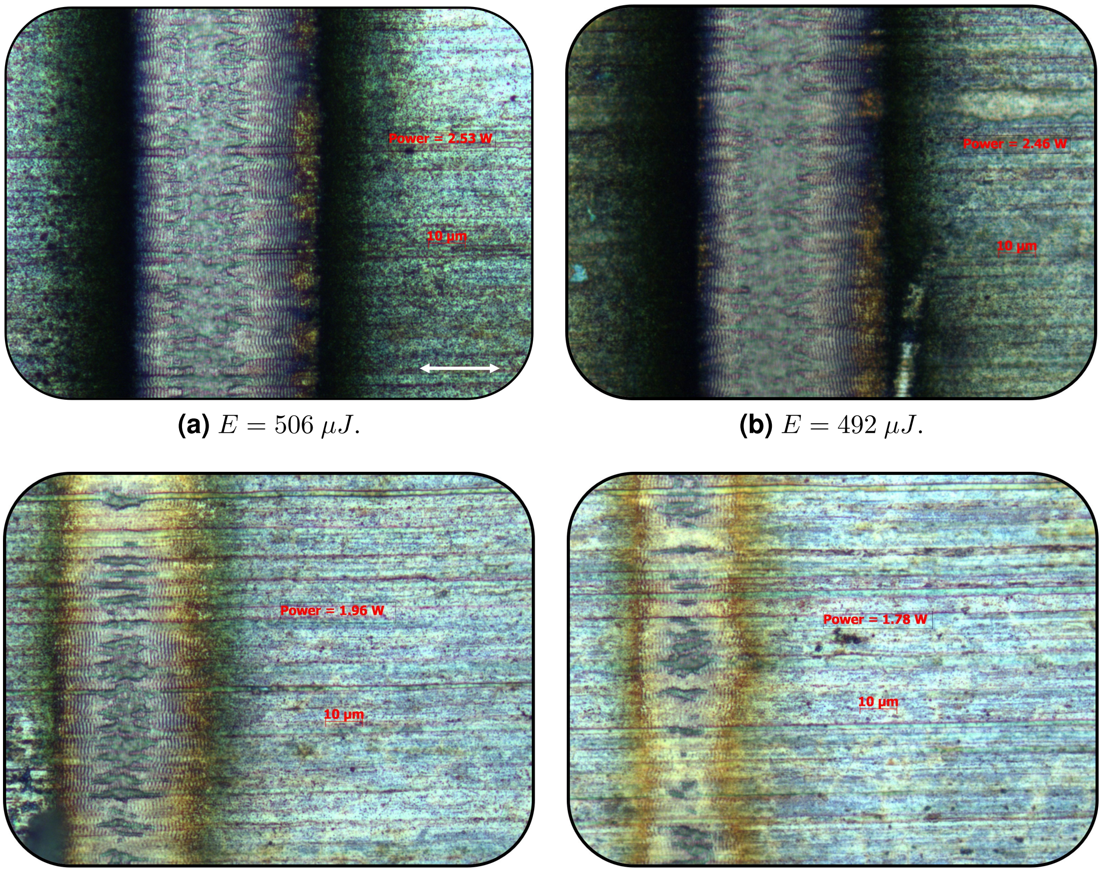

(a) $E = 506\ \mu J.$ **(b)** $E = 492\ \mu J.$

(c) $E = 392\ \mu J.$ **(d)** $E = 356\ \mu J.$

Figure 4.4: Morphological evolution of the structures as function of the energy. The corresponding values of the peak fluence are: (a) $\phi_0 = 0.37\ J/cm^2$, (b) $\phi_0 = 0.36\ J/cm^2$, (c) $\phi_0 = 0.29\ J/cm^2$, (d) $\phi_0 = 0.26\ J/cm^2$. The white arrow in panel (a) shows the direction of the laser beam polarization.

We turn now to investigate the ripples spatial period Λ as function of the energy. The current analysis was carried out on the SEM images exemplifying the craters elaborated at $\lambda = 515\ nm$ and on the OM images that visualise the structures produced at $\lambda = 1030\ nm$.

The measures were performed by means of Image J software. The program allows to select certain areas in order to produce the intensity spatial profile of the surface. An example is shown Fig.(4.5), where the inset in upper left corner displays a blue arrow that identifies the rippled region to analyse. The plot below represents the resulting spatial intensity profile. The ripples period was evaluated by measuring the distance between two consecutive minima as indicated by the green arrow in Fig.(4.5). After that the average ripples period with its standard deviation was estimated.

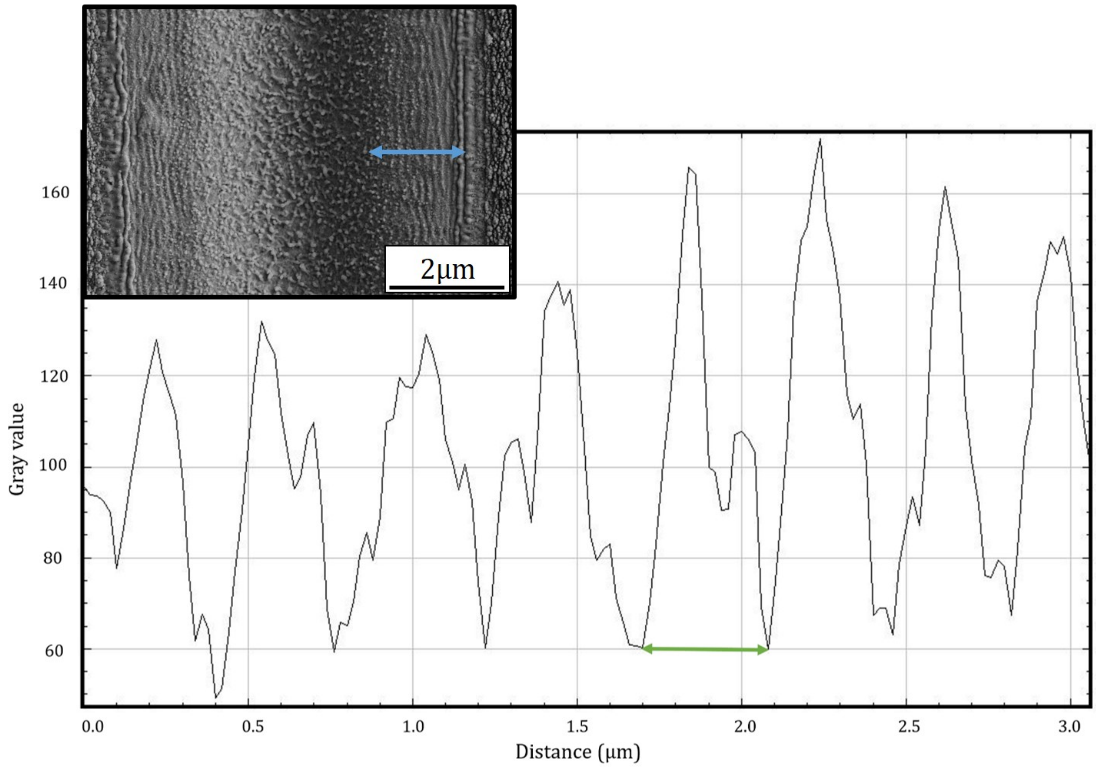

Figure 4.5: Scheme of the spatial intensity profile of a rippled region. The blue arrow in the upper left corner indicates the zone to analyse. The green arrow in the surface plot profile shows how the ripples period has been measured.

The dependence of Λ on E is traced in Fig.(4.6). The data reveal that, regardless of the wavelength, the ripples period does not change with energy. This result suggests, or rather confirms, what we discussed above i.e as the fluence increase the mechanism behind the formation of ripples does not change, but only their localization along the irradiated region gets modified. Therefore, considering the Gaussian spatial profile impressed on the surface, it can be ensured that ripples form in correspondence of the Gaussian wings. Since the values of Λ are consistent for each energy, we can estimate the average period of ripples at fixed wavelength. The results are reported in Tab.(4.2). From the data listed below, as well as from the plot in Fig.(4.6), one can notice that the period of ripples at $\lambda = 1030\ nm$ is higher with respect to that at $\lambda = 515\ nm$. This result is in agreement with the theory, in particular the values of Λ suggest that these periodic structures are part of the LIPSS family indicated as LSFL, for which

$\lambda/2 \leq \Lambda_{LSFL} \leq \lambda$ [see. Sect.(1.3)].

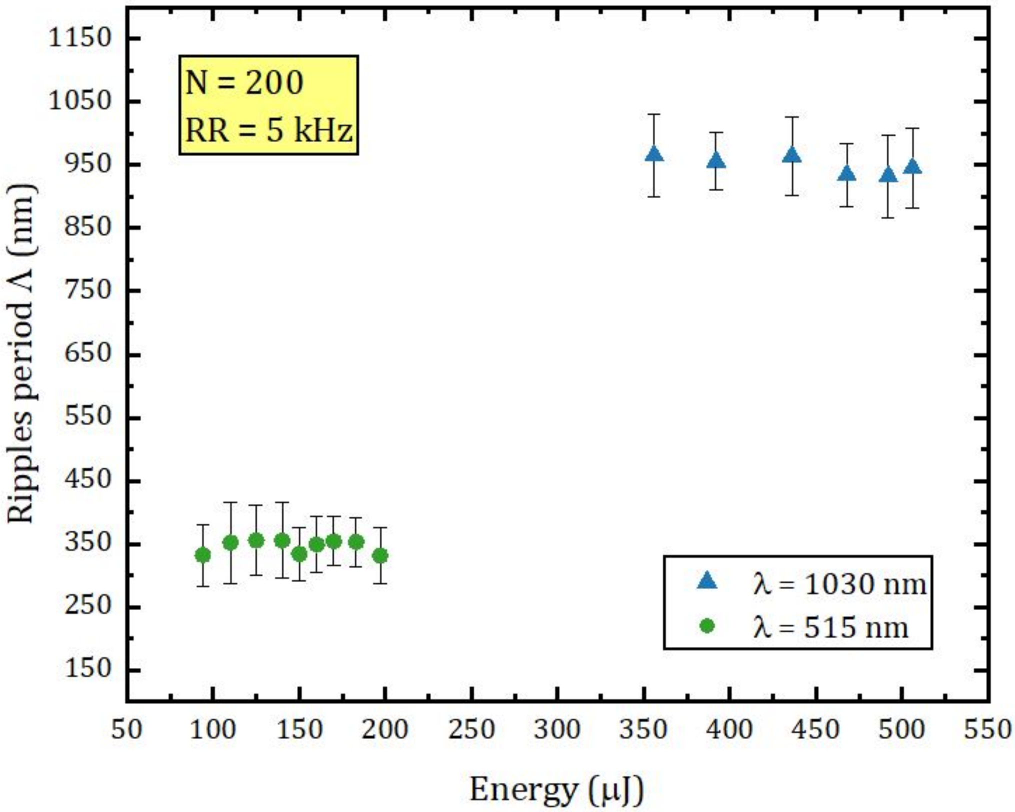

Figure 4.6: Variation of the spatial ripples period Λ as the energy increases. The green experimental points refer to measures performed on the SEM images exemplifying elliptical craters generated at $\lambda = 515\ nm$. The blue experimental points are relative to measures performed on the OM images exemplifying elliptical craters generated at $\lambda = 1030\ nm$.

Table 4.2: The average periods of ripples Λ corresponding to the strictures elaborated at $\lambda = 1030\ \ nm$ and $\lambda = 515\ \ nm$.

Wavelength λ (nm)	Ripples spatial period Λ (nm)
1030	950 $\pm$ 60
515	346 $\pm$ 49

Moreover, the registered data of Λ at the laser wavelength of $1030\ nm$ match other values reported in literature [40]. As regards the period evaluated at green wavelength, it is difficult to make a comparison with other experimental findings, since few works have been carried out at this wavelength. However, a value reported in literature is $\Lambda = 420\ nm$ [27], slightly above that displayed in Tab.(4.2). This may be due to the different experimental conditions, in particular to the number of applied pulses that in the case of Ref.[27] refers to an equivalent number of pulses, since the experiment was performed in dynamic irradiation condition.

In Sect.(1.3) we discussed about the mechanisms underlying LIPSS formation. In particular, we introduced two possible models: the electromagnetic and matter reorganization theories. Restricting our attention to the first theory, ripples form due to an interference between the incident laser beam and a surface electromagnetic wave scattered at the rough surface. In particular, we underlined that these processes may involve the excitation of the SPPs waves that propagate across the interface between two media, in this case, copper and air. In particular this model suggests a link between the spatial period of the modulated electromagnetic field Λ_{SPP} and the ripples spatial period Λ. Here, we recall the relation reported in Eq.(1.8):

$$\Lambda = \Lambda_{SPP} = \lambda\, Re\left\{\sqrt{\frac{\epsilon_m + 1}{\epsilon_m}}\right\} \tag{4.1}$$

where ϵ_m is the dielectric permittivity of the metal under consideration. According to Eq.(4.1) we calculated the ripples period for copper. Table (4.3) summarizes the results obtained from this calculation and the value of the copper dielectric permittivity exploited.

Table 4.3: Values of Λ obtained by using the theoretical formula in Eq.(1.8) and the value of the copper dielectric permittivity exploited.

Wavelength (nm)	$Re\{\epsilon_m\}$ at 300 K	$Im\{\epsilon_m\}$ at 300 K	$\Lambda\ (nm)$
1030	-45.761 [46]	4.5744 [46]	1019
515	-5.3328 [45]	6.1794 [45]	495

The values of Λ predicted theoretically are different from the experimental results reported in Tab.(4.2). This can be explained considering that the theory above discussed is valid for structures generated at few number of pulses. In our case $N = 200$, therefore a variation of the value of Λ is expected. The reduction of the rippled periodicity with increasing the number of pulses has been observed in different works [8], [10], [22], [61]. Several hypothesises have been advanced in order to elucidate this phenomenon that come under the feedback mechanisms of which we talked about in Sect.(1.3). Additional discussions about the dependence of the ripples period on N are provided in Chap.(5).

4.2 Deposition of nanoparticles debris accumulated around the craters

When a train of fs laser pulses hits the surface of a sample, part of the material is removed and results in a plume composed by ions, clusters, atoms and nanoparticles that remain above the target for several ns up to hundred of μs. In particular, due to the external ambient pressure the nanoparticles deposit back onto the surface in form of debris. One of the theory suggested to explain the deposition of debris is the shock wave theory [51]. We will not get into the details of this theory, since this task is out of the scope of the current thesis work. Nevertheless, we will try to give an idea of the process. When the plasma plume rises from the sample surface, it reaches an initial pressure P_b that depends on: (i) the ablated mass per pulse, (ii) the energy released in the ablation process, (iii) the size of irradiated area and (iv) the pulse duration [54]. As the plume expands, the cloud of the ablated particles gets accelerated towards the external environment, thus compressing the air molecules. This condition promotes the creation of a shock wave, defined as the geometrical surface that separates two regions of the same medium standing in different thermodynamic states [56]. The shock wave consists of a high-pressure front that causes the ambient air molecules to be forced at high densities, heated at high temperatures and accelerated at high velocities [54]. During the course of its expansion the pressure P_b decreases causing the cloud of ablated particles to slow down. As a consequence, the plume front gets divided from the shock wave front that spreads quickly until it reaches a critical radius R_B [51]. The critical radius is defined as the distance at which the pressure in the shock wave reaches the ambient air pressure P_0. Plume expansion stops at a distance R_P less than R_B. It has been found that $R_P \sim fR_B$ where f varies in a window of $0.3 \div 0.5$ [54]. When the shock wave becomes weak and the cloud of the ablated particles cools down, the ambient gas flows back into this region dragging the nanoparticles of the plume towards the target surface. In the best scenario of a radial expansion of the plume, nanoparticles debris are expected to cover a ground with a radius of a fraction of R_B [51], [54].

In this frame we start to consider the circular craters generated on the copper target by focusing the laser beam with a spherical lens having a focal length of 200 mm. Table (4.4) recalls the experimental condition used in this case.

Table 4.4: Experimental conditions for the fs laser structuring of a copper target, in the case of the spherical lens.

N	λ (nm)	Rep. Rate (kHz)	Pulse energy (μJ)	Peak fluence (J/cm^2)
200	1030	$(3 \div 30)$	$(30 \div 60)$	$(0.3 \div 0.6)$

The values of the peak fluence are calculated by using $\phi_0 = 2E/S$ where S is

reported in Tab.(3.7) of Sect.(3.1).
Figure (4.7) reveals OM images of the craters generated at $RR = 25\ kHz$. As discussed in Sect.(3.1) the faded annulus around the circular spots corresponds to the portion of the surface where nanoparticles deposited. The OM micrographs evidence debris uniformly covering the area around the ablated craters. The crater formed at $E = 40\ \mu J$ and displayed in panel [a] of Fig.(4.7), features weak colors indicating a reduced amount of sediments. The sharp tints of the crater obtained at $E = 55\ \mu J$ and displayed in panel [b], instead, denote a greater amount of debris. This is expected since the higher is the energy, the more is the removed material.

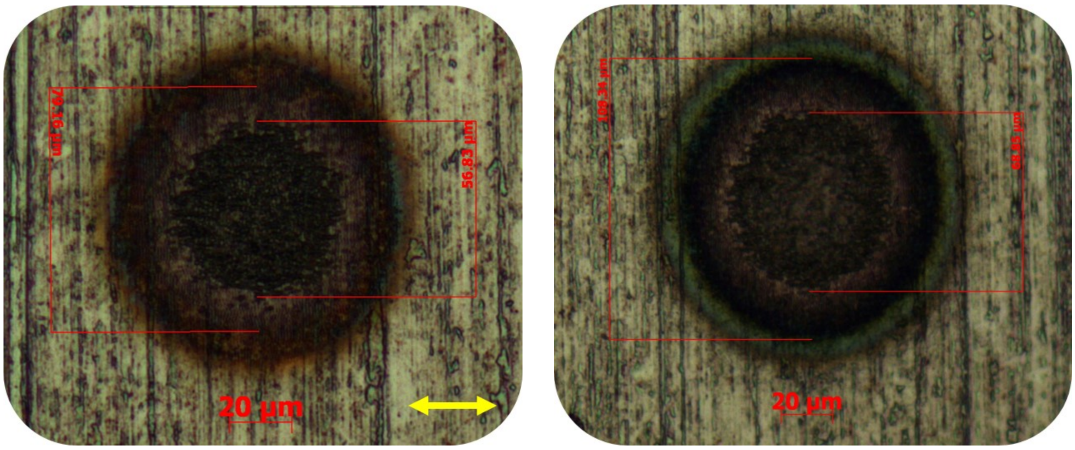

(a) $E = 40\ \mu J$. **(b)** $E = 55\ \mu J$.

Figure 4.7: OM images exemplifying circular craters generated with the spherical lens at $\lambda = 1030\ nm$ and $RR = 25\ kHz$. The yellow arrow in panel (a) indicates the laser beam polarization.

Similar observations are found in Ref.[51] where nanoparticles debris were studied on a Si substrate irradiated with $N = 100$ pulses and at laser energies in the range $(1 \div 25)\ \mu J$. These authors noticed that at low fluence values the recognition of debris in the outer ring of the structure is not easy. According to the theory above explained, they suggest that at low fluence regimes the plasma plume reaches quickly the value R_P at which the expansion stops. This condition leads the ambient air to drag onto the surface a small quantity of nanoparticles.

In order to evaluate the thickness t of the substrate were nanoparticles are deposited, we performed several measures by using Image J software. Initially, we measured the area A of the total region where nanoparticles are observed, as illustrated in panel [a] of Fig.(4.8). By averaging the registered values of A, the diameter d_{np} of the zone under consideration and its error $\sigma_{d_{np}}$ are derived by using Eq.(4.2):

$$d_{np} = 2\sqrt{\frac{A}{\pi}} \qquad \text{and} \qquad \sigma_{d_{np}} = \sqrt{\frac{1}{\pi A}}\sigma_A \tag{4.2}$$

where σ_A is the standard deviation of A.
Considering the average diameter d_{th} already estimated in Sect.(3.1), we derived the thickness t and its error as follow:

$$t = \frac{d_{np} - d_{th}}{2} \qquad \text{and} \qquad \sigma_t = \frac{\sigma_{d_{np}} + \sigma_{d_{th}}}{2} \tag{4.3}$$

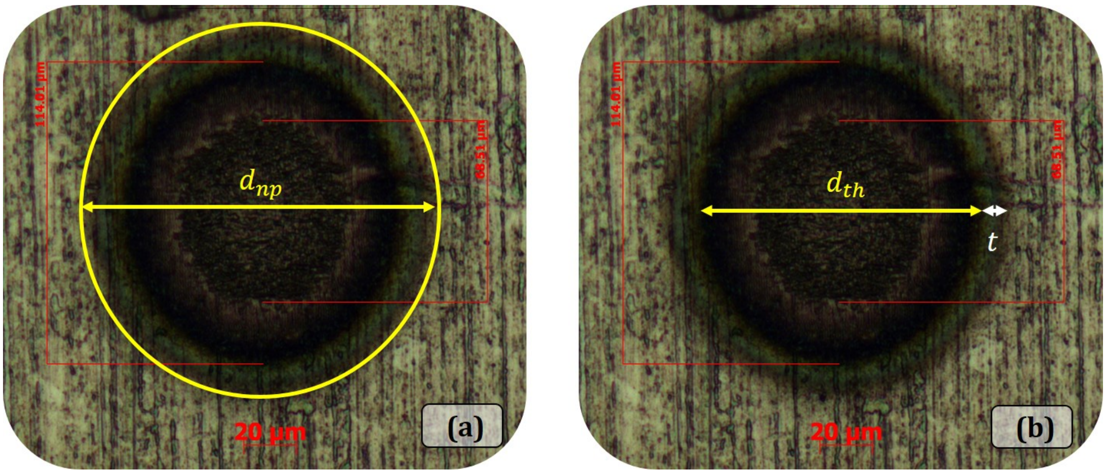

Figure 4.8: Scheme of the measurement procedure. Panel (a) exemplifies the measure of A and d_{np}, panel (b) indicates the zone t we refer to.

Figure (4.9) reports the experimental results on the variation of t as function of the pulse energy E, for each repetition rate. The plot shows the linear dependence of t on E, i.e as the energy increases the debris covers larger portion of substrate. The data reveal that the various repetition rates do not affect the redeposition dynamic of nanoparticles. In fact, the experimental points overlap each other and tend to align along a common line. This is expected since in Sect.(3.1) it has been shown the removal of material is independent on the variation of repetition rates. In particular, we notice that in our experimental conditions the plasma plume is not dense enough to interfere with the incoming train of pulses.

The linear tendency in Fig.(4.9) indicates that t reaches the zero value at an energy close to the ablation threshold explored in Sect.(3.1). Therefore, in order to confirm this observation and to verify if the Gaussian beam profile has a sort of influence on the nanoparticles distribution, the fitting procedure in Eq.(3.9) is performed between r_{np}^2 and $ln(E)$ in the following.

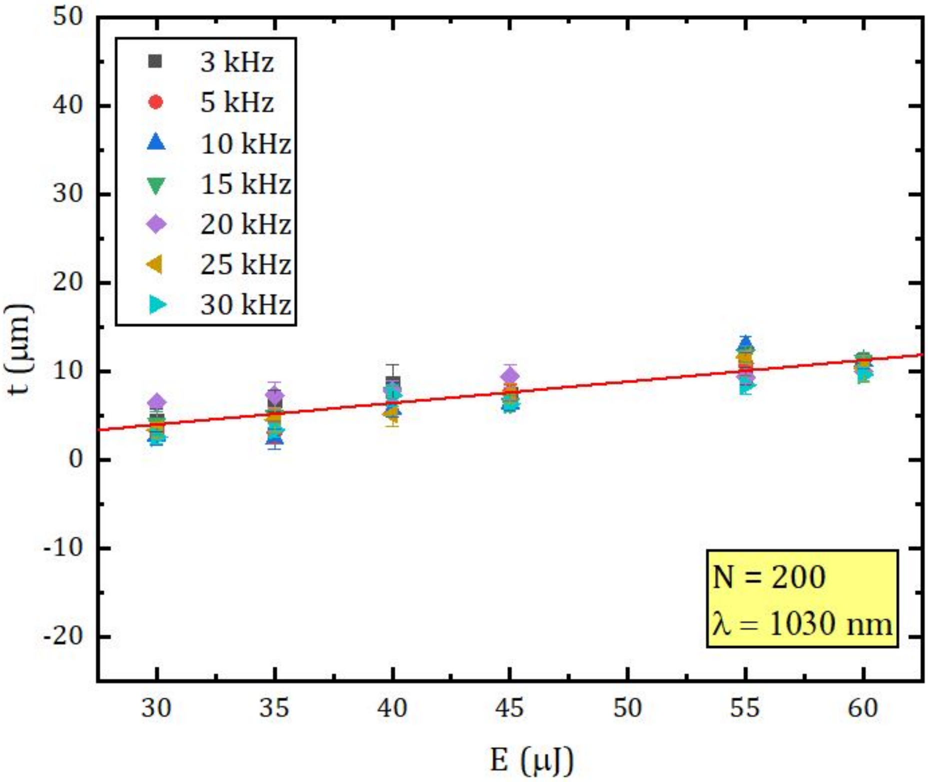

Figure 4.9: Variation of the thickness t as function of the pulse energy E at each RR raging from 3 kHz up to 30 kHz. The solid line indicates the linear trend of the experimental points.

Note that r_{np} is the radius of the region where nanoparticles extend and, on the basis of the above discussion, it was obtained performing a weighted average of d_{np} by fixing energy and varying the repetition rate. Figure (4.10) shows the variation of r_{np}^2 as function of $ln(E)$ and, for comparison, it also reports the trend of r_{th}^2 on $ln(E)$ already studied in Sect.(3.1). The graph evidences that, minus a π factor, the area covered by nanoparticles follows an analogous tendency to that observed for the ablated craters.
By using the relations in Eq.(3.3) the values of the energy threshold and of the laser spot size were calculated. Table (4.5) reports the data obtained from this analysis and recalls those achieved in Sect.(3.1). The data listed below indicate that the energy thresholds for ablation and for generation of nanoparticles sediments are in agreement within the errors. On one hand this is reasonable since the production of nanoparticles starts as a consequence of the laser ablation process. On the other hand, this means that as soon as E reaches E_{th}, the deposition of nanoparticles occurs immediately. The registered values of w_0 are different in the two cases. This result seems to suggest that the Gaussian profile of the beam has some direct influence on the spreading of the nanoparticulate

debris over the target surface. However, the larger value of the spot size parameter might indicate a more complex initial distribution of the plume of nanoparticles as well as more intricate phenomena involved in their confinement by the surrounding atmosphere and back-deposition.

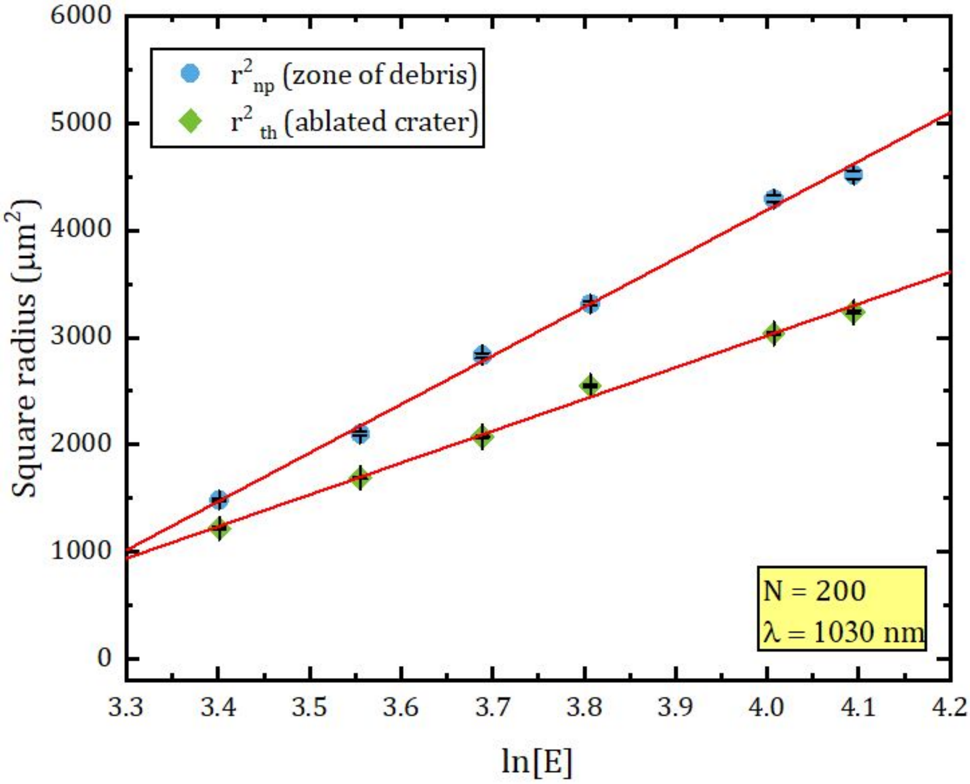

Figure 4.10: Variation of the squared radii r^2_{np} and r^2_{th} as function of the natural logarithm of E in the range $(30 \div 60)\ \mu J$.

Table 4.5: Values of the energy thresholds and the laser spot size resulting from the linear fits r^2_{np} vs. $ln(E)$ and r^2_{th} vs. $ln(E)$.

	Energy threshold (μJ)	Spot size (μm)
Zone of debris	(22 ± 1)	(95 ± 2)
Ablated crater	(20 ± 1)	(77 ± 1)

We turn now to investigate the redeposited debris mass in the case of the elliptical craters produced by focusing the laser beam with a cylindrical lens having a focal length of $150\ mm$. Here, the Cu target was irradiated at $\lambda = 1030\ nm$ and $\lambda = 515\ nm$. In the former case, the energy delivered to the sample was in the range of $(356 \div 506)\ \mu J$. This range corresponds to the fluence variation window of $\phi_0 = (0.26 \div 0.37)\ J/cm^2$. In the latter, the energy varied from $94\ \mu J$ up to $197\ \mu J$, hence the fluences were $\phi_0 = (0.24 \div 0.49)\ J/cm^2$. In both cases, the copper target was irradiated with a sequence of $N = 200$ pulses at $5\ kHz$.

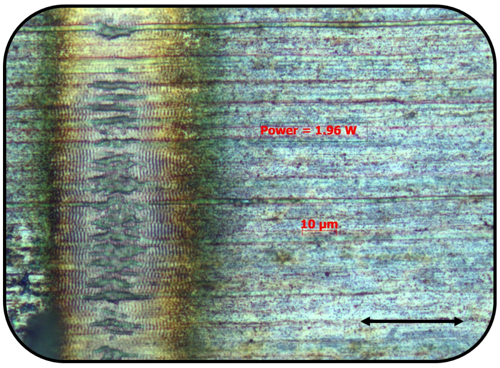

(a) $E = 392\ \mu J$.

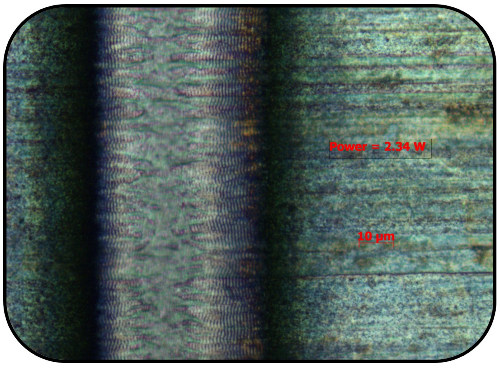

(b) $E = 468\ \mu J$.

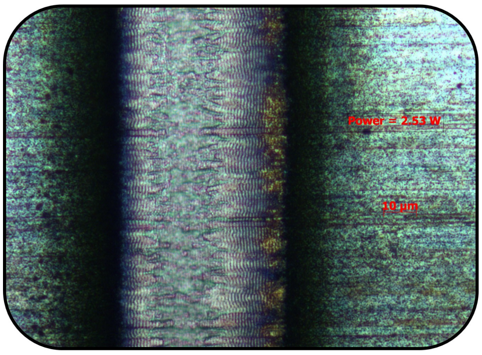

(c) $E = 506\ \mu J$.

Figure 4.11: OM images of elliptical craters generated by focusing the laser beam with the cylindrical lens. The picture visualises the morphological evolution of the structure as the pulse energy E increases. The black arrow in panel [a] indicates the laser beam polarization.

Figure (4.11) reports OM images exemplifying the surface structures elaborated at the IR wavelength. The picture displays the morphology of the redeposited debris at different energies. Most of the debris are deposited near to the ablated region, except for the debris in panel [c] generated at $E = 506\ \mu J$ where one can note a slight dissemination of nanoparticles far away from the crater.

By using Image J software the distance x_{np} indicated in panel [a] of Fig.(4.12) was measured. Subsequently, the average value of x_{np} and its standard deviation $\sigma_{x_{np}}$ were determined. Considering the the distance x_{th} estimated in Sect.(3.2), we evaluate t and its error σ_t as follow:

$$t = \frac{x_{np} - x_{th}}{2} \qquad \text{and} \qquad \sigma_t = \frac{\sigma_{x_{np}} + \sigma_{x_{th}}}{2} \tag{4.4}$$

This parameter t represents the thickness where nanoparticles diffuse on one side of the crater.

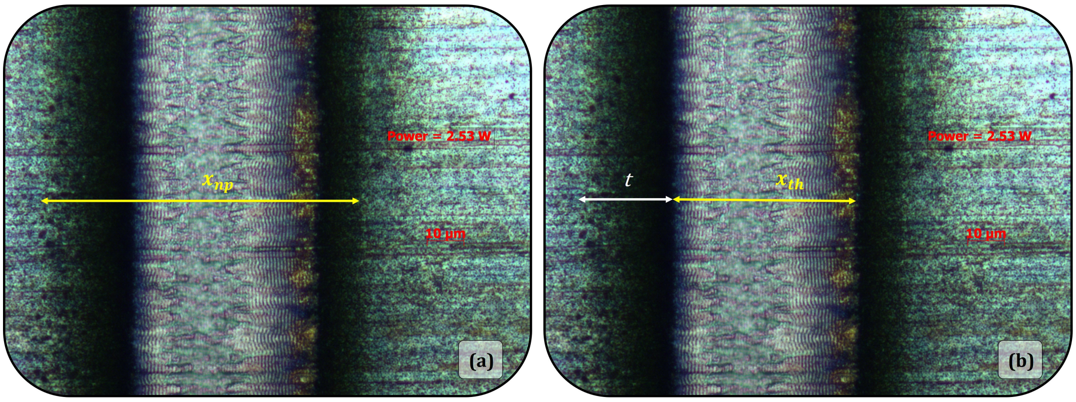

Figure 4.12: Example of the measurement procedure. Panel (b) identifies the zone t where nanoparticles deposit.

Figure (4.13) shows the linear dependence of t on E. As expected, at high energy values the distance reached by the debris is longer with respect to the case of low energy values. In particular, the line fit to the data seems to reach the zero value at $E \lesssim 340\ \mu J$. This value is close to the energy threshold for ablation found in Sect.(3.2) and recalled in Tab.(4.6).

This observation suggests to perform a fitting procedure between r_{np}^2 and $ln(E)$, where r_{np}^2 indicates the squared value of $x_{np}/2$. The linear fit was performed by using the formula in Eq.(3.9), from which the laser spot size w_{np} and the energy threshold E_{np} were derived. Table (4.6) reports the values obtained from this analysis, compared with those obtained in Sect.(3.2) for the elliptical spots produced at $\lambda = 1030\ nm$.
The data listed in Tab.(4.6) show that the energy thresholds are in fairly good agreement each other, whereas the values of the laser spot size are very far apart. Figure (4.14) [a] recalls the linear dependence of r_x^2 on $ln(E)$ studied in Sect.(3.2) and reports the results of the linear regression fit performed in this frame. The solid line representing the trend of r_{np}^2 on $ln(E)$ matches the experimental points at low energies. At high energy values, the points seem to follow another tendency.
This observation recommends to run a linear regression on the first four points and to compare the fit parameters gained in this case with those obtained in the ablation threshold study.

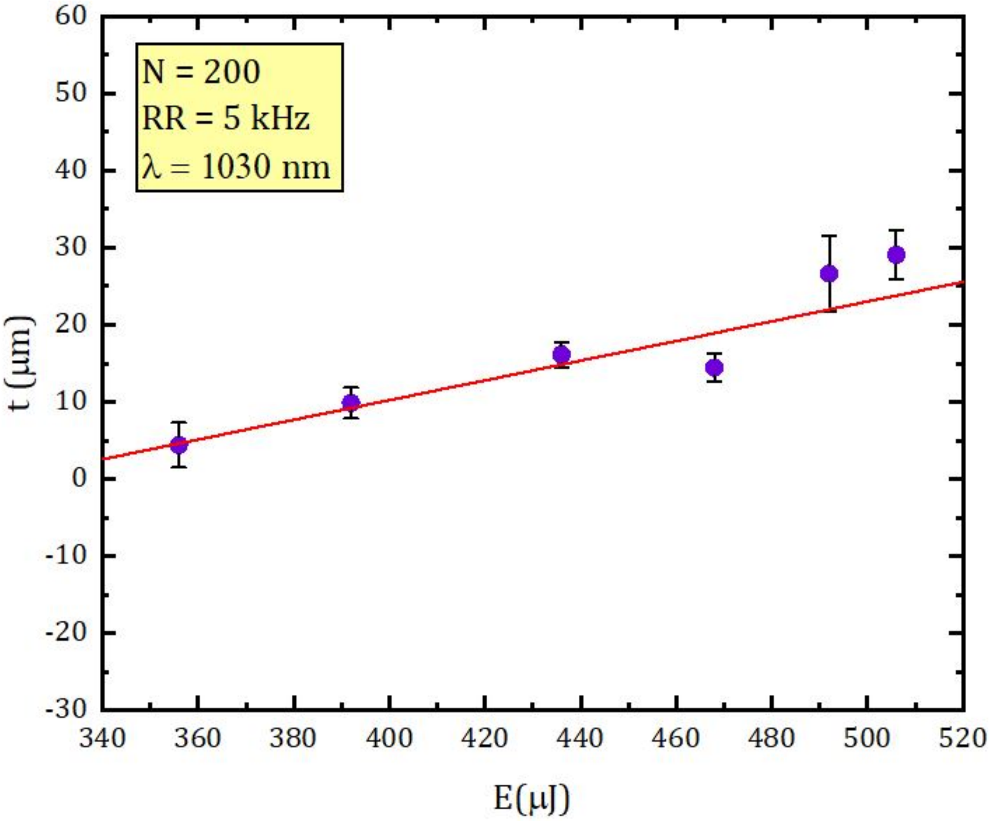

Figure 4.13: Dependence of the thickness t of the debris film on the pulse energy E ranging from 356 μJ to 506 μJ.

Panel [b] of Figure (4.14) and Table (4.7) reports the experimental results obtained from this analysis. Here, it is possible to notice that the energy thresholds are pretty consistent each other, whereas the spot sizes are still different.
Therefore one can suggest that in the regime of low fluences the zone of debris depends on the variation of the Gaussian beam profile, whereas at high fluence regimes the nanoparticles dispersion trend changes due to some diffusion processes during nanoparticles deposition.

The same type of analysis is carried out on the OM images exemplifying craters generated at $\lambda = 515$ nm. Figure (4.15) shows three OM micrographs representative of craters generate at low, medium and high energy values.

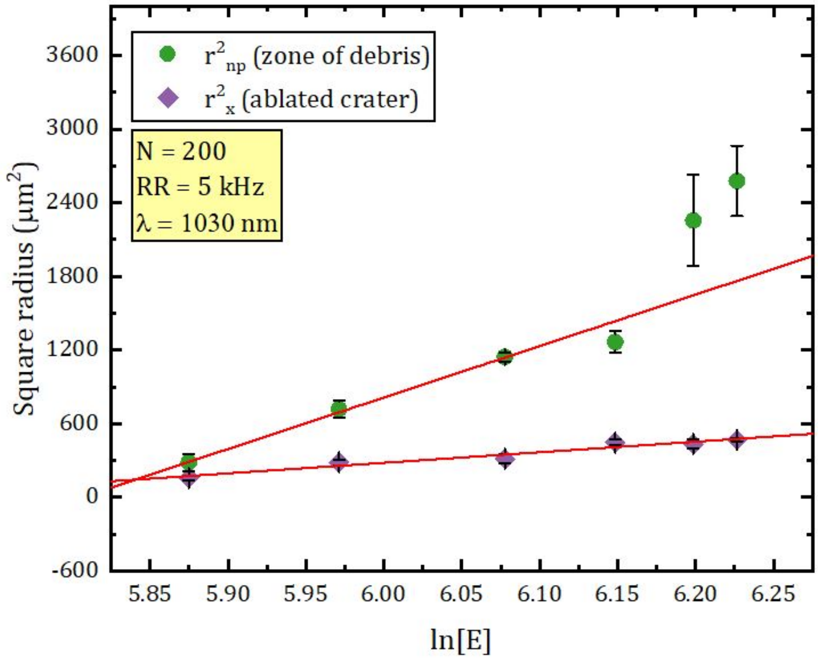

(a) r_{np}^2 vs. $ln(E)$ and r_{th}^2 vs. $ln(E)$.

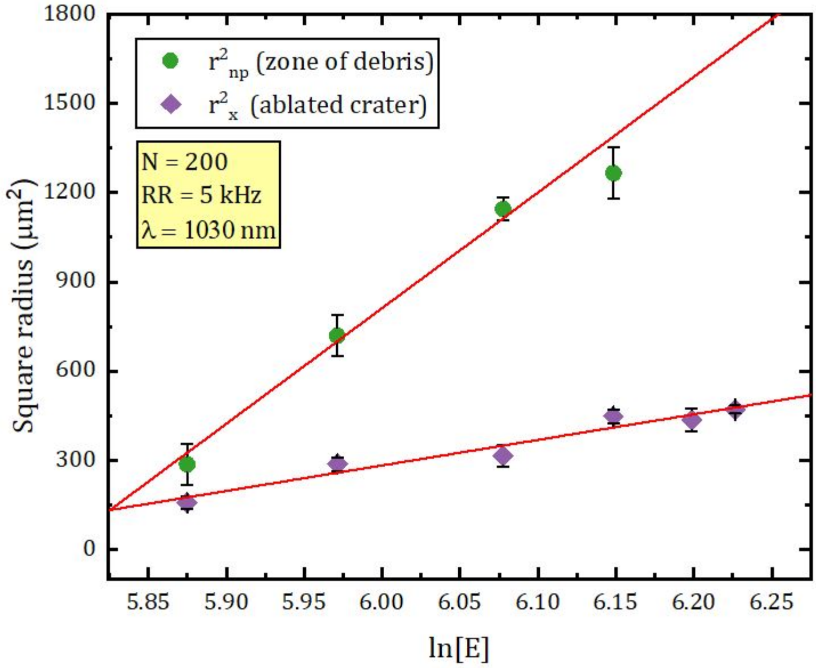

(b) r_{np}^2 vs. $ln(E)$ and r_{th}^2 vs. $ln(E)$.

Figure 4.14: Variation of squared radii r_{np}^2 and r_{th}^2 as function of the natural logarithm of E in the range $(356 \div 506)\ \mu J$. The trend in panel (a) refers to the complete energy range. The trend in panel (b) refers to the low energy range.

Table 4.6: Experimental results obtained from the linear fits r_{np}^2 vs. $ln(E)$ and r_{th}^2 vs. $ln(E)$. These data refers to the linear tendency of panel [a] in Fig.(4.14).

	Energy threshold (μJ)	Spot size (μm)
Zone of debris	(349 ± 17)	(110 ± 10)
Ablated crater	(323 ± 16)	(42 ± 3)

Table 4.7: Experimental results obtained from the linear fits r_{np}^2 vs. $ln(E)$ and r_{th}^2 vs. $ln(E)$. These data refers to the linear tendency of panel [b] in Fig.(4.14).

	Energy threshold (μJ)	Spot size (μm)
Zone of debris	(325 ± 9)	(86 ± 5)
Ablated crater	(323 ± 16)	(42 ± 3)

Unlike the previous case, nanoparticles sediments seem to cover a larger portion of the copper substrate. In particular, near the ablated region the distribution of nanoparticles appears uniform whereas far away from the crater the debris seem to cover the surface in a sparse manner. Such a behaviour is more visible in panel [c] of Fig.(4.15) that displays the crater generated at the highest pulse energy used in this thesis work. Therefore, from a qualitative point of view, the covering dynamics of the target surface appears different as the energy increases. Each OM image is provided of a SEM inset that visualises the amount of nanoparticles over the Cu surface. As it can be observed, the quantity of nanoparticles grows as the energy increases. In fact, the SEM view of panel [c] displays agglomerates of nanoparticles greater than those illustrated in the dashed green box of panels [b] and [c]. This trend is understandable since the higher the energy, the more the removal of the material.

Figure (4.16) shows the dependence of the zone were nanoparticles are observed, i.e the thickness t, on the pulse energy E. Comparing this linear trend to that in Fig.(4.13), it can be noticed that, unlike the IR wavelength, the rise of t in E is enhanced in the case of the green wavelength. This results can be explained considering that at $\lambda = 515\ nm$ the copper surface absorbs more radiation with respect to at $\lambda = 1030\ nm$. As a consequence, the amount of particles standing in the plasma plume is more consistent in the case of the green wavelength and thus the sediments deposited onto the surface are greater.

In order to explore the influence of the Gaussian beam profile variation on the debris distribution, the linear fitting procedure between r_{np}^2 and $ln(E)$ was performed. The dependence of r_{np}^2 on $ln(E)$ is shown in Fig.(4.17). As observed, the solid line matches only the first three experimental points at low energy values.

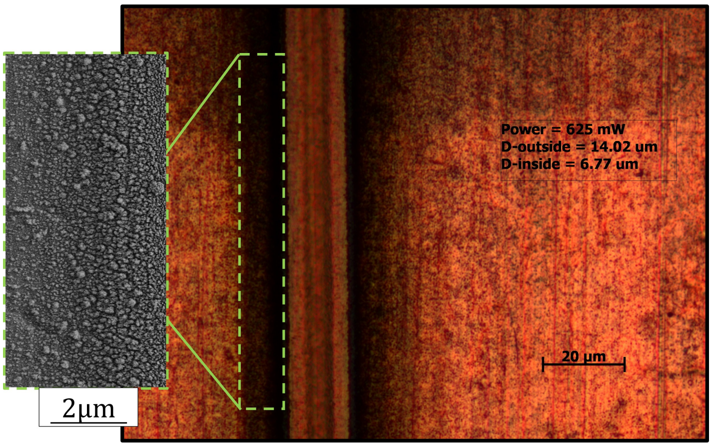

(a) $E = 125\ \mu J$.

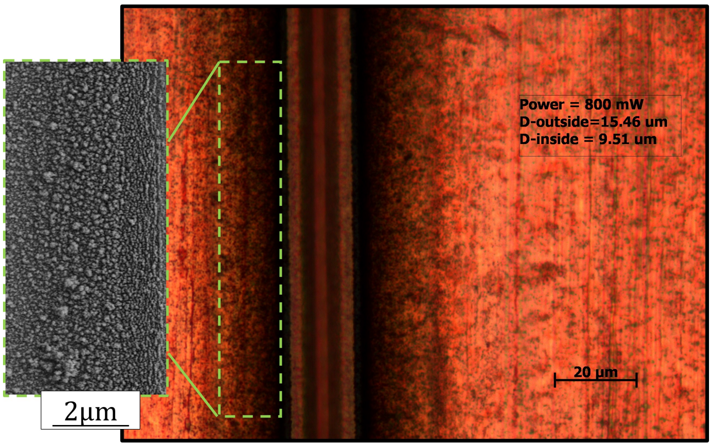

(b) $E = 160\ \mu J$.

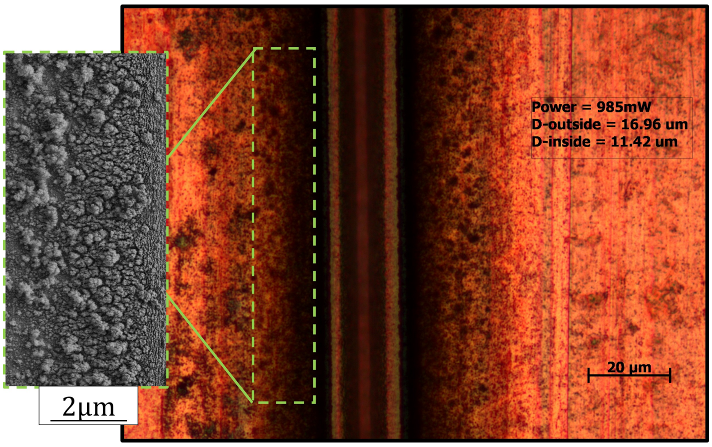

(c) $E = 197\ \mu J$.

Figure 4.15: OM images of the elliptical craters generated at $\lambda = 515\ nm$. Each OM view has insets exemplifying a SEM micrograph corresponding to the OM area in the dashed green box.

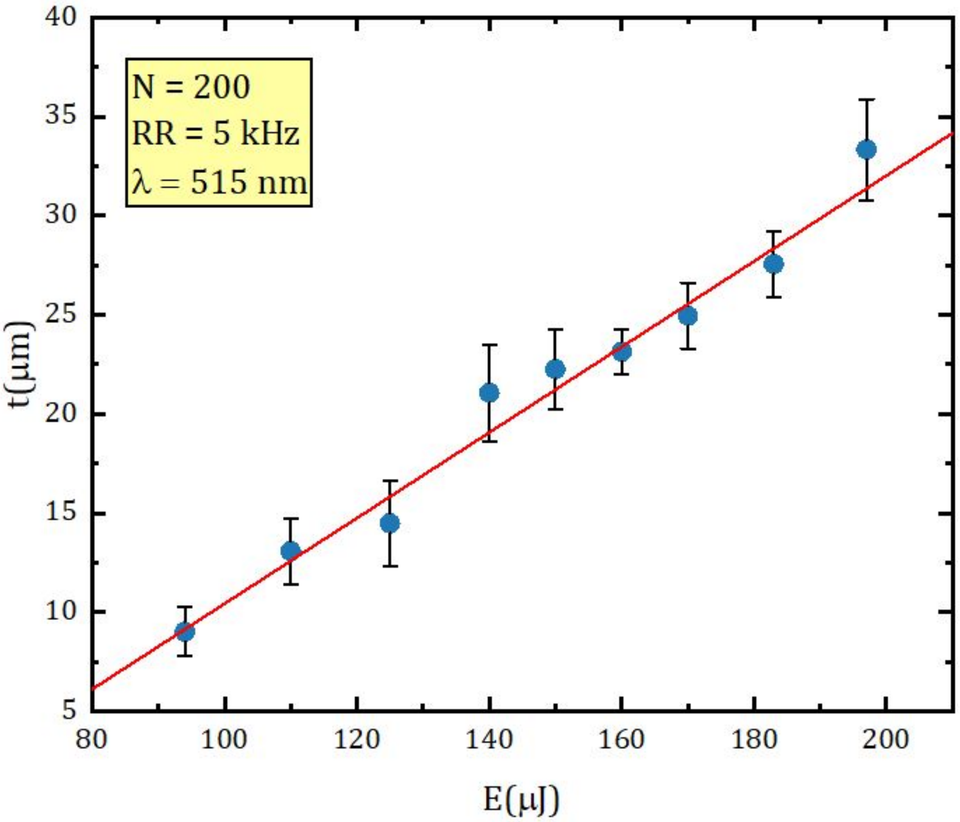

Figure 4.16: Variation of the thickness t as function of the pulse energy E in the range $(94 \div 197)$ μJ.

As the energy increases, the experimental points seems to follow other tendencies. In particular it is possible to recognize two different trends appearing at medium and high energy values, respectively. This observation agrees with the qualitative description provided above for the OM images. Table (4.8) lists the values of the energy threshold and laser spot size gained from this analysis. This results are compared with those obtained in Sect.(3.2) for ablation threshold. As expected, the energy thresholds and the laser spot sizes are not in good agreement each other. Therefore, basing also on the previous discussion, it was carried out a linear fitting procedure only on the three first experimental points. The solid line in Panel [b] of Fig.(4.17) confirms the linear trend of r_{th}^2 on $ln(E)$ expected in this case. Table (4.9) summarizes the results obtained from this analysis. Here, we note that the agreement with the energy thresholds gets improved, although they are not consistent within the errors, whereas the values of w_0 are still distant.

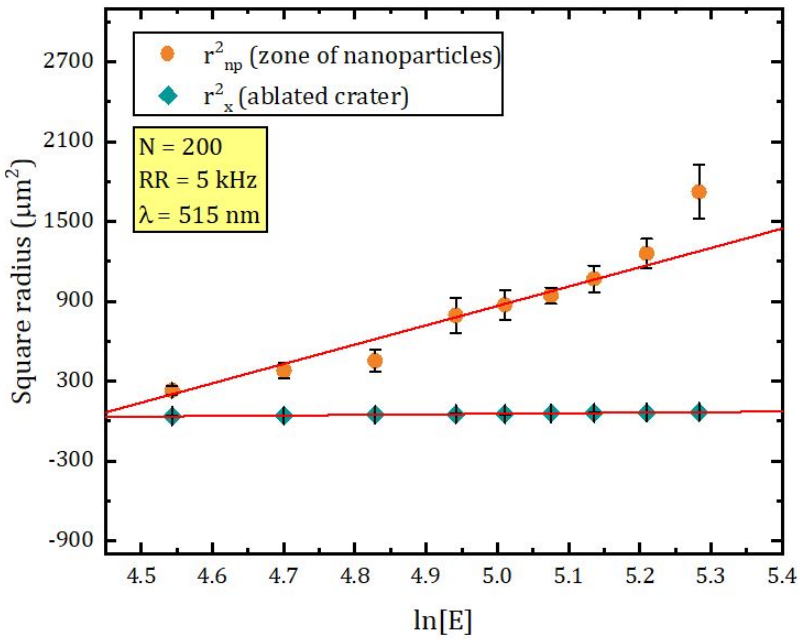

(a) r^2_{np} vs. $ln(E)$ and r^2_{th} vs. $ln(E)$.

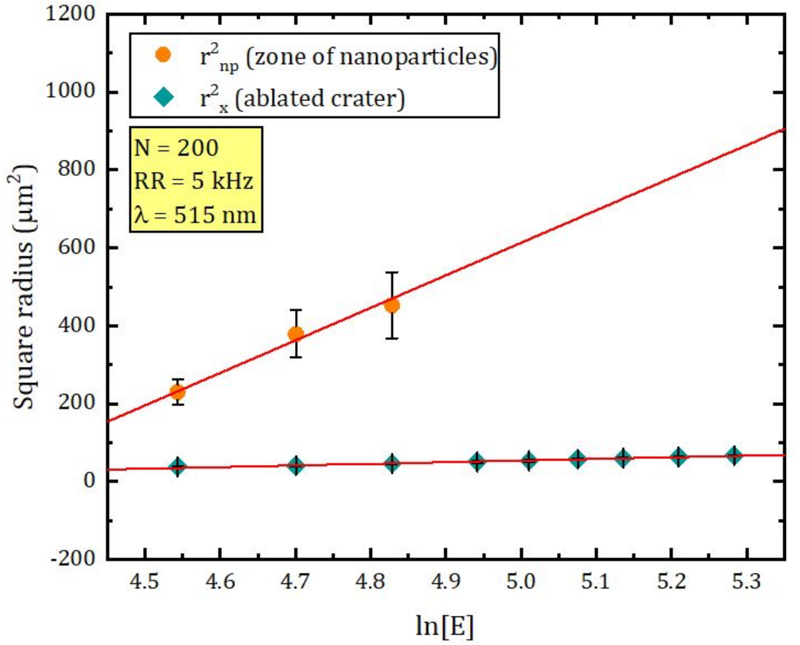

(b) r^2_{np} vs. $ln(E)$ and r^2_{th} vs. $ln(E)$.

Figure 4.17: Variation of the squared radii r^2_{np} and r^2_x as function of the natural logarithm of E in the range $(94 \div 197)\ \mu J$. Panel (a) refers to the linear fit performed in the total energy range, whereas panel (b) illustrates the result of the linear fit at low energy range.

Table 4.8: Experimental results obtained from the linear fits r_{np}^2 vs. $ln(E)$ and r_{th}^2 vs. $ln(E)$. These data refers to the linear tendency of panel [b] in Fig.(4.17).

	Energy threshold (μJ)	Spot size (μm)
Zone of debris	(90 ± 6)	(61 ± 4)
Ablated crater	(61 ± 5)	(9.4 ± 0.1)

Table 4.9: Experimental results obtained from the linear fits r_{np}^2 vs. $ln(E)$ and r_{th}^2 vs. $ln(E)$. These data refers to the linear tendency of panel [b] in Fig.(4.17).

	Energy threshold (μJ)	Spot size (μm)
Zone of debris	(70 ± 4)	(40 ± 3)
Ablated crater	(61 ± 5)	(9.4 ± 0.1)

For the sake of simplicity, the main results gained from these analyses are below reported.

- Concerning the craters elaborated with the spherical lens at $\lambda = 1030\ nm$, it has been found that the dependence of r_{np}^2 on $ln(E)$ is linear in accordance with Eq.(3.2). Moreover, the close values of the energy thresholds for ablation and for debris formation suggest that Gaussian beam profile somewhat affects the dynamics of nanoparticles distribution. This may explain also why the sediments are arranged in a ring that follows the circular shape of the craters.

- In the case of the cylindrical lens the experimental findings evidence interesting results. First of all, the laser wavelength influences the amount of debris deposited on the surface. In fact, as above discussed at $\lambda = 515\ nm$ the production of nanoparticles is higher than at $\lambda = 1030\ nm$. Moreover in both cases, it is possible to notice that the dynamics of nanoparticles distribution seems to depend on the fluence regimes. In particular, at low fluence values the debris coverage of the substrate seems to be mostly affected by the Gaussian beam profile.

The trends observed in the case of the cylindrical lens are different from those observed in the case of the spherical lens. This is likely due to the different geometries of the plasma plume expansion in the two cases. In particular, the distribution of nanoparticles in the case of the spherical lens can be described by the model introduced at the begging of this Section. As regard the cylindrical lens, an implemented model should be find since there is still not a model aimed to explain the experimental findings of this work. Moreover, a preliminary qualitative analysis seems to show a dependence at low energy resembling the one related to the variation of the elliptical Gaussian beam profile, whereas of a wide energy range the size of the covered region seems to be better described by a linear dependence on the energy. A clarification of such effects should deserve further experimental and theoretical analyses to clarify the mechanisms underlying the coverage of nanoparticulate debris and its dependence on the laser beam shape and energy.

Chapter 5

Laser surface texturing of copper over large areas

The aim of this chapter is to investigate the surface structures developed on millimeter size areas by the raster scanning of the laser beam on the copper surface. In particular, in Sect.(5.1) we deal with the subwavelength structures typically generated in the direct femtosecond laser surface structuring process, whereas in Sect.(5.2) we focus on the morphological features of a textured area.

5.1 Generation of ripples on large areas

Many authors report the formation of well-defined ripples achieved by the dynamic irradiation of a copper target at IR wavelengths [2], [40], [50]. In the present work rippled areas were produced by raster scanning at the green wavelength. This technique consists in a bidirectional scanning of the laser beam along the horizontal (x) and vertical (y) directions, by moving the sample at velocity v_s. In this case a track of parallel lines along the x axis, with a shift Δ_y along the y axis, has been impressed onto the target. The sketch of the scanning path is illustrated in panel [a] of Fig. (5.1).
In the current experiment, several areas were textured by varying the scanning velocity v_s and the vertical step Δ_y. Panel [b] in Fig.(5.1) displays the Cu sample after the laser treatment. The laser was operated at $RR = 5\ kHz$, $\lambda = 515\ nm$ and $E \sim 180\ \mu J$ and the beam was focused onto the material surface by a cylindrical lens with a focal length of $150\ mm$.
Table (5.1) summarizes the values of v_s and Δ_y selected in order to produce twelve different areas. The surface morphology of the areas was analysed by means of the scanning electron microscope. In particular, in the current section we illustrate the SEM images that exemplify the upper edge of each irradiated zone. Considering the scanning path together with the 2D Gaussian spatial profile along the copper surface, we can hy-

pothesize that regions under investigations have been exposed to the less intense parts of the beam, i.e those corresponding to Gaussian tails.

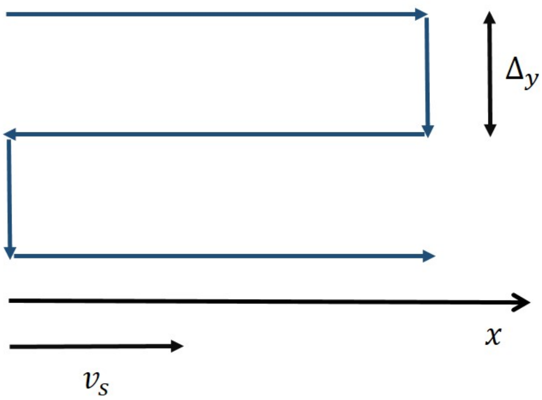

(a) Example of the scanning path in the raster scan method.

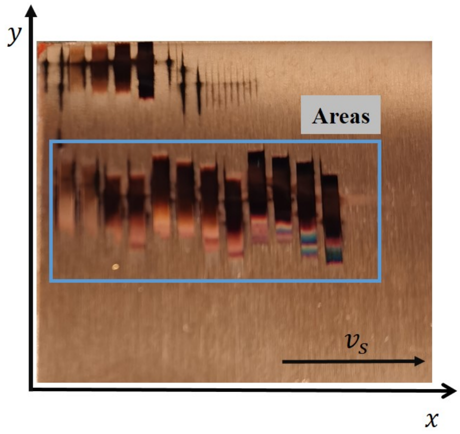

(b) Cu sample after the laser treatment carried out in this thesis work. The rectangular outline indicates the elaborated areas.

Figure 5.1: Femtosecond laser texturing of a copper target performed by raster scanning of the laser beam, focused with a cylindrical lens, on the surface.

In order to provide a clearer idea of the process, a picture of the spatial distribution of the laser intensity is illustrated in Fig. (5.2). In this frame, we do not take into account the influence of Δ_y since the zones under consideration are supposed to be not affected by the partial overlap between the Gaussian wings along the y direction.

Table 5.1: Values of the scanning speed v_s and the vertical shift Δ_y for each area elaborated at $\lambda = 515\ nm$, $RR = 5\ kHz$ and pulse energy $E = 180\ \mu J$.

	A_1	A_2	A_3	A_4	A_5	A_6	A_7	A_8	A_9	A_{10}	A_{11}	A_{12}
v_s(mm/s)	2	2	1	1	0.5	0.5	0.5	0.5	0.1	0.1	0.1	0.1
Δ_y (mm)	0.4	0.6	0.9	1.4	0.4	0.6	0.9	1.4	0.4	0.6	0.9	1.4

We turn now to introduce a typical parameter used to quantify the equivalent number of pulses in the case of the dynamic irradiation of the sample, namely $N_0 = (2\,w_0 RR)/v_s$, where w_0 is the laser spot size at the material surface [38].
Under the aforementioned hypothesis, we assume that w_0 is obtained by averaging the values $w_{0,x}$ reported in Tabs.(3.8) and (3.9) of Sect.(3.2). In this case w_0 is about $9.1\ \mu m$.

Hence, for each scanning velocity we calculated the number of overlapped pulses N_0 that are listed in Tab.(5.2).

Table 5.2: Number of overlapped pulses N_0 as function of the scanning velocity v_s.

$v_s(mm/s)$	N_0
2	45
1	90
0.5	182
0.1	910

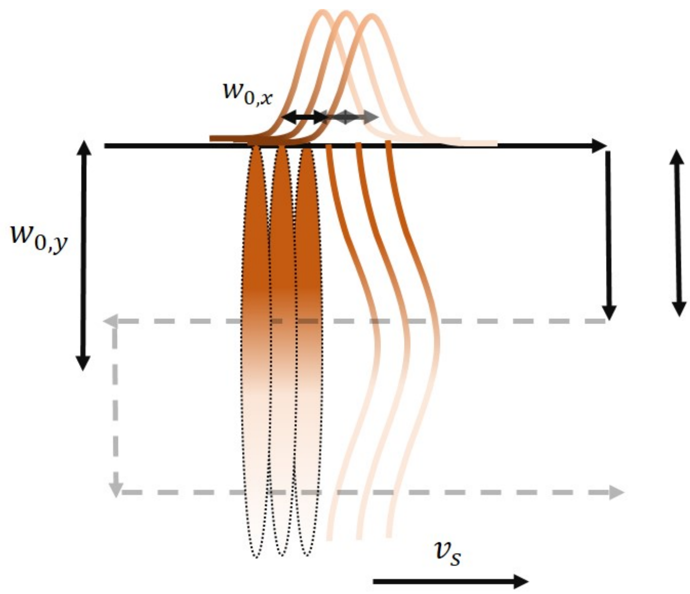

Figure 5.2: Sketch of the scanning path of the beam along the sample in combination with its spatial intensity profile.

Figure (5.3) illustrates the SEM micrographs that visualize copper rippled regions obtained by varying the scanning speeds and by fixing $\Delta_y = 0.4\,mm$. The panels show the formation of ripples aligned perpendicular to the laser beam polarization and decorated with nanoparticles back-deposited onto the sample due to the air confinement. From a qualitative point of view, the amount of nanoparticles increases with the reduction of the scanning velocity, i.e with the enhancement of the effective number of pulses. This result matches the literature, since many works report the dependence of back-deposited nanoparticles not only on the laser energy, as seen in Sect.(4.2), but also on the number of applied pulses onto the target [3], [43], [58]. In particular, the panels

[c] of Figs.(5.3) and (5.4) display agglomerates of nanoparticles, organized along the typical ripples periodic pattern, and obtained at $N_0 = 910$. The generation of ripples formed by aggregations of nanoparticles have been reported in several works [57], [58]. In particular, a study carried out on MeP-Si at low fluences shows that nanoparticles tend to align into periodic stripes as the number of pulses increases [57]. However, the mechanisms behind the formation of well ordered aggregates of nanoparticles are still being debated.

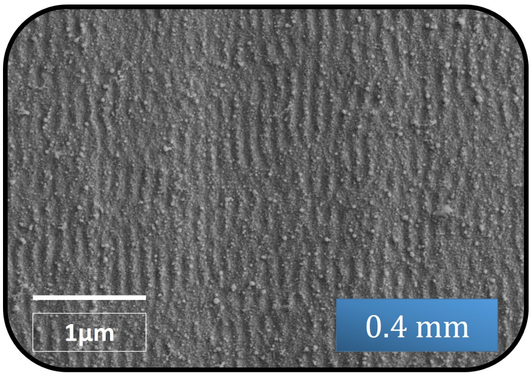

(a) $v_s = 2mm/s$.

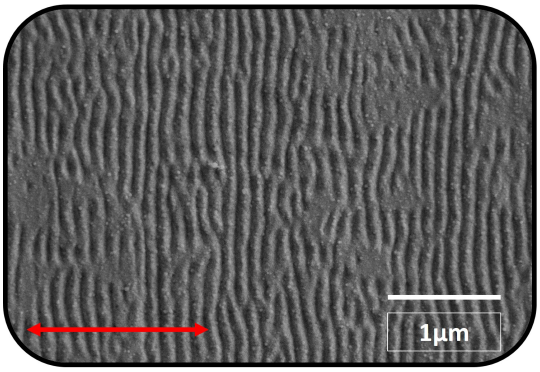

(b) $v_s = 0.5mm/s$.

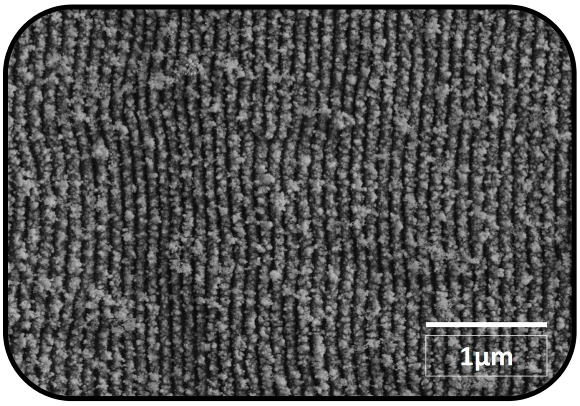

(c) $v_s = 0.1mm/s$.

Figure 5.3: SEM images of the upper edge of different areas processed at $\Delta_y = 0.4\ mm$. In each panel we signed up the scanning velocity v_s at which the Cu surface was elaborated. The double-headed arrow in panel [b] indicates the direction of the laser beam polarization. A spatial scale bar with a length of 1 μm is reported in each panel.

Since the goal of the present thesis is to produce well-defined periodic structures with less time-consuming approach, the reduction of the scanning velocity certainly constitutes a disadvantage. However, as it can be observed in Fig.(5.3), the generation of rippled areas gets improved as v_s decreases. Indeed, ripples formed at $v_s = 0.5\ mm/s$, and displayed in the right panel of Fig.(5.3), are deeper and more regular than those illustrated in the left panel. This effect is likely due to the Gaussian beam tails; in fact, since the tails represent the less intense parts of the beam, the laser fluence is not capable to induce substantial removal of material from the sample surface.

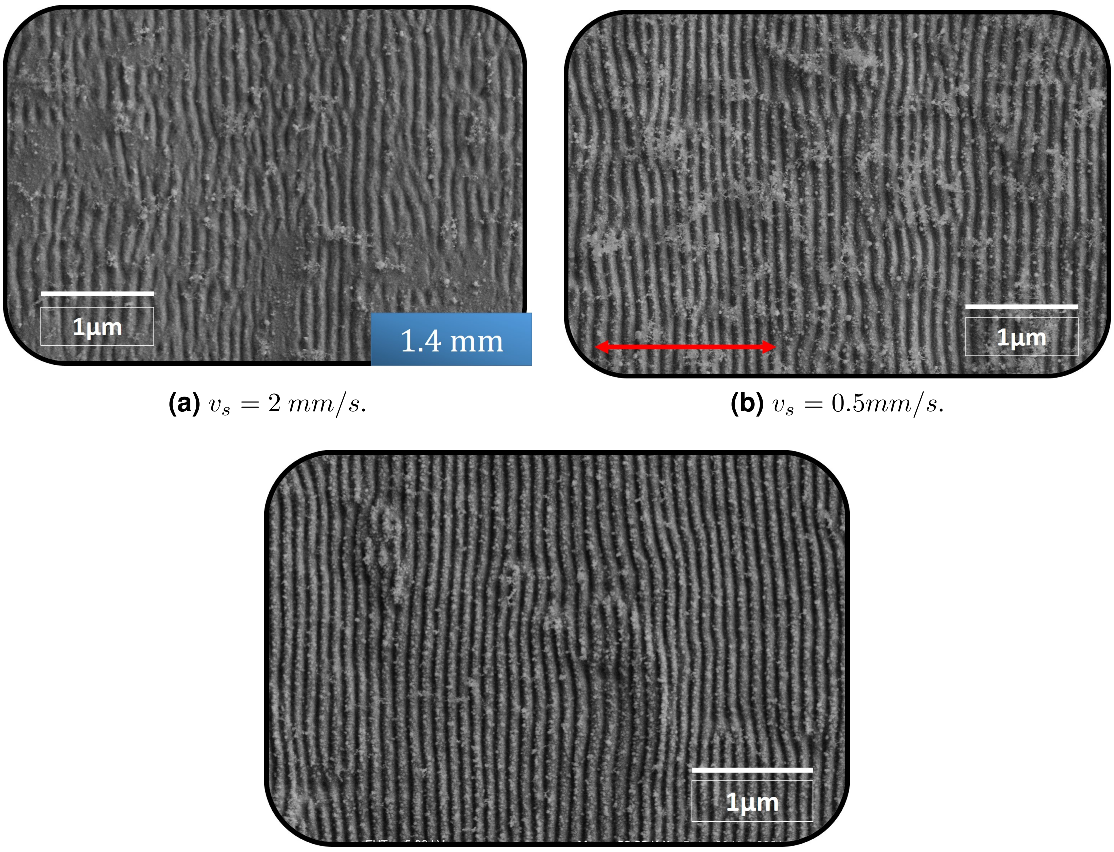

(a) $v_s = 2\ mm/s.$ **(b)** $v_s = 0.5mm/s.$

(c) $v_s = 0.1mm/s.$

Figure 5.4: SEM images of the upper edge of different areas processed at $\Delta_y = 1.4\ mm$. In each panel we signed up the scanning velocity v_s at which the Cu surface was elaborated. The double-headed arrow in panel [b] indicates the direction of the laser beam polarization. A spatial scale bar with a length of $1\ \mu m$ is reported in each panel.

Therefore, if the number of overlapped pulses is small, the resulting surface exhibits shallow ripples with a less defined pattern; whereas if N_0 increases the amount of material ablated is more consistent leading to the formation of well-defined ripples. Similar results are obtained in Ref. [40], where the authors investigated ripples formed on Cu at $N_0 = 200$ and $N_0 = 400$. The same description is suitable for the other structures elaborated at different Δ_y. An example is provided in Fig.(5.4), where ripples formed at $v_s = 2\ mm/s$ are shown to be less-defined with respect to those emerged at $v_s = 0.1\ mm/s$.

Another observation rising from a qualitative analysis of the SEM images is the influence of N_0 on the spatial period Λ of the ripples. Indeed, an increase of N_0 leads to a decrease of Λ. In order to investigate the periodic structures in more details, the bidimensional Fast Fourier transform (2D-FFT) maps of the SEM images were carried out. The 2D-FFT maps were elaborated by using Gwyddion software.

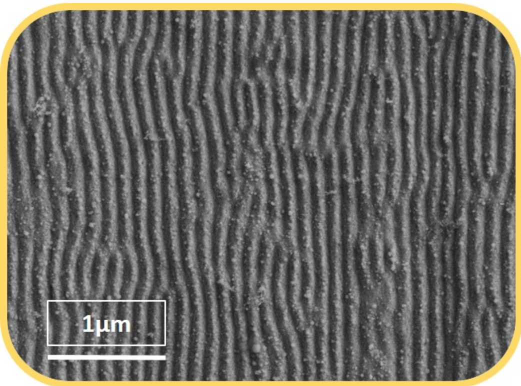

(a) Cu surface processed at $\Delta y = 0.6\ mm$ and $v_s = 0.5\ mm/s$.

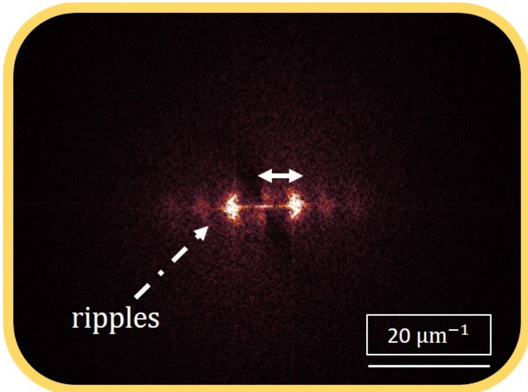

(b) 2D-FFT map of the SEM image of panel (a).

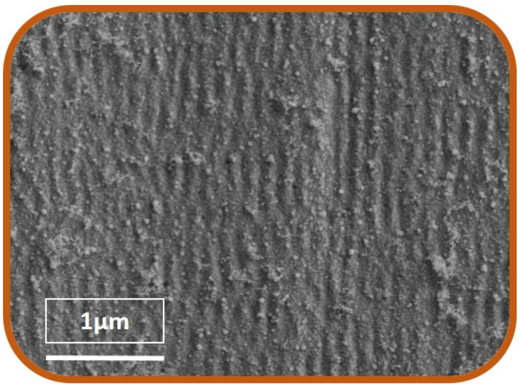

(c) Cu surface processed at $\Delta y = 0.6\ mm$ and $v_s = 2.0\ mm/s$.

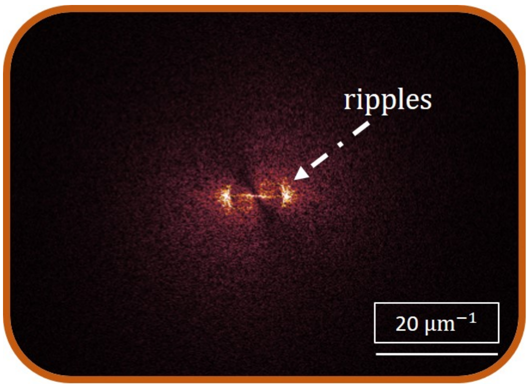

(d) 2D-FFT map of the SEM image of panel (c).

Figure 5.5: SEM views of the upper edge of the structured Cu surface with their 2D-FFT maps. The white double headed arrow in panel [b] indicates the measurement procedure.

Panels [b] and [d] of Figure (5.5) report the 2D-FFT maps of the panels [a] and [c], respectively. In both cases, it is possible to recognize a couple of intense peaks aligned along the direction of propagation of the periodic pattern in real space. These peaks are the spatial frequencies associated to ripples and allow to derive their the spatial period Λ. A sketch of the measurement procedure is provided in the panel [b] of Fig.(5.5). The measures in the Fourier space give an estimation of the spatial frequency $|\vec{k}|$ from which one can calculate Λ by using $\Lambda = 1/|\vec{k}|$.

The ripples spatial period was also measured by means of the spatial intensity profile elaborated with Image J software. The procedure is the same illustrated in Sect.(4.1). It is worth noticing that if the SEM images evidence a great amount of nanoparticles, the measure of Λ from the spatial intensity profile is not possible, because the presence of sparse nanoparticles compromises the spatial intensity distribution of the SEM image. This is the case of panel [c] of Fig.(5.3) that displays abundance of nanoparticles that leads to spatial intensity profile profiles as the one provided in Fig.(5.6), which does not show clear modulations to reliably recognize the ripples.

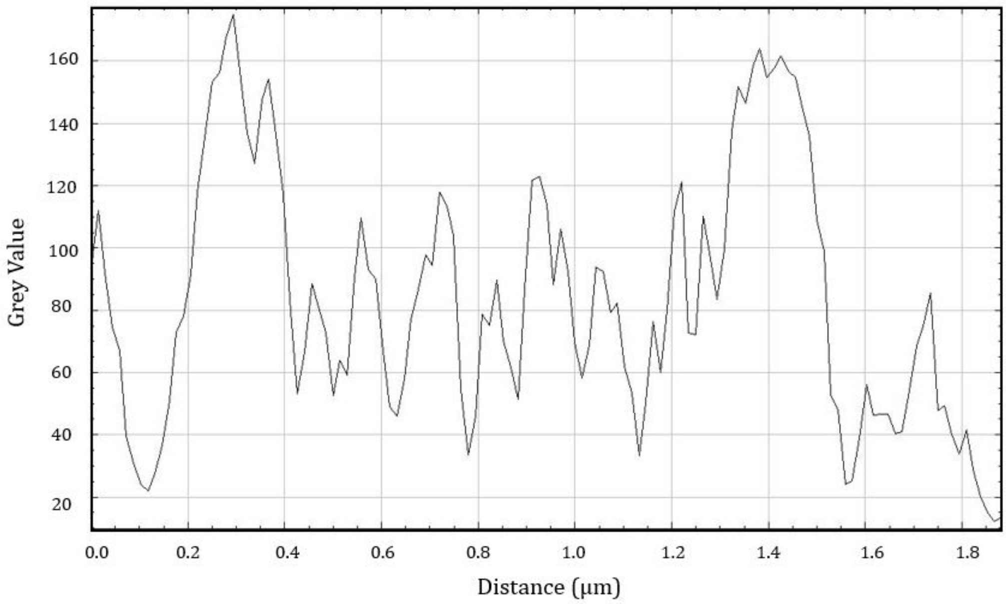

Figure 5.6: Example of a spatial intensity profile elaborated with Image J software associated to the SEM image of panel (c) in Fig.(5.3).

In such cases, in order to well visualize the presence of ripples and measure a reliable value of Λ, the 2D inverse FFT (2D-IFFT) is performed.
Panel [a] of Figure (5.7) reports the 2D FFT map of the SEM image of Fig.(5.3) [c]. The map displays two intense characteristic peaks linked to ripples, and a signal associated to a diffused distribution to the spreading of the spatial frequencies due to nanoparticles. Based on the panel [a] in Fig.(5.7), by using the filtering method offered by Gwyddion software, we obtained the 2D-IFFT maps of the zones corresponding to the intense coupled peaks and to the region surrounding them, respectively.

The former is illustrated in panel [b] of Fig.(5.7) and evidences the spatial distribution of nanoparticles in the real space.

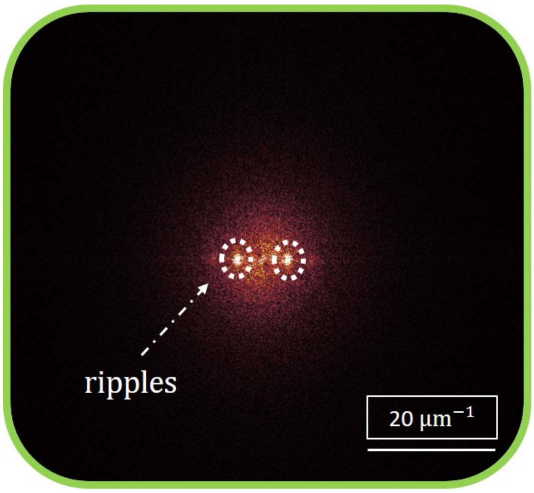

(a) 2D-FFT map of the SEM image of panel (c) in Fig.(5.3).

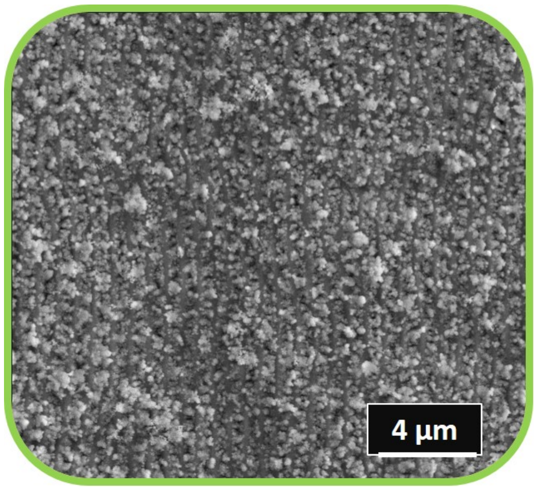

(b) 2D-IFFT map obtained from the difference between the signals in 2D-FFT map and the frequencies in the dashed circles of panel (a).

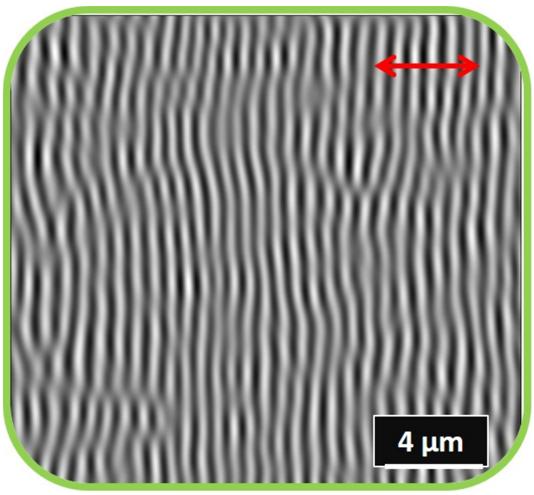

(c) 2D-IFFT map corresponding to the intense coupled peaks in the dashed circles of panel (a).

Figure 5.7: Example of 2D-IFFT maps in the case of an area fully covered by nanoparticles. The panel (b) evidences the distribution of nanoparticles in the real space, whereas the panel (c) shows the spatial modulation of ripples in the real space. The red arrow indicates the laser beam polarization.

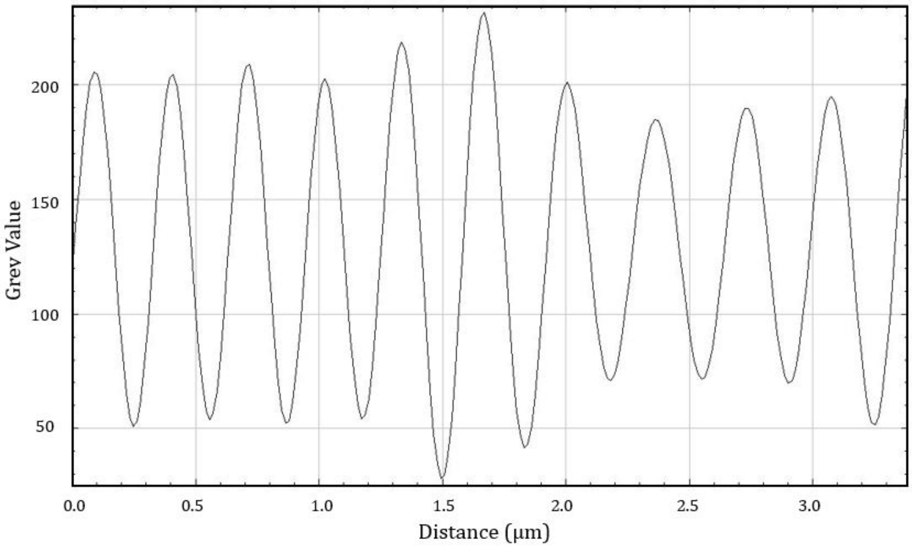

Figure 5.8: Spatial intensity profile elaborated with Image J software associated to the 2D-IFFT map of panel (c) in Fig. (5.7).

Table 5.3: Ripples spatial period calculated from the 2D-FFT maps, Λ_{FFT}, and from the intensity spatial profile $\Lambda_{profile}$.

Δ_y (mm)	v_s (mm/s)	Λ FFT (nm)	Λ profile(nm)
	2	365 ± 21	369 ± 45
0.4	0.5	346 ± 16	357 ± 34
	0.1	345 ± 13	331 ±27
	2	394 ± 30	388 ± 31
0.6	0.5	388 ± 29	380 ± 22
	0.1	336 ± 18	327 ± 37
	1	403 ± 41	406 ± 53
0.9	0.5	393 ± 17	382 ± 37
	0.1	344 ± 15	333 ± 26
	1	398 ± 26	393 ± 16
1.4	0.5	351 ± 17	366 ± 43
	0.1	324 ± 15	314 ± 39

The latter is displayed in panel [c] and shows the spatial modulation of the ripples in the real space as obtained by 2D-IFFT of filtered 2D-FFT maps. In this way it is possible to obtain a regular spatial intensity profile [Fig. (5.8)] from which an estimate of Λ can be obtained. Table (5.3) reports the values of Λ obtained from both the 2D-FFT images (Λ_{FFT}) and spatial intensity profiles analysis ($\Lambda_{profile}$).

The results gained from the two analyses are in agreement each other within the errors. Moreover, the data listed below show that a decrease of the scanning velocity v_s, namely an increase of N_0, results in a reduction of the spatial period of the ripples. Such an achievement is consistent with experimental findings reported in the literature both for the dynamic [40] and static irradiation conditions [9], [61]. These authors suggest that the decrease in the period of ripples may have different origins. One of the most acclaimed theory is that, pulse by pulse, the surface of the irradiated material changes its optical properties. This effect is supposed to be due to a mechanism of coupling between the incident laser beam and the grating formed by the first incoming pulses. As a consequence, the resonant wavelength of the SPP waves undergoes a shift that causes the reduction of the spatial period of the the interference pattern. Therefore, the modulation of the spatial energy distribution changes and gives rise to ripples with shorter periods [9], [22]. However, other mechanisms should not be ignored, such as the local variation of the angle of incidence in correspondence with the ablated zones or the accumulation of defects inside the material [9], [57].

Although there are not works about the direct laser surface processing of large areas over a Cu target at $\lambda = 515\ nm$, it can be stained that the values of Λ are reasonable since (i) those obtained at $N_0 = 182$ are in pretty good agreement with those observed in Sect.(4.1) at $N = 200$; (ii) exhibit a trend with the increase of the number of overlapped pulses similar to that observed in the case of the static irradiation of a metallic target.

5.2 Morphological features of the irradiated copper surface

In the current section, we deal with the structural modifications induced by the raster scanning of the beam on the Cu surface. In attempt to understand the rising of different structures, a sketch of the Gaussian spatial intensity profile along the scanning path is traced in Fig.(5.9).

In particular, we analyse several SEM images of the area indicated as A_{12} in Tab.(5.1). This region was elaborated at $v_s = 0.1\ mm/s$ and $\Delta_y = 1.4\ mm$. Considering that the Gaussian spot size along y direction is $\sim 2.7\ mm$, the picture in Fig.(5.9) becomes intelligible. In fact, since Δ_y is less than $w_{0,y}$, a superposition between the Gaussian spatial intensity profiles along the vertical direction can be expected. Note that the value of $w_{0,y}$ is obtained by averaging the data displayed in Tabs.(3.8) and (3.9) of Sect.(3.2).

In order to give a clearer idea of the structures produced during the laser treatment, we will try to follow the Gaussian spatial distribution of the laser intensity along the scanning path illustrated in Fig.(5.9).

We start from the first scanning line that moves from left to right. This trait identifies the zone where the less intense part of the beam is impressed on the target. In this case the surface is involved in mechanisms of interference that lead to the formation of ripples. Panel [a] in Fig.(5.10) is associated to this region indicated as (1). This SEM micrograph illustrates a wrinkled surface with well-defined ripples whose period Λ was evaluated from the 2D-FFT map displayed in panel [b]. Λ is found to be equal to $(324 \pm 15)\ nm$.

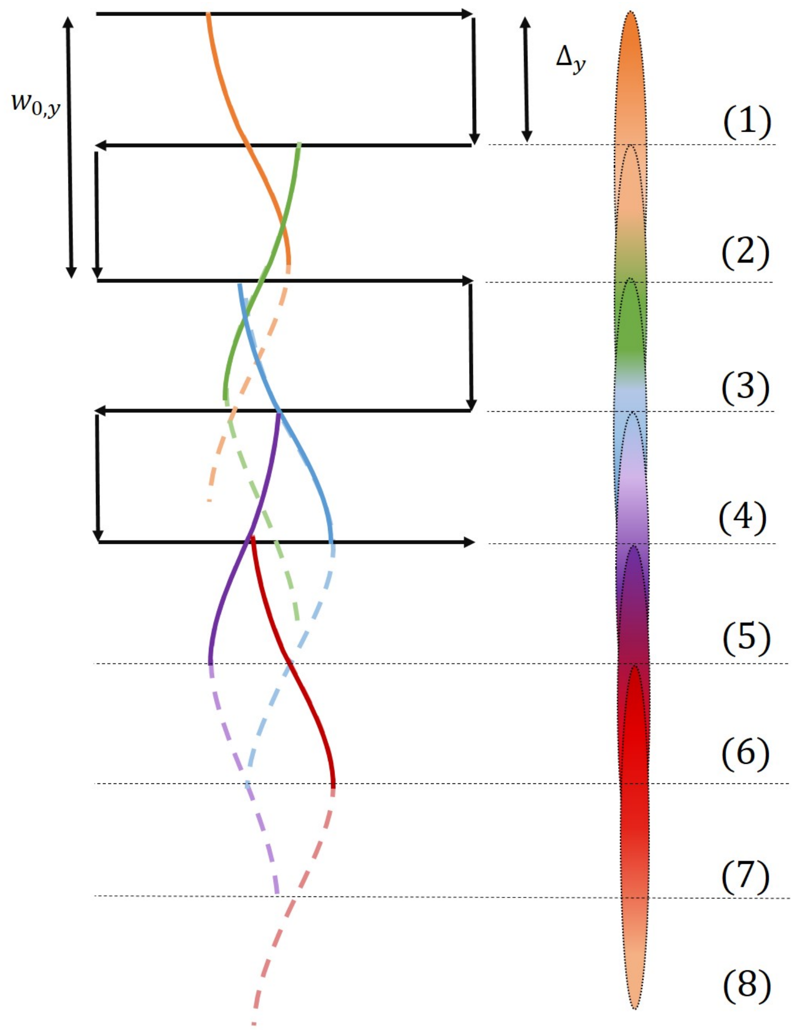

Figure 5.9: Sketch of the spatial distribution of the laser intensity during the laser treatment.

We now move down with a step $\Delta_y < w_{0,y}$ and consider the scanning line that starts from the right and goes towards the left. This line separates the zone (1) from the one marked as (2). The SEM view of panel [c] in Fig.(5.10) is relative to the zone (2) and features periodic structures composed by an assemblage of nanoparticles oriented perpendicular to the laser beam polarization. In this case the period of ripples, resulting from the measure carried out on the 2D-FFT map in panel [d], is about $(307 \pm 13)\ nm$. A possible explanation of the transition from well-defined ripples of the zone (1) to a well-ordered arrangement of nanoparticles of the zone (2) can rely on the superposition between the Gaussian spatial profiles. By moving the sample along the first line, the most intense part of the beam is impressed on zone (2) of the target causing the surface to eject some material and change its optical properties.

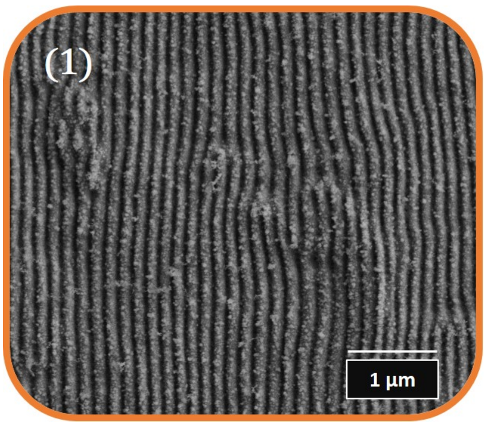

(a) SEM image exemplifying the upper edge of the copper surface.

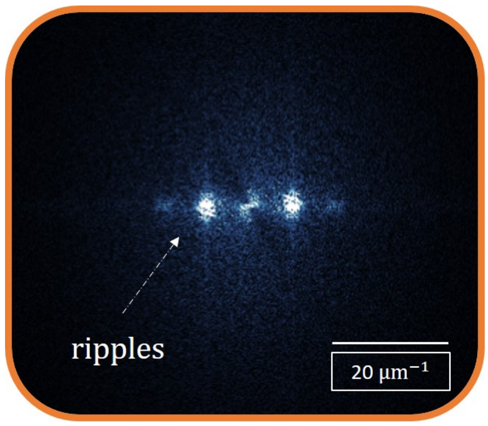

(b) 2D-FFT map of the SEM image of panel (a).

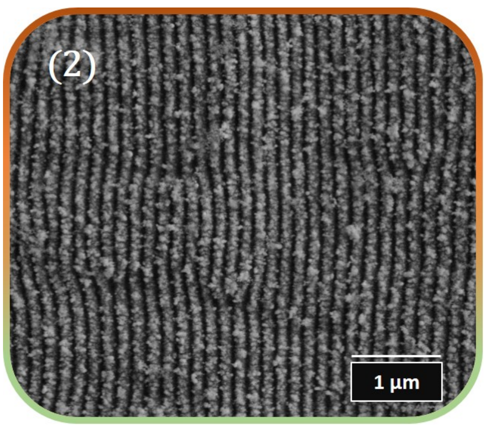

(c) SEM micrograph that identifies the surface structure below that illustrated in panel (a).

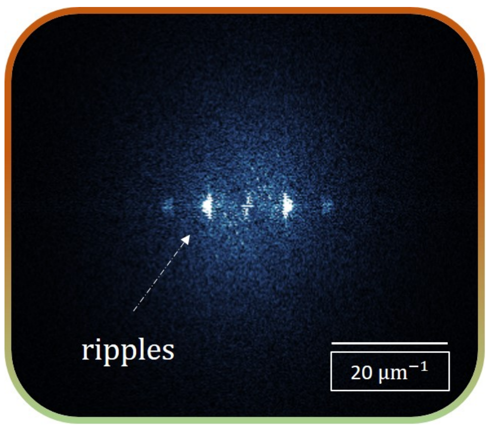

(d) 2D-FFT map of the SEM image of panel (c).

Figure 5.10: SEM images of the surface structures with their 2D-FFT maps. The panels (b) and (d) indicate the two bright peaks associated to ripples.

Subsequently, by moving the sample along the second scanning line, the zone (2) of the target is crossed by the Gaussian beam wings that influence the spatial arrangement of nanoparticles rising from the previous ablation. This effect is quite similar to that described in Sect.(5.1), where we studied the influence of the number N_0 of overlapped pulses on the structured Cu surface.

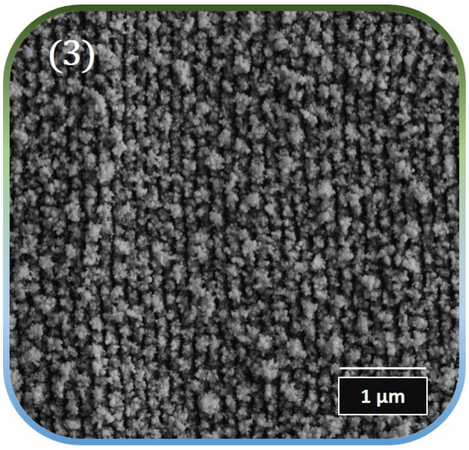

(a) Periodic structures fully covered by nanoparticles.

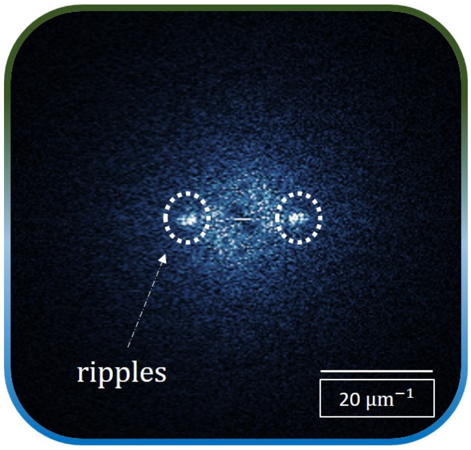

(b) 2D-FFT map of the SEM image of panel (a).

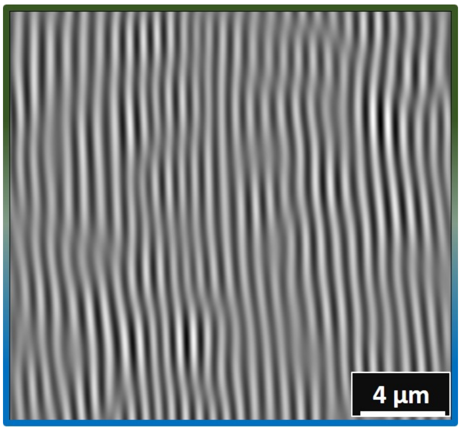

(c) 2D-IFFT map corresponding to the intense coupled peaks in the dashed circles of panel (b).

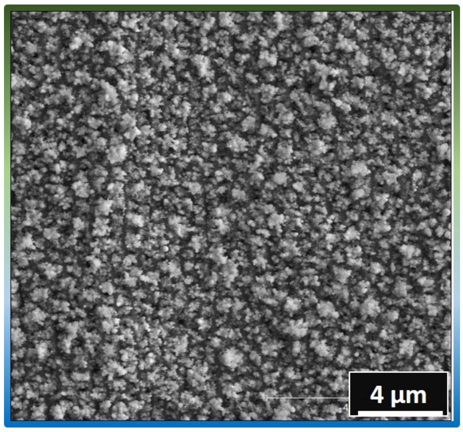

(d) 2D-IFFT map obtained from the difference between the signals of 2D-FF map and the frequencies in the dashed circles of panel (b).

Figure 5.11: SEM image of the structured Cu surface and its 2D-FFT (b) and filtered 2D-IFFT maps ((c) and (d)). The panel (b) evidences the presence of ripples together with the distribution of spatial frequencies associated to nanoparticles. Panels (c) and (d) show respectively the contribution of ripples and nanoparticles in the real space as obtained by 2D-IFFT of filtered maps of the 2D-FFT in panel (b).

In particular we found out that the spatial period Λ is getting reduced as N_0 increases. In this case a similar trend is observed, since the period of ripples in the case of the zone (2) is slightly smaller then the ripples spatial period linked to the zone (1). From this point of view, the presence of any feedback mechanisms in the region (2) is not all that unreasonable.

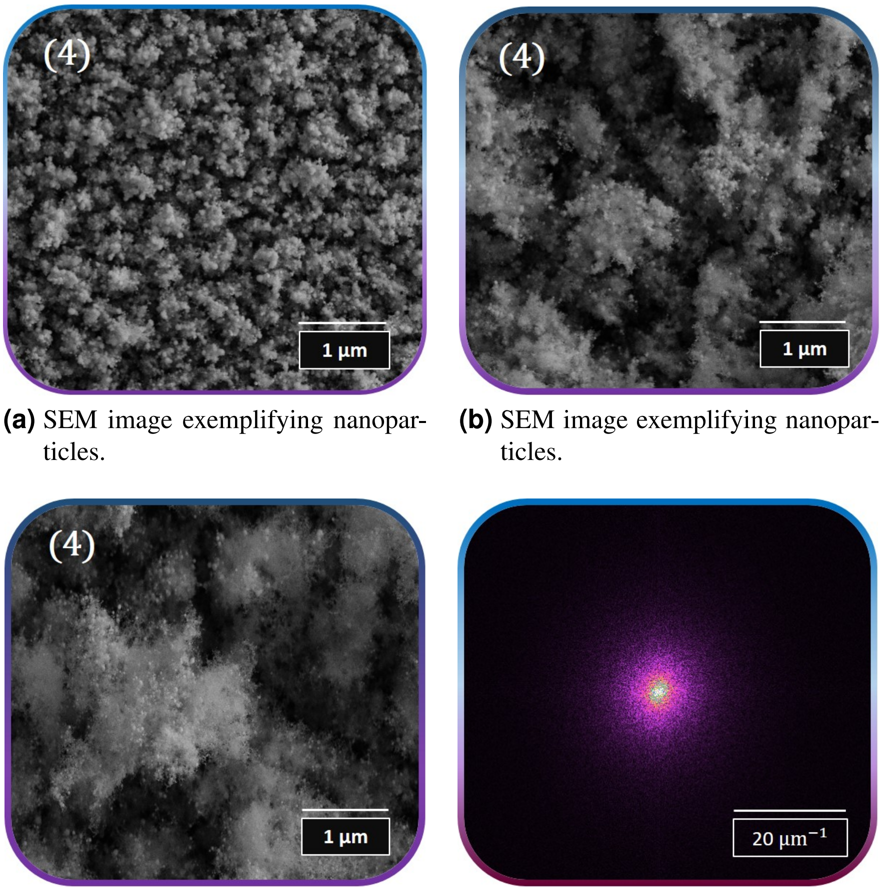

(a) SEM image exemplifying nanoparticles.

(b) SEM image exemplifying nanoparticles.

(c) SEM image exemplifying nanoparticles.

(d) 2D-FFT map of the SEM image of panel (c).

Figure 5.12: Panels [a]-[c] display the copper surface entirely covered by nanoparticles. Panel [d] exhibits the archetypal 2D-FFT for the regions fully of nanoparticles.

These observations can be applied for the other structures displayed in the beneath SEM images. In particular each micrograph is marked in the left upper corner with the number of the corresponding zone of the picture in Fig.(5.9). The SEM micrograph in Fig.(5.11) displays periodic structures entirely covered by nanoparticles that seem to assemble in periodic lines. The 2D-FFT map in the panel [b] show the two weak intensity peaks, surrounded by a distribution of spatial frequencies due to nanoparticles.

In order to associate the peaks to ripples, the 2D inverse FFT of the panel [a] was performed by filtering the two coupled spatial frequencies.

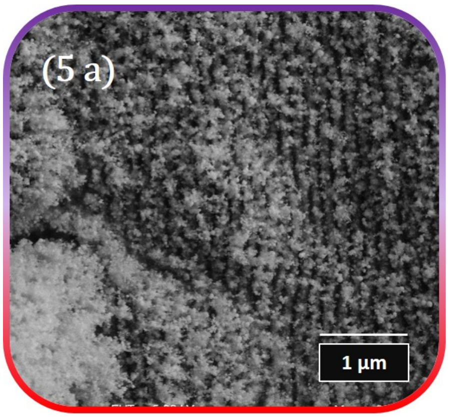

(a) Rippled area covered by noparticles deposits.

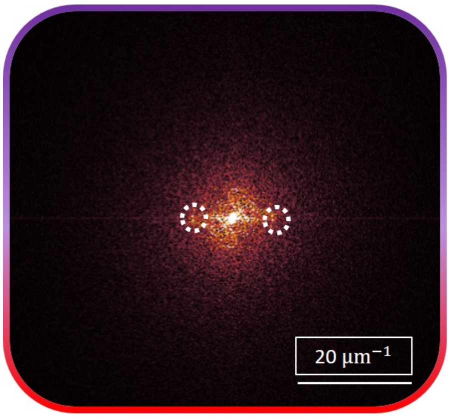

(b) 2D-FFT map of the SEM image in panel (a).

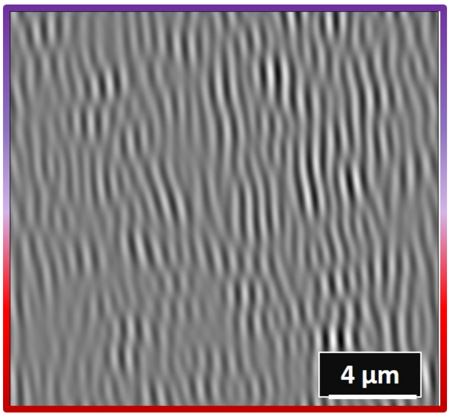

(c) 2D-IFFT map corresponding to the signals evidenced in the dashed circles of panel (b).

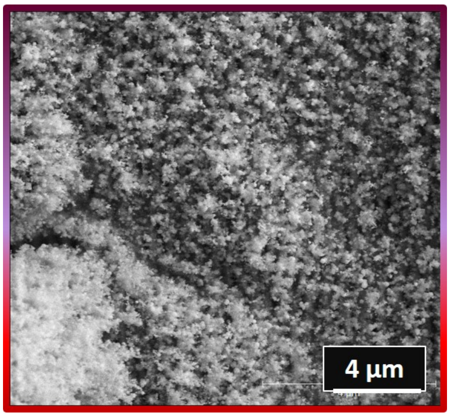

(d) 2D-IFFT map obtained from the difference between the signals in 2D-FFT map and the frequencies in the dashed circles of panel (b).

Figure 5.13: SEM image of copper surface with its 2D-FFT and 2D-IFFT maps. The panel [c] is inherent to the presence of ripples in the real space, whereas the panel [d] represents the contribution of nanoparticles.

The panel [c] of Fig.(5.11) reports the intensity spatial modulation of the periodic structures in the real space from which we measured Λ by using Image J software as in Sect.(5.1). The panel [d] evidences nanoparticles contribution in the real space. From this analysis the couples of peaks can be ascribed to ripples. Hence, the estimated value of ripples spatial period achieved from the 2D-FFT map is $(311 \pm\ 34)\ nm$, whereas the one evaluated from the intensity profile analysis is $(319 \pm 31)\ nm$. As expected, the two values are good in agreement with each other. Unlike the previous case, the SEM image under consideration visualise a larger amount of nanoparticles.

This could be due to the superposition between the Gaussian spatial profiles that in zone (3) is more pronounced than in zone (2). In particular, the more is the overlap between the Gaussian profiles of the laser beam along the direction perpendicular to the scanning direction, the more is the production of nanoparticles. This can be observed in panels ([a]-[c]) of Fig.(5.12) that report SEM images exemplifying nanoparticles randomly distributed over the surface of the target. The panel [d] is representative of the spectra obtained by the 2D-FFT of such images. The spread of the spatial frequencies in the map is inherent to the presence of nanoparticles and as expected it is not possible to recognize the couples of characteristic peaks linked to ripples. The formation of regular gratings appears again in the panel [a] of Fig.(5.13). The morphology suggests that this structure form as a consequence of a reduced superposition between the Gaussian intensity profiles. The 2D-FFT map in panel [b] displays two weak peaks inherent to periodic structures standing beneath the broad deposition of nanoparticles. The 2D-IFFT map in panel [c] confirms the presence of the ripples whose period is found to be $(310 \pm 11)\ nm$.

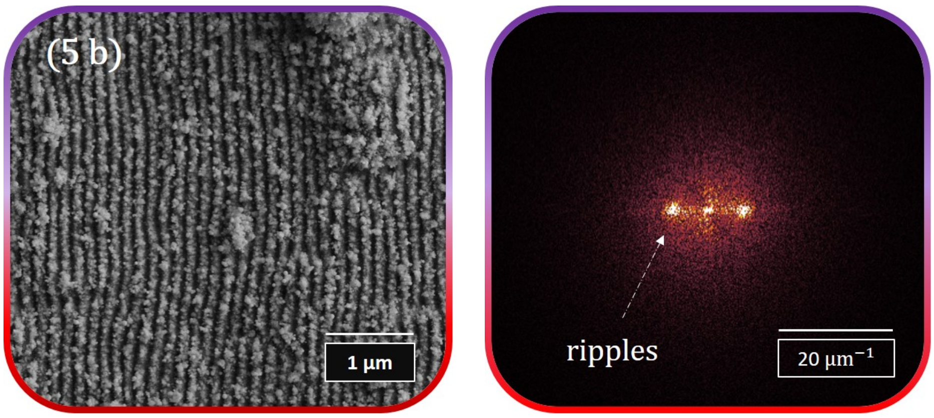

(a) Large area grating generated on copper and decorated by nanoparticles.

(b) 2D-FFT map of the SEM image of panel (a).

Figure 5.14: SEM image of the structured copper surface together with its 2D-FFT evidencing ripples.

The scanning electron micrograph marked as (5 b) in Fig.(5.14) shows the morphological features of the structure succeeding the one illustrated in panel [a] of Fig.(5.13). In this case the overlap between the Gaussian fluence distributions translates into a pattern of periodic trenches decorated by agglomerates of nanoparticles. The correspond-

ing 2D-FFT in Fig.(5.14) [b] reveals a period of $(300 \pm 18)\ nm$.
Moreover, the upper-right corner of panel [a] indicates the incoming of micro bumps formation, that is displayed in Fig.(5.15).

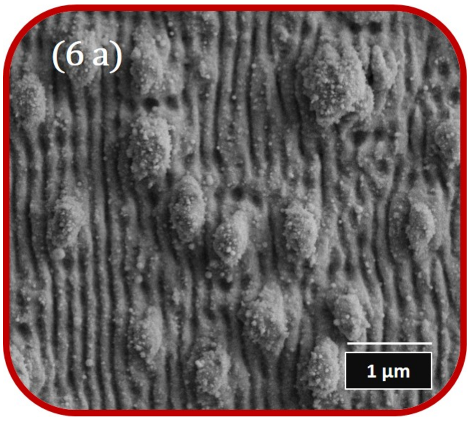

(a) Structured copper surface characterized by bumps and ripples.

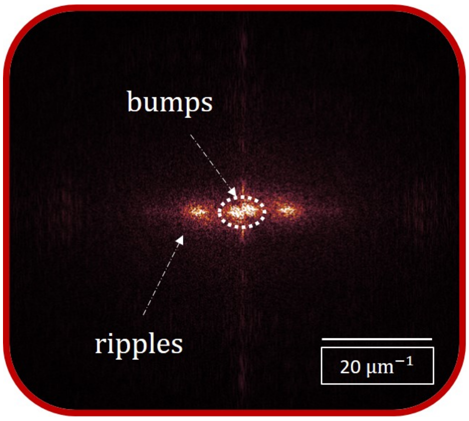

(b) 2D-FFT map of the SEM image of panel (a).

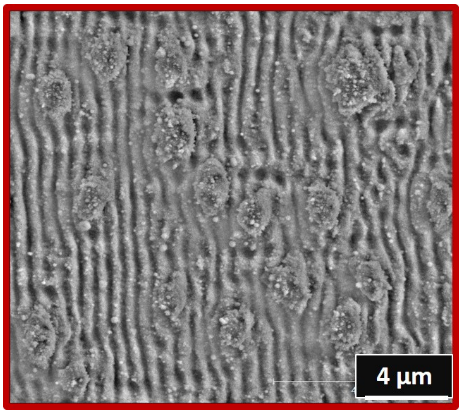

(c) 2D-IFFT map corresponding to the difference between the signals 2D-FFT map and the frequencies in the dashed circles in panel (b).

Figure 5.15: SEM micrograph exemplifying surface texture. Panel [b] indicates the presence of ripples and bumps. Panel [c] is inherent to ripples in the real space.

In fact, panel [a] in Fig.(5.15) features periodic structures interrupted by the growth of circular relief that dubbed bumps. The generation of bumps have been observed on several materials such as Ti, Al, steel, gold and copper [33], [35]. In particular, it has been shown that these structures can be replicated into a series of ordered arrays by exploiting interference between multiple beams [34]. However, the mechanism behind their formation is still controversial. Some authors suggest that bumps take their origin from plastic deformations caused by thermoelastic forces linked to the heating of the irradiated material. In particular, the stresses confine the hot material in a small portion of surface causing it to reach high temperatures and pressures that lead to a possible phase explosion and thus the formation of circular shaped bumps [44]. Others, instead, sustain that the development of bumps is linked to a fast cooling and redistribution of the molten material after the fs laser treatment [33]. Others possible explanations involve (i) the excitation of shock waves due to the plasma plume located above the material, (ii) and the Marangoni effect [33], [44].

Panel [b] of Fig.(5.15) reports the 2D-FFT map of the SEM image in panel [a] from which we estimated $\Lambda = (340 \pm 16)\ nm$ in agreement with that evaluated from the intensity profile analysis. Moreover, the map identifies two bright spatial frequencies that seem to be associated to bumps. In order to ascertain this correspondence, the 2D-IFFT map was carried out by filtering the spatial frequencies in the center of the picture. The result of this procedure, illustrated in panel [c], confirms our hypothesis since the figure replicates the surface structure in panel [a] without bumps.
The SEM micrograph in Fig.(5.16) displays the evolution of bumps into periodic straight lines that seem to result from a fast solidification of the irradiated zone. The 2D-FFT map in the panel [c] of Fig.(5.16) displays the characteristic intensity peaks associated to ripples, from which we measured $(\Lambda = 379 \pm 45)\ nm$ in agreement with the value $(385 \pm 32)\ nm$ achieved from the spatial intensity profile. Note that these values of the ripples spatial period are the highest of all find out in this frame.

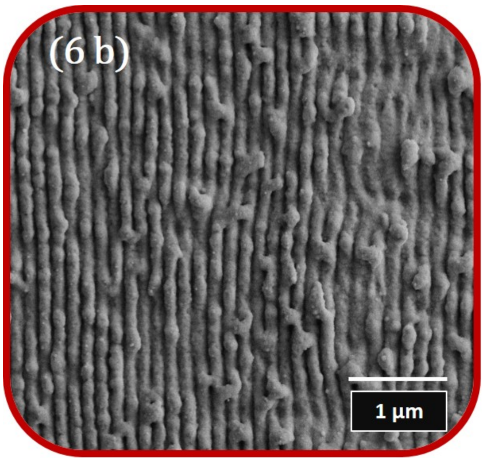

(a) Rippled area resulting from the solidification of the irradiated structure.

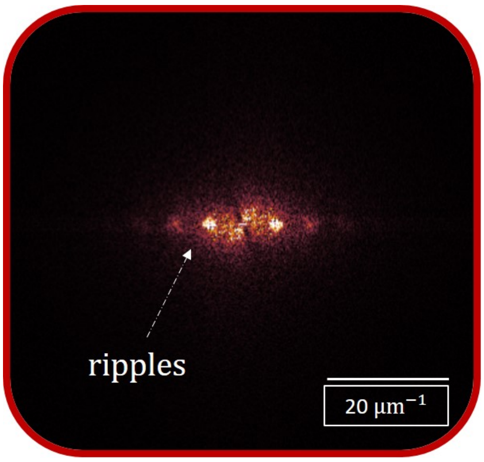

(b) 2D-FFT map of the SEM image of panel (a).

Figure 5.16: SEM image of the surface structures and its 2D-FFT maps.

We now pay our attention to the last two structures marked as (7) and (8) in Fig.(5.17).

According to the picture in Fig.(5.9), the former rippled area emerges as consequence of an overwriting that occurs in the same way described for the zone (2), whereas the latter forms in the same way of the zone (1).

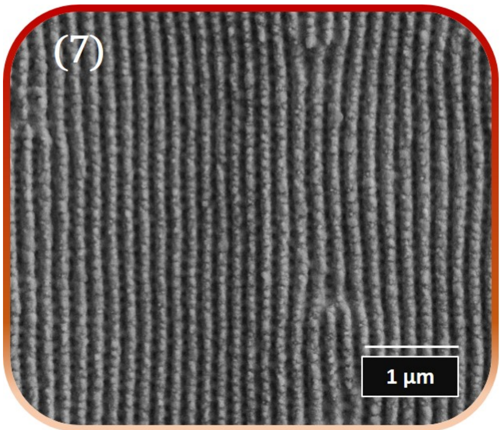

(a) SEM image exemplifying the upper edge of the copper surface.

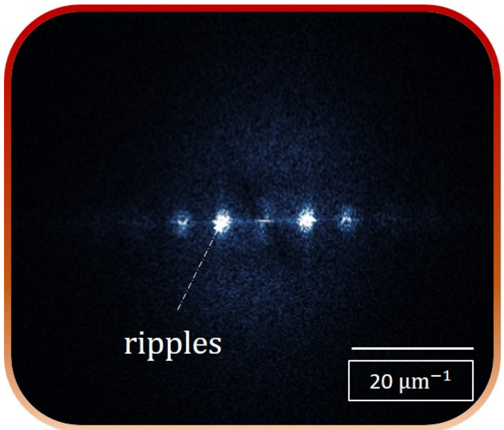

(b) 2D-FFT map of the SEM image of panel (a).

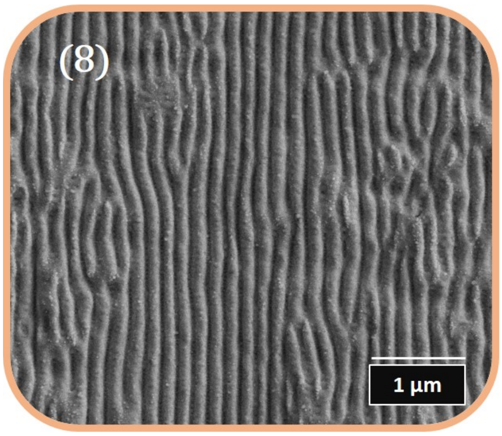

(c) SEM micrograph that identifies the surface structure below that illustrated in panel (a).

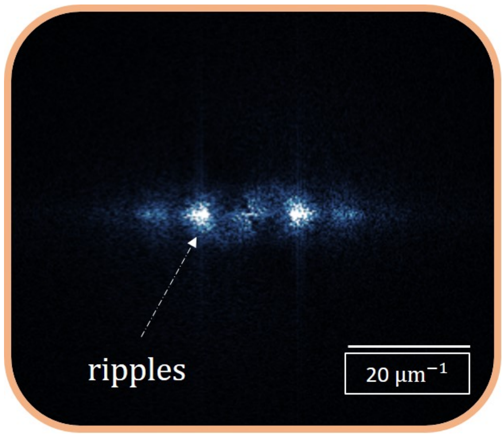

(d) 2D-FFT map of the SEM image of panel (c).

Figure 5.17: SEM images of the surface structures with their 2D-FFT maps. Panels (b) and (d) indicate the presence of ripples.

From the 2D-FFT maps, we evaluated the ripples spatial period Λ of the two SEM images under investigation. The estimated values are $(311 \pm 20)\ nm$ for the picture [a] and $(335 \pm 31)\ nm$ for the picture [c]. Note that the ripples period inherent to the zone (7) is consistent with the one estimated in the zone (2) and smaller with respect to the period obtained for the zone (8) that, in turn, is in agreement with that derived for the zone (1). These results suggest that (i) the mechanism behind the formation of the wrinkled structure associated to the zone (7) is similar to that associated to the zone (2) as well as for the zone (1) and (8); (ii) the regions which feature smaller ripples periods are probably involved in some feedback mechanisms similar to those that induce their reduction as number of applied pulses increases.

The description of the formation behind the surface structures provided in this section is only one of those possible. Therefore, further investigation are required in order to (i) develop clearer sub-wavelength structures by the raster scan method (ii) understand the mechanisms of formation of hierarchical structures on copper. Moreover, to the best of our knowledge, few works on the elaboration of large areas by means of a fs laser source focused with a cylindrical lens have been carried out. Some studies were carried out on steel [4], Ti O_2 [17] and silicon [52]. However, further investigations on the effects of the cylindrical lens in combination with direct femtosecond laser processing is required, since this method allows to rapidly produce nano-structures over large zones.

Conclusions

In this thesis work fs laser surface texturing of a Cu sample is carried out. The work offers a complete overview of the induced surface structures on copper with a Yb:KGW laser source providing laser pulses with a duration of $\sim 180\ fs$ at a central wavelength of $1030\ nm$ and a second harmonic output of $515\ nm$.
Chapter (1) and Chapter (2) are respectively devoted to the fs laser ablation process with a particular emphasis on the mechanisms underlying the LIPSS formation and the experimental setup used for the direct fs laser surface processing. Additionally, Chap.(2) contains: (i) a general outlook on the spherical and cylindrical lenses, evidencing the role of the cylindrical lens in the frame of this work, (ii) the description of the optical and the scanning electron microscope used to analyse the morphological features of the surface structures.
The surface structures have been produced with both static and dynamic irradiation of the copper target. By irradiating the sample in static condition, circular craters with a spherical lens and elliptical craters with a cylindrical lens were generated; whereas by the raster scanning of the beam along the target surface (dynamic configuration) millimeter size areas were elaborated. The former technique is usually preliminary to the second since, by exploiting the Gaussian beam model, it allows to measure two important parameters: the threshold fluence and the spot size of the laser beam. This experimental procedure is presented in Chapter (3) and it results conventional for laser beams focused with a spherical lens. However, in this work we proved that it is suitable also for laser beams focused with a cylindrical lens.
The thresholds fluence for copper ablation are found to be dissimilar at the laser wavelengths of $\lambda = 1030\ nm$ and $\lambda = 515\ nm$. This is expected since this parameter depends not only on the specific material, but also on the laser wavelength. In this context, the study of the influence of laser pulse repetition rate on the surface structures is provided; in particular, our experimental findings show that the Cu surface topography is not affected by repetition rates in the range of kHz in our experimental conditions.
Since the interest is to explore the surface structures generated by employing the cylindrical lens, Chapter (4) is devoted to the description of the morphological features of the elliptical craters produced on the Cu target in static configuration. In particular, the induced surface structures exhibit different morphologies due to the local fluence value

impinged on the material during the irradiation process. In the peripheral area ripples with a period $\Lambda = 950\ nm$ (at $\lambda = 1030\ nm$) and $\Lambda = 346\ nm$ (at $\lambda = 515\ nm$) appear. These ripple periodicity evidence the presence of the feedback mechanism linked to the number of laser pulses. The chapter illustrates also the dynamics of nanoparticles distribution. The nanoparticles debris deposits onto the copper substrate as a consequence of the plasma plume cooling; in particular, our experimental findings evidence that distribution of the nanoparticles around the shallow crater is different when using the spherical and cylindrical lenses. In order to explain this experimental observation, further studies are necessary since such phenomenon has been evidenced here for the first time and there are not yet models of the nanoparticle plume propagation dynamics in air at atmospheric pressure after ablation with a cylindrical lens and even the one generated by using a spherical lens is far to be completely addressed.

Finally, in fifth Chapter deals with the morphological features of the target surface elaborated by using the cylindrical lens to texture larger areas. In particular, we analysed the influence of the scanning velocity, i.e the effective number of pulses, on the rippled periodicity and it was found that Λ decreases with N, in agreement with the expected behaviour. Moreover, the chapter contains the description of surface structures emerging in the region processed by a single beam passage, at the periphery of the produced large areas, that develop well defined ripples and the features observed where more beam overlap occurs. In this second case, our analysis evidences that the effects of the superposition between the Gaussian beam intensity profiles pertaining to each laser beam passage during the rastering process. In particular, when the overlap is too high on the irradiated surface a great amount of nanoparticles appear. All the obtained results provide a clear picture of the various effects coming into play during large area structuring with elliptical beams and lay the foundation to investigate the best experimental conditions in order to form well defined ripples on copper.

Bibliography

[1] E Allahyari, J JJ Nivas, M Valadan, R Fittipaldi, A Vecchione, L Parlato, R Bruzzese, C Altucci, and S Amoruso. Plume shielding effects in ultrafast laser surface texturing of silicon at high repetition rate in air. *Applied Surface Science*, 488:128–133, 2019.

[2] Elaheh Allahyari, Jijil JJ Nivas, Stefano L Oscurato, Marcella Salvatore, Giovanni Ausanio, Antonio Vecchione, Rosalba Fittipaldi, Pasqualino Maddalena, Riccardo Bruzzese, and Salvatore Amoruso. Laser surface texturing of copper and variation of the wetting response with the laser pulse fluence. *Applied Surface Science*, 470:817–824, 2019.

[3] JC Alonso, R Diamant, P Castillo, MC Acosta-García, N Batina, and E Haro-Poniatowski. Thin films of silver nanoparticles deposited in vacuum by pulsed laser ablation using a yag: Nd laser. *Applied Surface Science*, 255(9):4933–4937, 2009.

[4] Marcus Ardron, Nick Weston, and Duncan Hand. A practical technique for the generation of highly uniform lipss. *Applied surface science*, 313:123–131, 2014.

[5] Milton Birnbaum. Semiconductor surface damage produced by ruby lasers. *Journal of Applied Physics*, 36(11):3688–3689, 1965.

[6] Jörn Bonse. Quo vadis lipss?—recent and future trends on laser-induced periodic surface structures. *Nanomaterials*, 10(10):1950, 2020.

[7] Jörn Bonse and Stephan Gräf. Maxwell meets marangoni—a review of theories on laser-induced periodic surface structures. *Laser & Photonics Reviews*, 14(10):2000215, 2020.

[8] Jörn Bonse, Sandra Höhm, Sabrina V Kirner, Arkadi Rosenfeld, and Jörg Krüger. Laser-induced periodic surface structures—a scientific evergreen. *IEEE Journal of selected topics in quantum electronics*, 23(3), 2016.

[9] Jörn Bonse and Jörg Krüger. Pulse number dependence of laser-induced periodic surface structures for femtosecond laser irradiation of silicon. *Journal of Applied Physics*, 108(3):034903, 2010.

[10] Jörn Bonse, Jörg Krüger, S Höhm, and A Rosenfeld. Femtosecond laser-induced periodic surface structures. *Journal of Laser Applications*, 24(4):042006, 2012.

[11] Jörn Bonse, Martin Munz, and Heinz Sturm. Structure formation on the surface of indium phosphide irradiated by femtosecond laser pulses. *Journal of Applied Physics*, 97(1):013538, 2005.

[12] Jörn Bonse, Sabrina V. Kirner, Sandra Höhm, Nadja Epperlein, Dirk Spaltmann, Arkadi Rosenfeld, and Jörg Krüger. Applications of laser-induced periodic surface structures (LIPSS). In Udo Klotzbach, Kunihiko Washio, and Rainer Kling, editors, *Laser-based Micro- and Nanoprocessing XI*, volume 10092, pages 114 – 122. International Society for Optics and Photonics, SPIE, 2017.

[13] Jeppe Byskov-Nielsen, Juha-Matti Savolainen, Martin Snogdahl Christensen, and Peter Balling. Ultra-short pulse laser ablation of metals: threshold fluence, incubation coefficient and ablation rates. *Applied Physics A*, 101(1):97–101, 2010.

[14] Sergio Calatroni, Elisa Garcia-Tabares Valdivieso, Ana Teresa Perez Fontenla, Mauro Taborelli, Holger Neupert, Marcel Himmerlich, Paolo Chiggiato, David Bajek, Stefan Wackerow, and Amin Abdolvand. Optimization of the secondary electron yield of laser-structured copper surfaces at room and cryogenic temperature. *Physical Review Accelerators and Beams*, 23(3):033101, 2020.

[15] Sergio Calatroni, Elisa Garcia-Tabares Valdivieso, Holger Neupert, Valentin Nistor, Ana Teresa Perez Fontenla, Mauro Taborelli, Paolo Chiggiato, Oleg Malyshev, Reza Valizadeh, Stefan Wackerow, et al. First accelerator test of vacuum components with laser-engineered surfaces for electron-cloud mitigation. *Physical Review Accelerators and Beams*, 20(11):113201, 2017.

[16] JK Chen and JE Beraun. Modelling of ultrashort laser ablation of gold films in vacuum. *Journal of Optics A: Pure and Applied Optics*, 5(3):168, 2003.

[17] Susanta Kumar Das, Kiran Dasari, Arkadi Rosenfeld, and Ruediger Grunwald. Extended-area nanostructuring of tio2 with femtosecond laser pulses at 400 nm using a line focus. *Nanotechnology*, 21(15):155302, 2010.

[18] Iaroslav Gnilitskyi, Thibault J-Y Derrien, Yoann Levy, Nadezhda M Bulgakova, Tomáš Mocek, and Leonardo Orazi. High-speed manufacturing of highly regular femtosecond laser-induced periodic surface structures: physical origin of regularity. *Scientific reports*, 7(1):1–11, 2017.

[19] Shutong He, Jijil JJ Nivas, KK Anoop, Antonio Vecchione, Minglie Hu, Riccardo Bruzzese, and Salvatore Amoruso. Surface structures induced by ultrashort laser pulses: Formation mechanisms of ripples and grooves. *Applied Surface Science*, 353:1214–1222, 2015.

[20] Shutong He, Jijil JJ Nivas, Antonio Vecchione, Minglie Hu, and Salvatore Amoruso. On the generation of grooves on crystalline silicon irradiated by femtosecond laser pulses. *Optics express*, 24(4):3238–3247, 2016.

[21] https://www.zeiss.com/microscopy/us/products.html. Zeiss sigma field emission electron microscope.

[22] Min Huang, Fuli Zhao, Ya Cheng, Ningsheng Xu, and Zhizhan Xu. Origin of laser-induced near-subwavelength ripples: interference between surface plasmons and incident laser. *ACS nano*, 3(12):4062–4070, 2009.

[23] SE v Kirkwood, AC Van Popta, YY Tsui, and R Fedosejevs. Single and multiple shot near-infrared femtosecond laser pulse ablation thresholds of copper. *Applied Physics A*, 81(4):729–735, 2005.

[24] Yang Leng. *Materials characterization: introduction to microscopic and spectroscopic methods*. John Wiley & Sons, 2009.

[25] JM Liu. Simple technique for measurements of pulsed gaussian-beam spot sizes. *Optics letters*, 7(5):196–198, 1982.

[26] Yi-Hsien Liu and Chung-Wei Cheng. Green wavelength femtosecond laser ablated copper surface. *Optics Communications*, page 127875, 2021.

[27] Yi-Hsien Liu, Kong-Kai Kuo, and Chung-Wei Cheng. Femtosecond laser-induced periodic surface structures on different tilted metal surfaces. *Nanomaterials*, 10(12):2540, 2020.

[28] Thomas Lucatorto, Marc De Graef, Richard F Haglund, and John C Miller. *Laser ablation and desorption*. Academic Press, 1997.

[29] Charles E Lyman, Dale E Newbury, Joseph Goldstein, Alton D Romig Jr, John Armstrong, Patrick Echlin, David B Williams, David C Joy, Charles Fiori, Eric Lifshin, et al. *Scanning electron microscopy, X-ray microanalysis, and analytical electron microscopy: a laboratory workbook*. Springer Science & Business Media, 1990.

[30] M Malinauskas, A Žukauskas, S Hasegawa, Y Hayasaki, V Mizeikis, R Buividas, and S Juodkazis. Light: Sci. appl. 5, e16133 (2016), 2016.

[31] Ion N Mihailescu and Anna Paola Caricato. Pulsed laser ablation: Advances and applications in nanoparticles and nanostructuring thin films. 2018.

[32] Douglas B Murphy. *Fundamentals of light microscopy and electronic imaging*. John Wiley & Sons, 2002.

[33] Aida Naghilou, Miao He, Jasmin S Schubert, Leonid V Zhigilei, and Wolfgang Kautek. Femtosecond laser generation of microbumps and nanojets on single and bilayer cu/ag thin films. *Physical Chemistry Chemical Physics*, 21(22):11846–11860, 2019.

[34] Yoshiki Nakata, Tatsuo Okada, and Mitsuo Maeda. Nano-sized hollow bump array generated by single femtosecond laser pulse. *Japanese Journal of Applied Physics*, 42(12A):L1452, 2003.

[35] Barada K Nayak and Mool C Gupta. Self-organized micro/nano structures in metal surfaces by ultrafast laser irradiation. *Optics and Lasers in Engineering*, 48(10):940–949, 2010.

[36] David Nečas and Petr Klapetek. Gwyddion: an open-source software for SPM data analysis. *Central European Journal of Physics, http://gwyddion.net/*, 10:181–188, 2012.

[37] WS Rasband (NIH). Imagej. *https://imagej.nih.gov/ij/*, 2016.

[38] Jijil JJ Nivas and Salvatore Amoruso. Generation of supra-wavelength grooves in femtosecond laser surface structuring of silicon. *Nanomaterials*, 11(1):174, 2021.

[39] Jijil JJ Nivas, Shutong He, Andrea Rubano, Antonio Vecchione, Domenico Paparo, Lorenzo Marrucci, Riccardo Bruzzese, and Salvatore Amoruso. Direct femtosecond laser surface structuring with optical vortex beams generated by a q-plate. *Scientific reports*, 5(1):1–12, 2015.

[40] JJJ Nivas, M Valadan, M Salvatore, R Fittipaldi, M Himmerlich, M Rimoldi, A Passarelli, E Allahyari, SL Oscurato, A Vecchione, et al. Secondary electron yield reduction by femtosecond pulse laser-induced periodic surface structuring. *Surfaces and Interfaces*, 25:101179, 2021.

[41] Zhigui Ou, Min Huang, and Fuli Zhao. Colorizing pure copper surface by ultrafast laser-induced near-subwavelength ripples. *Optics express*, 22(14):17254–17265, 2014.

[42] Dr. Rüdiger Paschotta. Rp photonics consulting gmbh, waldstr. 17, 78073 bad dürrheim, germany, https://www.rp-photonics.com/.

[43] M Quintana, E Haro-Poniatowski, J Morales, and N Batina. Synthesis of selenium nanoparticles by pulsed laser ablation. *Applied surface science*, 195(1-4):175–186, 2002.

[44] M Shahid Rafique, Shazia Bashir, Ali Ajami, and Wolfgang Husinsky. Nonlinear absorption properties correlated with the surface and structural changes of ultra short pulse laser irradiated cr-39. *Applied Physics A*, 100(4):1183–1189, 2010.

[45] RefractiveIndex.INFO. https://refractiveindex.info/shelf=mainbook=cupage=babar.

[46] RefractiveIndex.INFO. https://refractiveindex.info/shelf=mainbook=cupage=johnson.

[47] RefractiveIndex.INFO. https://refractiveindex.info/shelf=mainbook=sipage=aspnes.

[48] Claude Rulliere et al. *Femtosecond laser pulses*. Springer, 2005.

[49] X Sedao, M Lenci, Anton Rudenko, N Faure, A Pascale-Hamri, Jean-Philippe Colombier, and C Mauclair. Influence of pulse repetition rate on morphology and material removal rate of ultrafast laser ablated metallic surfaces. *Optics and Lasers in Engineering*, 116:68–74, 2019.

[50] Vidhya Selvamani, Amin Zareei, Ahmed Elkashif, Murali Kannan Maruthamuthu, Shirisha Chittiboyina, Davide Delisi, Zheng Li, Lirong Cai, Vilas G Pol, Mohamed N Seleem, et al. Hierarchical micro/mesoporous copper structure with enhanced antimicrobial property via laser surface texturing. *Advanced Materials Interfaces*, 7(7):1901890, 2020.

[51] NG Semaltianos, W Perrie, V Vishnyakov, R Murray, CJ Williams, SP Edwardson, G Dearden, P French, M Sharp, S Logothetidis, et al. Nanoparticle formation by the debris produced by femtosecond laser ablation of silicon in ambient air. *Materials Letters*, 62(14):2165–2170, 2008.

[52] Mehra S Sidhu, Pooja Munjal, and Kamal P Singh. High-fidelity large area nanopatterning of silicon with femtosecond light sheet. *Applied Physics A*, 124(1):1–5, 2018.

[53] ZEISS Sigma. Zeiss axio scope a1, https://www.microscopemaster.com/zeiss-axio-scope-a1.html.

[54] S Singh, M Argument, YY Tsui, and R Fedosejevs. Effect of ambient air pressure on debris redeposition during laser ablation of glass. *Journal of applied physics*, 98(11):113520, 2005.

[55] Mihai Stafe, Aurelian Marcu, and Niculae N Puscas. *Pulsed laser ablation of solids: basics, theory and applications*, volume 53. Springer Science & Business Media, 2013.

[56] E Vo Stupochenko, So A Losev, and AI Osipov. Relaxation processes in shock waves. Technical report, FOREIGN TECHNOLOGY DIV WRIGHT-PATTERSON AFB OHIO, 1968.

[57] Abderazek Talbi, Sostaine Kaya-Boussougou, Audrey Sauldubois, Arnaud Stolz, Chantal Boulmer-Leborgne, and Nadjib Semmar. Laser-induced periodic surface structures formation on mesoporous silicon from nanoparticles produced by picosecond and femtosecond laser shots. *Applied Physics A*, 123(7):1–7, 2017.

[58] Abderazek Talbi, Agnès Petit, Amer Melhem, Arnaud Stolz, Chantal Boulmer-Leborgne, G Gautier, T Defforge, and N Semmar. Nanoparticles based laser-induced surface structures formation on mesoporous silicon by picosecond laser beam interaction. *Applied Surface Science*, 374:31–35, 2016.

[59] Shuntaro Tani and Yohei Kobayashi. Pulse-by-pulse depth profile measurement of femtosecond laser ablation on copper. *Applied Physics A*, 124(3):1–5, 2018.

[60] George D Tsibidis, Marios Barberoglou, Panagiotis A Loukakos, Emmanuel Stratakis, and Costas Fotakis. Dynamics of ripple formation on silicon surfaces by ultrashort laser pulses in subablation conditions. *Physical Review B*, 86(11):115316, 2012.

[61] George D Tsibidis, Alexandros Mimidis, Evangelos Skoulas, Sabrina V Kirner, Jörg Krüger, Jörn Bonse, and Emmanuel Stratakis. Modelling periodic structure formation on 100cr6 steel after irradiation with femtosecond-pulsed laser beams. *Applied Physics A*, 124(1):1–13, 2018.

[62] George D Tsibidis, Evangelos Skoulas, Antonis Papadopoulos, and Emmanuel Stratakis. Convection roll-driven generation of supra-wavelength periodic surface structures on dielectrics upon irradiation with femtosecond pulsed lasers. *Physical Review B*, 94(8):081305, 2016.

[63] Masahiro Tsukamoto, Keita Asuka, Hitoshi Nakano, Masaki Hashida, Masahito Katto, Nobuyuki Abe, and Masayuki Fujita. Periodic microstructures produced by femtosecond laser irradiation on titanium plate. *Vacuum*, 80(11-12):1346–1350, 2006.

[64] R Valizadeh, OB Malyshev, T Sian, JS Colligon, Q Li, and W Perrie. Laser ablated surface engineering: from discovery to machine application. In *CERN Yellow Reports: Conference Proceedings*, volume 7, pages 209–209, 2020.

[65] Reza Valizadeh, Oleg B Malyshev, Sihui Wang, Svetlana A Zolotovskaya, W Allan Gillespie, and Amin Abdolvand. Low secondary electron yield engineered surface for electron cloud mitigation. *Applied Physics Letters*, 105(23):231605, 2014.

[66] A Ya Vorobyev and Chunlei Guo. Femtosecond laser nanostructuring of metals. *Optics express*, 14(6):2164–2169, 2006.

[67] Anatoliy Y Vorobyev and Chunlei Guo. Direct femtosecond laser surface nano/microstructuring and its applications. *Laser & Photonics Reviews*, 7(3):385–407, 2013.

[68] IN Zavestovskaya, AP Kanavin, and NA Men'kova. Crystallization of metals under conditions of superfast cooling when materials are processed with ultrashort laser pulses. *Journal of Optical Technology*, 75(6):353–358, 2008.

[69] Dmitry A Zayarny, Andrey A Ionin, Sergey I Kudryashov, Sergey V Makarov, Alexander A Kuchmizhak, Oleg B Vitrik, and Yury N Kulchin. Pulse-width-dependent surface ablation of copper and silver by ultrashort laser pulses. *Laser Physics Letters*, 13(7):076101, 2016.

[70] Craig A Zuhlke, Dennis R Alexander, John C Bruce, Natale J Ianno, Chad A Kamler, and Weiqing Yang. Self assembled nanoparticle aggregates from line focused femtosecond laser ablation. *Optics Express*, 18(5):4329–4339, 2010.